

MSc Thesis

Natural frequency analysis of the pushpart of a metal pushbelt continuous variable transmission

J.A. van den Meiracker



This is a public version in which all confidential information has been removed.

Natural frequency analysis of the pushpart of a metal pushbelt continuous variable transmission

by

Jacob Antonius van den Meiracker

to obtain the degree of Master of Science

at the Delft University of Technology,
to be defended publicly on Thursday October 18, 2018 at 09:00 AM.

Student number:	4149718
Project duration:	January 2, 2018 – October 18, 2018
Supervisors:	Dr. ir. D. de Klerk TU Delft Ing. P. Ribbers Bosch Transmission Technology
Exam committee:	Dr. ir. R. Happee TU Delft (Chairman) Dr. F. Alijani TU Delft Dr. ir. D. de Klerk TU Delft Ing. P. Ribbers Bosch Transmission Technology

This thesis is confidential and cannot be made public.



This is a public version in which all confidential information has been removed.

Preface

In the autumn of 2015 I made the important but most of all exciting decision to register for the Master Vehicle Engineering at the Delft University of Technology. Being a major car enthusiast this actually never was a true decision but more a confirmation of my passion. I remember the feeling of recognition during the introduction week of the master when it turned out I was not the only guy that always uses his car, for absolutely everything.

Now, almost three years later, I am proud to present to you my master thesis. But first I would like to say thanks to the people who supported and guided me the past few years and especially during my graduation project.

First and foremost my parents, Afke and Eric van den Meiracker, for their unconditional and continuous support during all my years in Waddinxveen and Delft, for giving me the opportunity to already start a career during my bachelor and master, for always believing in me. Second my girlfriend Britt de Wilde, for her unconditional support, for always trusting in me. Thirdly my sisters, Inge and Anna van den Meiracker, for their occasional contribution to a ‘dynamic’ atmosphere while learning for exams. My best friends Christian de Rooij, Ewoud Spruijt, Gijs Haeren and Marten de Vries with whom I can always find the time to blow off some steam, or just have a good discussion about nothing. My friends from the master, Alexander van Doeveren, Joël Dijkhuizen, Ries Uittenbogaard, Robert Cornet and Quinn Vroom. Vehicle Dynamics, Nonlinear Mechanics and the Integration Project where never boring with you guys.

Next to my family and friends I would like to thank my Bosch supervisor Peter Ribbers for giving me the opportunity to do an internship and graduation project at Bosch and supporting me during this period. My colleagues at Bosch, Arie van der Velde, LiChao Pan, Pepijn Smits and Roderick Bijkerk who also supported me with a critical eye to keep me sharp while making my decisions and my TU Delft supervisor Dr. ir. Dennis de Klerk for his support and for letting me appreciate my performance when I perhaps was to critical of myself.

I want to dedicate this thesis to my grandfather Ing. Jaap Landkroon,
of whom I am sure would have wanted the opportunity to read it.

I hope you enjoy your reading.

*Joep van den Meiracker
Leiderdorp, September 2018*

Summary

Over the years car manufactures have increased their efforts in reducing passenger cabin noise. Furthermore driver sensitivity to acoustical comfort has increased because vehicles have continuously become quieter [10]. The consequence of these developments is that noise from the driveline is now a significantly contributing factor to the comfort level of the driver. For vehicles equipped with continuous variable transmissions (CVT) higher standards regarding noise and vibration reduction are demanded. Research by both Bosch Transmission Technology (Bosch) [16] and one of its customers [21] has shown that there is a relation between noise and vibrations originating from the differential of the driveline and belt vibrations inside the CVT. Although the cause of these vibrations is known, sufficient knowledge is not available to improve the design of the CVT in such way that these driveline vibrations are prevented or reduced. The main reason for this is the application of a metal pushbelt in the CVT's designed by Bosch.

A pushbelt CVT transfers the motor torque to the wheels via a metal pushbelt that is loaded with both a tensile and compressive force respectively called pull- and pushforce. The pushbelt is an assembly of two bundles of strings or loopsets, and elements, firmly packed together in between the loopsets, also known as element string. Pullforce is applied in the loopsets and pushforce in the element string, in between elements. The interactions occurring between the loopsets and elements as a result of these two forces and other belt specific nonlinear effects make the dynamics behind this type of belt much more complicated than regular belt drives. The natural frequency of the pushbelt is found by observing the transversal vibration of the pushpart of the pushbelt. The pushpart of the belt is the part between the in- and output axles that transfers the motor torque. A belt parameter that is frequently linked to having an effect on the flexural rigidity of the pushpart and thereby on its natural frequency is Δt . Δt indicates the thickness difference between bottom and top of each element. Having a positive Δt results in elements being thicker at the top than at the bottom. Similarly to an arch bridge the pushpart also arcs upward as a result of the local thickness difference of the elements. The pushforce in between elements is distributed over the top and bottom part of the elements. The distribution ratio depends on the position of the bending line over which the pushpart bends.

For ordinary belt drives extensive literature is available, describing the natural frequency of belts under axial tension. Due to the fact that a pushbelt CVT is highly specialized and its dynamics are complex, the frequency response of the pushbelt and its underlying effects have not been truly investigated at Bosch prior to this thesis. Furthermore literature about this subject is barely available. The main objective of this research is therefore to gain insights in the natural frequency of the pushbelt of the CVT.

To find the natural frequency of the pushbelt a tool used at Bosch for doing measurements on the pushpart was modified to perform natural frequency measurements on this part of the belt. Measurements were done on four belts with Δt and over five different loadpaths per belt. A loadpath describes the relation between pull- and pushforce since both forces are coupled, where the pullforce always is higher than the pushforce. From the frequency measurement results a lot of conclusions were drawn. Regarding a single belt it was concluded that the loadpaths over which is measured are nonlinear. The frequency change for increasing load can be divided in two parts. At low pushforce the frequency increases fast and for high pushforces the frequency increases slowly and eventually stagnates. The area in between these two parts is named the transition area. In this area the frequency makes a jump in trend. The lower trend fades out and the higher trend fades in. Furthermore at a loadpath with high initial pullforce the frequency is higher than for a loadpath with low initial pullforce, matching the theory that

increasing tension in similar systems increases the frequency. However the fact that increasing pushforce also increases the frequency contradicts this theory.

Comparing all four belts in first it was concluded that the loadpaths between belts do not match although starting at similar initial pullforces. By interpolating the frequency data the measurements for all four belts could be compared, showing that the vibration frequency overall is higher for higher [REDACTED] belts. Next to that the increase in frequency at low pushforces is more violent for increasing [REDACTED]. From trends in corresponding color maps it was seen that at low pushforces the changing in frequency is mostly depending on the pushforce and for high pushforces the frequency seems dependent on a relation similar to that between pull- and pushforce.

By analyzing the transition area it was shown that the frequency jump is mostly constant for the belts with [REDACTED] and shows an increase over the loadpaths for an [REDACTED]. Moreover regarding the forces and force range where the transition takes place it can be seen that for increasing [REDACTED] the transition takes place at lower pushforces and at smaller pushforce ranges. For increasing initial pullforce of the loadpath this difference becomes smaller.

Besides frequency measurements the pushpart has also been subjected to a modal analysis. This modal analysis was performed on a belt with [REDACTED] by use of the roving hammer approach. A mode shape was retrieved at four loadcases; below transition, at transition in both lower and higher frequency trend and above transition. The results from this analysis showed that for all measured frequencies, below, in and above the transition area, a first mode or fundamental frequency was found.

Comparing the individual mode shapes of each of the belts to each other by doing a MAC analysis it was concluded that overall the mode shapes indeed are very much alike. However comparing the MAC values relatively to each other it was concluded that for both belts the mode shape of the higher frequency in the transition area, located in the fading in frequency trend, is slightly different from the mode shapes corresponding to the other three measured frequencies. Not only the mode shapes of the frequencies in the lower fading out frequency trend, but also the mode shape corresponding to the highest measured frequency in the higher fading in trend. An explanation for this difference in mode shape cannot be given although it does not seem coincidental that for both belts a similar conclusion was drawn.

Finally an attempt was made to put together a model that can calculate the natural frequency of the pushpart. This was done by comparing outcomes of frequency measurements with a model based on the beam theory behind ordinary belt drives. Based on the suspicion that the flexural rigidity of the pushpart is influenced by its compression stiffness a direct relation between the two was found in which the flexural rigidity of the pushpart assembly is formulated as a combination of the flexural rigidity of the loopsets and element string. The pushpart model requires the initial length and compression stiffness of the pushpart to be known. As well as the location and size of the element-element contact area and corresponding pushpart bending line. The last two are however not known. Because of that several model cases were composed, each giving a plausible configuration of contact area size, location and bending line location in the pushpart. By applying two different model cases over the total pushforce range of the frequency response an accuracy of the model between -24% and 10% compared to the frequency measurements was achieved. Next to that, by defining the model cases for the pushpart model an explanation could be given for the jump in frequency in the transition area. The bending line over which the pushpart bends shifts, most likely in combination with a change in pushforce distribution in the element-element contact area. In the transition area, for increasing pushforce, the bending line shifts downwards.

This research showed the frequency response of the pushpart of a metal pushbelt CVT and corresponding pushpart mode shapes. With these new insights a model has been put together showing that in general the dynamics behind a pushbelt and ordinary belt are not that different. However effects like [REDACTED] and the interaction between the individual belt parts changing the pushforce distribution and pushpart bending line have a serious impact on the flexural rigidity of the pushbelt.

List of Figures

2.1	Variator: variable transmission ratio	4
2.2	Pulley cross section	5
2.3	Elements and Loopsets	5
2.4	Element interactions	6
2.5	Variator side view	7
2.6	Minimal Bending Radius	7
2.7	Loadpath examples	8
2.8	Catsback shape in pushpart	8
2.9	Marked element-element contact area	9
2.10	Neutral bending line shift for changing dominant element-element contact	9
3.1	Belt vibration	11
4.1	String in free bending vibration	12
4.2	Beam in free bending vibration	13
4.3	Tensioned beam in free bending vibration	15
4.4	Axially moving tensioned beam in forced bending vibration	17
7.1	Pushpart schematic	26
8.1	Pushpart assembly	27
8.2	Pushpart assembly in compression tool	28
8.3	Compression tool	28
8.4	End-element side view	29
8.5	End-element 3D view	29
8.6	Misalignment forces in pushpart and measured forces	29
8.7	Measurement setup	31
8.8	Four layer loopset test measurement	33
8.9	Four layer loopset test error	33
9.1	Measured loadpaths belt B	35
9.2	Belt B: FRF at single loadcase	35
9.3	Belt B: FRF contour at single loadcase	35
9.4	Belt B: FRF at single loadcase	36
9.5	Belt B: peak frequencies loadpath	36
9.6	Belt B: peak frequencies for all loadpaths vs. pushforce	37
9.7	Belt B: peak frequencies for all loadpaths vs. pullforce	37
9.8	Measured loadpaths all belts	38
9.9	Belt A: frequency contour plot	38
9.10	Belt B: frequency contour plot	38
9.11	Belt C: frequency contour plot	39
9.12	Belt D: frequency contour plot	39
9.13	Transition area: frequency jump	39

9.14	Transition area: force differences	39
10.1	Impact hammer hit locations indicated on the pushpart	41
10.2	Overview of origin of the mode shapes	42
10.3	Undeformed catsback shapes belt B	43
10.4	Undeformed catsback shapes belt D	43
10.5	Belt B mode shapes	43
10.6	Belt D mode shapes	44
10.7	Belt B MAC matrix	44
10.8	Belt D MAC matrix	44
10.9	Belt B MAC matrix values	45
10.10	Belt D MAC matrix values	45
11.1	Measured and calculated natural frequencies at the start of the loadpaths	47
11.2	Belt D: measured natural frequency vs. loopsets model against pullforce	48
11.3	Belt D: measured natural frequency vs. loopsets model against pushforce	48
11.4	Percentual difference between measurements and loopsets model	49
11.5	Compression measurement error	50
11.6	Belt D: compression curves	50
11.7	Belt D: stiffness curves	50
11.8	All belts: compression stiffness curves scattered	
11.9	Percentual difference between measurements and pushpart model without element string flexural rigidity	51
11.10	Case 1	53
11.11	Case 2	53
11.12	Case 3	53
11.13	Case 4	53
11.14	Case 5	53
11.15	Case 6	53
11.16	Case 7	53
11.17	Percentual difference between measurements and pushpart model for belt D for all model cases	55
11.18	Percentual difference between measurements and pushpart model for all belts, model case 6 and loadcases above transition	55
11.19	Percentual difference between measurements and pushpart model for all belts, model case 6 for loadcases below transition	56
11.20	Percentual difference between measurements and pushpart model for all belts, model case 4 below transition and model case 6 above transition	56
11.21	Percentual difference between measurements and pushpart model for all belts, model case 5 below transition and model case 6 above transition	56
11.22	Percentual difference between measurements and pushpart model for all belts, model case 6 below transition and model case 6 above transition	57
11.23	Percentual difference between measurements and pushpart model for all belts, model case 7 below transition and model case 6 above transition	57
12.1	Research overview	61
A.1	Pushpart assembly in the tool	66
A.2	Fixation of the support block	67
A.3	Pushpart assembly	67
A.4	CVT belt with elements removed for pushpart assembly	67
A.5	Loopset validation measurement: tool setup	68
A.6	Loopset validation measurement: measurement setup	68
B.1	Belt A: measured loadpaths	69

B.2	Belt B: measured loadpaths	69
B.3	Belt C: measured loadpaths	70
B.4	Belt D: measured loadpaths	70
B.5	Belt A: resonance frequencies for all loadpaths vs. pushforce	70
B.6	Belt A: resonance frequencies for all loadpaths vs. pullforce	70
B.7	Belt B: resonance frequencies for all loadpaths vs. pushforce	71
B.8	Belt B: resonance frequencies for all loadpaths vs. pullforce	71
B.9	Belt C: resonance frequencies for all loadpaths vs. pushforce	71
B.10	Belt C: resonance frequencies for all loadpaths vs. pullforce	71
B.11	Belt D: resonance frequencies for all loadpaths vs. pushforce	72
B.12	Belt D: resonance frequencies for all loadpaths vs. pullforce	72
C.1	Belt A: compression curves	73
C.2	Belt B: compression curves	73
C.3	Belt C: compression curves	74
C.4	Belt D: compression curves	74
C.5	Belt A: stiffness curves	74
C.6	Belt B: stiffness curves	74
C.7	Belt C: stiffness curves	75
C.8	Belt D: stiffness curves	75
C.9	Percentual difference between pushpart model and measurements for belt A for all cases	75
C.10	Percentual difference between pushpart model and measurements for belt B for all cases	75
C.11	Percentual difference between pushpart model and measurements for belt C for all cases	76
C.12	Percentual difference between pushpart model and measurements for belt D for all cases	76
D.1	Research overview	78

List of Tables

8.1	Belts selected for frequency measurements	30
8.2	Sensorlist frequency measurements	31
8.3	DAQ hard- and software list	31
10.1	Loadcases of modal analysis	42

Contents

Preface	III
Abstract	V
List of Figures	X
List of Tables	XI
1 Introduction	1
1.1 Problem statement	1
1.2 Investigation topic	1
1.3 Report structure	2
I Literature Study	3
2 Pushbelt CVT	4
2.1 Introduction	4
2.2 Variator	4
2.3 Pushbelt	5
2.3.1 Elements and loopsets	5
2.3.2 Torque transfer	6
2.3.3 Bending freedom	6
2.4 Pushpart	6
2.4.1 Loadpath	7
2.4.2 Catsback	8
2.4.3 Pushforce distribution	9
3 Pushbelt vibration	10
3.1 Introduction	10
3.2 Vibration cause	10
3.3 Vibration definition	10
4 Ordinary belt vibration	12
4.1 Introduction	12
4.2 Free vibration	12
4.2.1 String vibration	12
4.2.2 Beam vibration	13
4.2.3 Tensioned beam vibration	14
4.3 Belt speed	15
4.3.1 Method of multiple scales	16
4.3.2 Approximate analysis	16
4.4 Extended beam models	18
4.4.1 Rayleigh beam model	18

4.4.2	Timoshenko beam model	19
5	Bosch models	21
5.1	Introduction	21
5.2	██████████	21
5.3	██████████	21
5.4	██████████████████	21
5.5	██████████████████	22
5.6	██████████	22
6	Conclusion: literature study	23
II	Master Thesis	24
7	Research scope	25
7.1	Introduction	25
7.2	Parameter selection	25
7.3	Boundary conditions	25
7.4	System schematic	26
7.5	Assumptions	26
8	Measurement setup	27
8.1	Introduction	27
8.2	Compression tool	27
8.3	Tool modifications	28
8.4	Assumptions	30
8.5	Scope	30
8.6	Sensors and data acquisition	31
8.7	Procedure	31
8.7.1	Tool setup	31
8.7.2	Measurement setup	32
8.8	Tool validation: loopset measurement	32
9	Frequency measurement results	34
9.1	Introduction	34
9.2	Single belt	34
9.2.1	Loadpaths	34
9.2.2	Frequencies	34
9.3	Belt comparison	37
9.3.1	Loadpaths	37
9.3.2	Frequencies	37
9.3.3	Transition area	39
9.4	Conclusion	40
10	Pushpart modal analysis	41
10.1	Introduction	41
10.2	Setup	41
10.3	Results	42
10.4	Conclusion	45

11 Pushpart modeling	46
11.1 Introduction	46
11.2 Loopsets model	46
11.2.1 Loadpath start	46
11.2.2 Loadpath start to end	47
11.3 Compression stiffness	49
11.3.1 Catsback compensation	49
11.3.2 Compression curves	50
11.3.3 Stiffness curves	51
11.3.4 Compression curve fitting	51
11.4 Element string implementation	52
11.4.1 Pushpart as beam	52
11.4.2 Flexural rigidity	52
11.5 Model case selection	54
11.5.1 Above transition area	55
11.5.2 Below transition area	55
11.6 Conclusion	57
12 Conclusion	59
12.1 Frequency measurements	59
12.2 Pushpart modal analysis	60
12.3 Pushpart model	60
12.4 Research overview	61
12.5 Research topics	62
13 Discussion	63
13.1 Research scope and measurement setup	63
13.2 Frequency measurements	63
13.3 Modal Analysis	64
13.4 Pushpart Model	64
14 Recommendation	65
Appendix A Frequency measurement tool	66
A.1 Modified Tool and components	66
A.2 Tool validation	68
Appendix B Frequency measurements	69
B.1 Loadpaths	69
B.2 Resonance frequencies	70
Appendix C Pushpart modeling	73
C.1 Compression curves	73
C.2 Stiffness curves	74
C.3 Case selection	75
Appendix D Research overview	77
Bibliography	80

Chapter 1

Introduction

In 1932 Hub van Doorne founded DAF, a Dutch manufacturing company which initially made trucks and truck trailers. In 1958 DAF introduced the DAF 600 a relatively cheap and lightweight passenger car which was affordable to the common people. Special about this vehicle was its automatic transmission, called the Variomatic. A continuous variable transmission (CVT) that transferred the engine power to the wheels via two rubber belts. To improve the lifespan and reduce the size of the transmission, the rubber belts were eventually replaced by a metal pushbelt. This new design also had the benefit that the transmission could cope with higher torques.

The metal pushbelt CVT initially was produced by Van Doorne's Transmissie (VDT) which became part of the German Bosch concern in 1995. In 2009 Bosch changed the name of the company to Bosch Transmission Technology (Bosch) and currently is market leader regarding the development and mass production of metal pushbelts for CVT's [2].

1.1 Problem statement

Next to reliability, safety and efficiency a major selling point for passenger cars is driving comfort. Over the years car manufactures have increased their efforts in reducing passenger cabin noise. Road surface and wind noise have been reduced with the result that other background noises are less masked. Furthermore driver sensitivity to acoustical comfort has increased because vehicles have continuously become quieter [10]. The consequence of these developments is that noise from the driveline is now a significantly contributing factor to the comfort level of the driver. Regarding the CVT design higher standards regarding noise and vibration reduction are demanded by customers.

Research by both Bosch [16] and one of its customers [21] has shown that there is a relation between noise and vibrations originating from the differential of the driveline and belt vibrations inside the CVT. Due to the reduction of other vehicle noise and vibration levels this noise is becoming a more and more serious problem.

1.2 Investigation topic

The noise from the driveline arises at specific operating conditions of the vehicle. The belt of the CVT is triggered and starts vibrating around a certain frequency. Bosch is able to identify and track this frequency for changing operating conditions. However it is unclear if and how this frequency is related to the natural frequency of the CVT belt. At Bosch research on this topic has started recently and several pushbelt CVT models describing the complete driveline, the transmission or parts of it are used to investigate occurring vibrations. The ultimate goal of this research is to formulate a mathematical model or relation for finding the natural frequency of the pushbelt CVT. If this goal is achieved the pushbelt CVT could in theory be designed in such way that the occurring noise is reduced. Understanding the working mechanism behind the belt vibrations is key for tuning the belt design so driveline vibrations

are reduced. In this master thesis the available research is extended where possible in contribution to achieving this ultimate goal.

The main objective is to gain more insides in the natural frequency of the CVT pushbelt.

Before this research can be done it is important to get familiar with the pushbelt CVT system designed by Bosch. Prior to the research a literature study is performed. An extensive explanation of the working principle of the CVT pushbelt will be given. Available research on the natural frequency analysis of ordinary belt drives will be used to find out what general belt parameters influence its natural frequency. This can later be used as template or as comparison for finding the natural frequency of pushbelt CVT drives. Finally the models used by Bosch are summarized and their ability to analyze belt vibrations and corresponding vibration frequencies is given.

Knowing the current state of art regarding the knowledge on pushbelt CVT belt vibrations the research will be extended. In this master thesis it is investigated what belt parameters or external factors have an influence on the natural frequency of the belt. An attempt is made to measure the vibration frequencies and to visualize the vibrations of the belt. These insides could help in formulating a mathematical model for calculating the natural frequency of the belt or at least help in validating the models available at Bosch and possibly help in extending and improving them in describing the belt mechanics.

1.3 Report structure

The structure of this master thesis is derived from the objectives of this investigation. Chapters 2 to 6 include the literature study performed in preparation to this master thesis. In Chapter 2 an extensive explanation is given on the general working mechanisms behind the pushbelt CVT. A closer look on belt vibrations is made in Chapter 3. What exactly is meant by belt vibration is explained and assumptions made for this definition are listed. Subsequently the general dynamics of ordinary belt drives are described in Chapter 4 together with analytic methods to find their natural vibration frequencies. In Chapter 5 the models available at Bosch are summarized. Finally in Chapter 6 conclusions are drawn from the gained knowledge.

Chapters 7 to 14 include the new research performed in this master thesis. In first the scope of this research is given in Chapter 7. In Chapter 8 the entire process of performing frequency measurements on the pushbelt is summed up. Subsequently the measurement results are presented in Chapter 9. Chapter 10 presents the results of a modal analysis performed on the pushbelt. In Chapter 11 an attempt is made to formulate a model that can replicate the frequency measurements. Finally in Chapters 12 to 14 all conclusions that can be drawn from the research are summarized and listed. The master thesis and choices made during the investigation are discussed and recommendations for future research are given.

Part I

Literature Study

Chapter 2

Pushbelt CVT

2.1 Introduction

A pushbelt CVT is a highly complex piece of engineering. Understanding the working mechanism of this type of transmission is crucial for the investigation that is being described in this report. Although more recent research by amongst others Schindler, Ulbrich, Pfeiffer, Van der Velde and Brandsma [24, 25, 38] is providing an increasingly better understanding of the pushbelt CVT a large contribution has been made by the research by [redacted] [36]. However, due to a higher simplicity, earlier research about regular CVT systems is much more available, for example by Cuypers [6, 7]. In this chapter a general description of the working principal of a pushbelt CVT is given. If relevant for this investigation a more thorough explanation of specific components or phenomenas is provided.

2.2 Variator

A CVT is an automatic transmission which takes part in the driveline of a passenger vehicle like a regular transmission. Its main components are two pulleys and a belt, together called the variator. The drive and driven pulley are called primary and secondary pulley respectively. Each pulley consists of two conical disks or sheaves; one fixed to either the input or output shaft, the fixed sheave, and the other connected to a hydraulic actuator, the loose sheave. The actuators allow the loose sheaves to slide in axial direction, changing the width of each pulley.

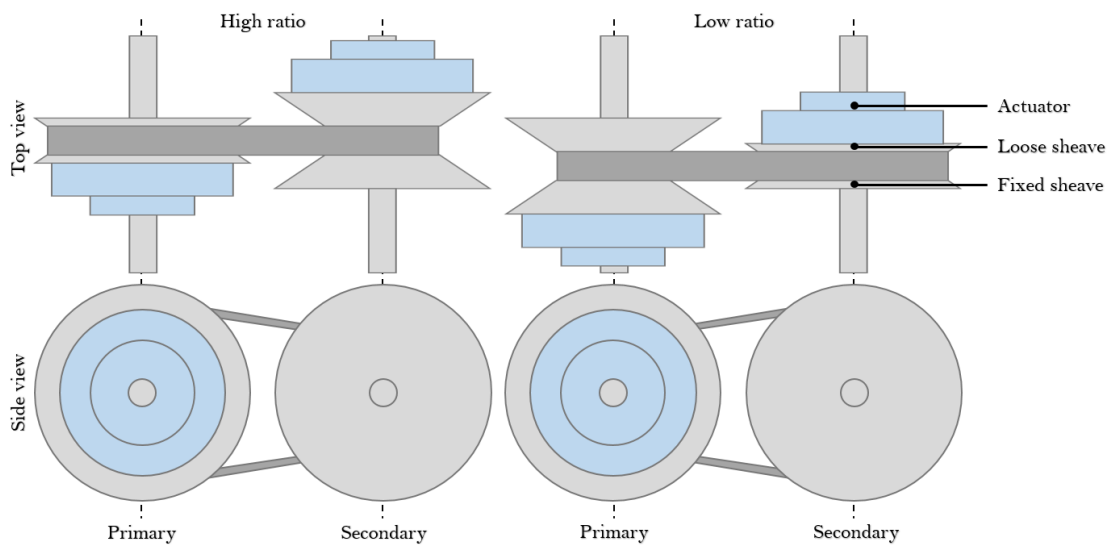


Figure 2.1: Variator: variable transmission ratio

As illustrated in Figure 2.1 with changing pulley widths, the transmission ratio of the CVT can be altered. The pulley widths and thereby the transmission ratio are controlled by a control unit which monitors the vehicle state parameters to calculate the optimal transmission ratio. Since the pulley width can be controlled steplessly the transmission ratio can be altered steplessly giving it an advantage over a regular automatic transmission which has fixed gear ratios.

The motor- or primary torque is transferred to the belt by a friction force between the belt flanks and pulley sheaves. In Figure 2.2 a cross section of one of the pulleys is given. The pushbelt's flank angles generally match the sheave angles of the pulleys to maximize the contact area between them. These contact areas are highlighted in red. The belt-pulley friction is generated by a clamping force in the pulley originating from the hydraulic actuator pressure. The torque-transfer from belt to secondary pulley is based on the same principle.

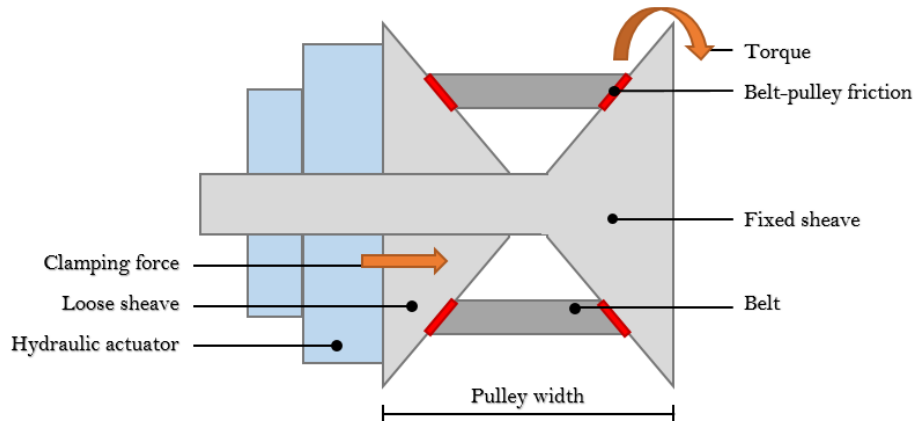


Figure 2.2: Pulley cross section

2.3 Pushbelt

Conventional CVT systems make use of an ordinary belt or chain drive. The design of a pushbelt CVT is based on a different approach consisting of a metal pushbelt. The main difference between these two concepts is the load in the belt while transferring the torque from the engine to the wheels. In a conventional CVT the belt is loaded by tension solely and in the pushbelt CVT the belt is loaded by both a tensile and compressive force which are called pullforce and pushforce respectively.

2.3.1 Elements and loopsets

The metal pushbelt is an assembly of two components, the loopsets and the elements. The loopsets are bundles of thin metal rings or loops span between the pulleys. The elements are thin metal parts with a unique shape. This shape enables the loopset to retain the elements and pack them close together to form an element string as in Figure 2.3. Each element consist of a so-called head and body, connected by the neck or pillar of the element. These are respectively the element sections above and beneath the loopsets.

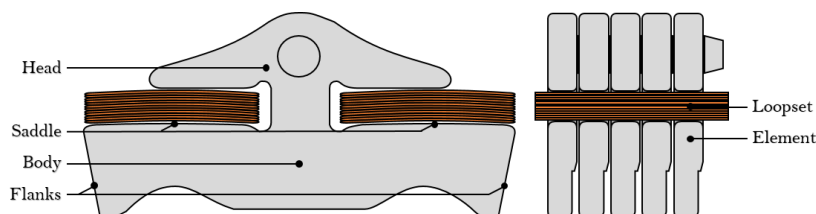


Figure 2.3: Elements and Loopsets

2.3.2 Torque transfer

The working principle of the pushbelt CVT is based on three interactions between pulleys, loopsets and elements, the element-pulley, element-loop and element-element contact respectively. The element-pulley contact is the contact of the pulley sheaves with the element flanks, similarly to a regular belt being wedged between the pulley sheaves. Note that this is the contact highlighted in red in Figure 2.2. The element-loop contact is the contact of each loopset with each saddle of the elements as indicated in Figure 2.3. The element-element contact is the mutual contact between elements and is split in a contact area at the body and a contact area in the head of the element. Because of these three distinct interactions in the variator assembly, three forces are applied to the elements during operation. Firstly a compressive force in axial direction as a result of the clamping force in the pulley. Secondly a transversal force on the saddles of the elements as a result of the interaction with the loopsets and the applied pullforce. And thirdly a pushforce in longitudinal direction as a result of the element-element interaction. All three applied forces are visualized in Figure 2.4 by respectively green, red and blue arrows. Note that the indicated directions and corresponding nomenclature is used throughout the entire report to point out the directions compared to the belt or element orientation.

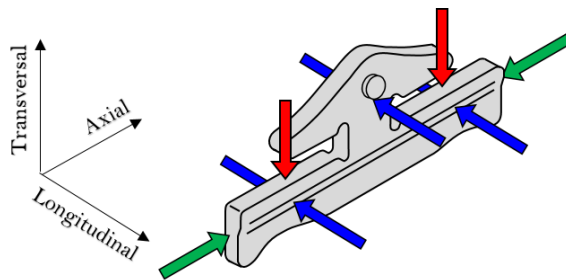


Figure 2.4: Element interactions

Knowing that there must be a force balance in the variator, it can be concluded that the pullforce in the loopsets is generated by the clamping forces in the pulleys. Increasing the clamping forces reduces the pulley widths and enlarges the running radii of the belt in the pulleys thereby tensioning the loopsets. During operation, on the primary side, the elements are 'caught' and clamped in the pulley and gradually loaded with a pushforce along the primary wrapped angle [8]. At the moment the element string leaves the primary pulley the elements are closely packed together and loaded with a pushforce. This part of the belt between primary and secondary pulley, loaded with a pushforce, is called the pushpart, Figure 2.5. On the secondary side the elements are 'caught' and clamped in the secondary pulley and gradually unloaded from pushforce, until no pushforce between the elements exists when leaving the secondary pulley. The angle over which this takes place is the secondary wrapped angle [8]. From this process it can be concluded that the pushforce is directly related to the torque transferred from the primary to secondary pulley. From the secondary back to the primary side the elements are not loaded with a pushforce. This part of the belt is called the slack- or loosepart.

2.3.3 Bending freedom

In order for the belt to wrap around the pulleys the belt needs a minimal bending freedom. This bending freedom is a result of the shape of the elements. Each element rocks over its neighboring element at the rocking edge [28], which is the lower element-element contact area as described in Section 2.3.2. The bodies of the elements are tapered at the bottom to form a clearance [34]. The smallest bending radius of the belt is defined by the clearance and rocking edge radius of the elements as illustrated in Figure 2.6.

2.4 Pushpart

The pushpart of the pushbelt is the part that transfers the torque from the primary and secondary pulley. The pushforce between the elements is therefore highest in this part. So far the pushbelt CVT is

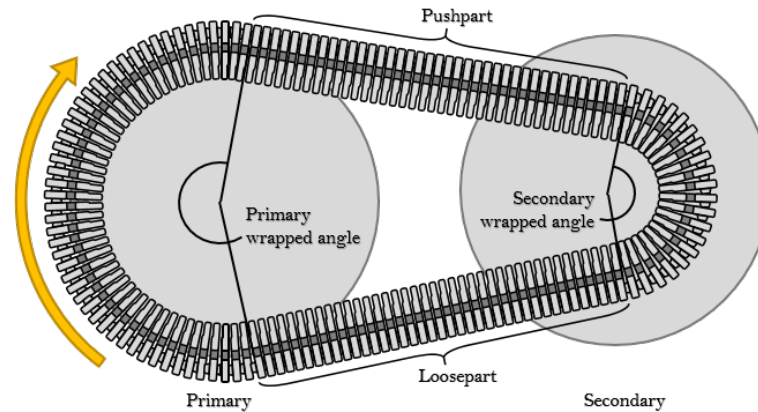


Figure 2.5: Variator side view

described generally. The way the pushforce is distributed between the elements is more complex than it seems. Understanding the combination of pull- and pushforce and their effect on the interaction between elements and on the shape and properties of the pushpart requires a more detailed explanation.

2.4.1 Loadpath

The amount of pull- and pushforce on respectively the element string and loopsets is related to the amount of torque that is transferred through the CVT. The ratio between pull- and pushforce depends on multiple mechanisms inside the belt, for example the amount of clamping force in the pulleys, the friction between pulley, elements and loopsets but also the effect of catsback, which will be explained in the next section.

For increasing pushforce the pullforce also increases mainly due the increased torque transferred by the CVT. The pushforce increases when a higher torque is transferred through the CVT. This higher torque can only be transferred when the clamping force of the pulleys is increased, otherwise the belt would slip inside the pulley. Increased clamping force results in a higher pullforce in the loopsets as explained in Section 2.3.2. The relation between pull- and pushforce is nonlinear because of e.g. nonlinear compression of the elements in the pushpart. Two examples of such force relation can be seen in Figure 2.7, where the pullforce is plotted against the pushforce. The path that is created for increasing pushforce will for convenience be called the loadpath. Each dot of each loadpath indicates a unique combination of pull- and pushforce which will be called a loadcase.

The initial pullforce, when no pushforce is applied, indicates the starting point of a loadpath. The black line in bold indicates where pullforce equals pushforce. Normally it is not possible to put the pushpart in a loadcase that approaches this boundary because the pushpart will buckle and collapse when this boundary is crossed. For each loadpath the relation between pull- and pushforce is different.

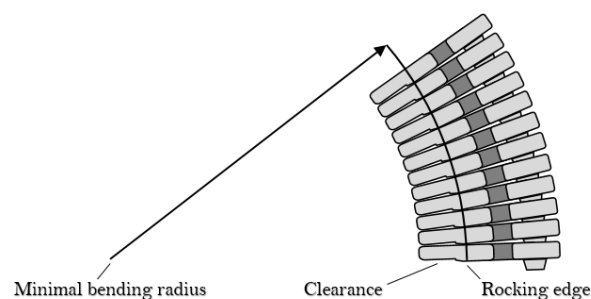


Figure 2.6: Minimal Bending Radius

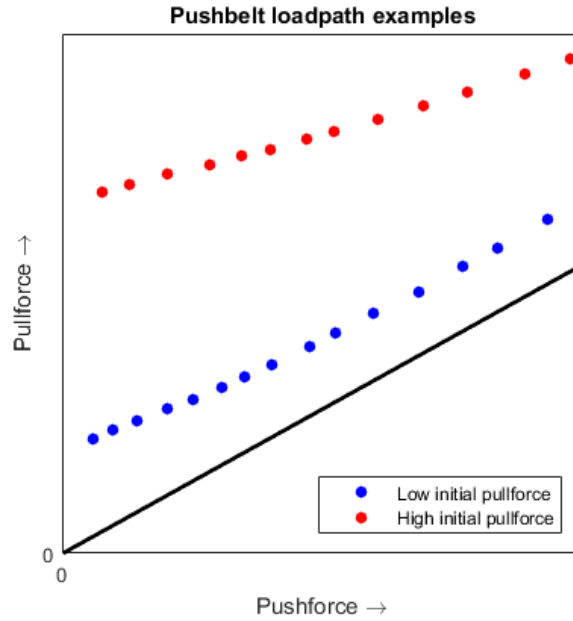


Figure 2.7: Loadpath examples

2.4.2 Catsback

In Figure 2.5 the pushpart is displayed as a straight part. In normal belt operation however the pushpart is not straight, but has a small curve. Since the shape of the pushpart resembles the shape of the back of a cat, it is called the catsback [31]. The higher the curve, the higher the catsback. This particular shape of the pushpart finds its origin in two different properties of the elements.

The first property that influences catsback is Δt [8, 15]. The geometric element parameter Δt is defined as the thickness of the head minus the thickness of the body. A positive value means a relatively thicker head compared to the body. Stacking the elements together in an element string result in an arc similarly to that of a stone arch bridge where the building blocks are also thicker at the top. The second property that influences catsback is the compression stiffness of the elements. The element compression stiffness at the rocking edge is lower than at the head resulting in the elements being compressed more at the rocking edge than at the head under pushforce. As a result the element thickness at the head is larger than at the body. The compression of the element basically enlarges Δt .

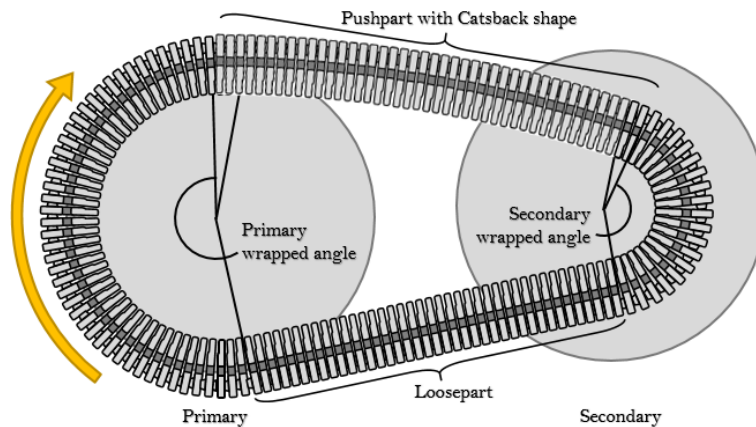


Figure 2.8: Catsback shape in pushpart

The locations at which the pushpart starts and ends, respectively the locations the pushbelt leaves the primary pulley and enters the secondary pulley are not fixed. For increasing catsback height the length of the pushpart increases. This can be seen in Figure 2.8. Because the belt length is fixed the increase in pushpart length is compensated by a decrease in wrapped angles.

2.4.3 Pushforce distribution

In Section 2.3.2 it was stated that the element-element contact is made up of two contact areas between the elements. To be more precise the element-element contact area is illustrated in Figure 2.9. Only at very high pushforces the element-element contact extends to the pillar, where the body and head of the element are connected [35].

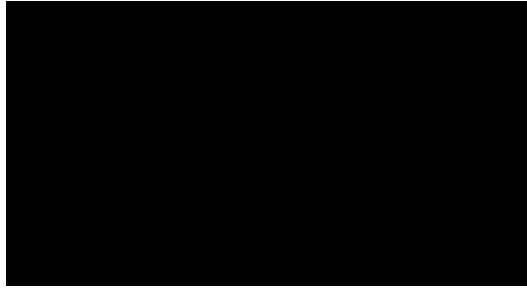


Figure 2.9: Marked element-element contact area

Generally it is assumed that the contact area can be split into an area at the head and at the rocking edge, ignoring the area of the pillar. For each element the pushforce is distributed over these two areas. The ratio in which the pushforce is distributed is not equal for all elements and dependent on numerous factors like the location of the element in the pushpart,  and the loadcase of the pushpart. The exact mechanics behind the way this pushforce distribution originates is still unclear because of the complexity of this effect. However in a previous study by Bosch [35] it has been found that the change in pushforce distribution over the element areas can also change the transversal position of the neutral bending line over which the pushpart bends. Logically the neutral bending line of the pushpart at no load lies at the neutral bending line of the loopsets, since they support the elements. When most of the pushforce is applied at the rocking edge the dominant element-element contact area is also at the rocking edge, towards which the neutral bending line shifts. In the case that the pushforce is mostly applied at the head the element-element contact area at the head is dominant and the neutral bending line of the pushpart shifts towards the head. This effect is illustrated in Figure 2.10 below where the blue arrows indicate the pushforce between elements and the red lines indicate the location of the bending line of the pushpart.

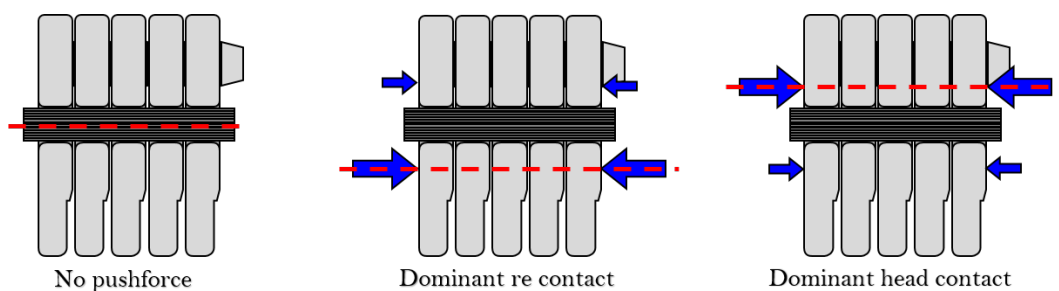


Figure 2.10: Neutral bending line shift for changing dominant element-element contact

Chapter 3

Pushbelt vibration

3.1 Introduction

This investigation is performed because for specific operating conditions of the vehicle driveline vibrations occur causing unwanted noise in the vehicle. The exact cause of these vibrations is explained in this chapter but more importantly a definition is given of the type of pushbelt CVT vibration that is going to be investigated.

3.2 Vibration cause

The total vehicle driveline consists of numerous components. Each of these subsystems has its own natural frequency. The natural frequency of a system is the frequency at which a system tends to vibrate when it is free to do so. Meaning that there are no time-varying disturbances that cause the system to vibrate. The system is in so-called free vibration. When such disturbance does exist the system is in forced vibration. Examples of disturbances are load, displacement or velocity fluctuations exerted on the system. Resonance occurs when the system is forced to vibrate at its natural frequency. Although the periodic force driving the system usually is small, at resonance large amplitude vibrations are produced. Therefore resonance causes the system to vibrate severely resulting in unacceptable noise levels and comfort reduction inside the vehicle.

Force fluctuations in one of the driveline components or external vibrations applied on the vehicle can cause resonance in that component or the other components in the driveline. Extensive research on this topic has shown that driveline vibrations are usually caused by torsional vibrations which typically occur in systems with rotating parts as described by Sheng [26]. Examples of this research for various driveline components are: internal combustion engine [3], drive shaft [18], differential [1]. Internal research by Bosch [17, 22, 37] shows that the CVT itself can also cause torque vibrations between the pulleys and the pushbelt.

3.3 Vibration definition

The torque vibrations arising from one of the driveline components are transferred into the CVT via the primary or secondary pulley. In Figure 3.1 a schematic representation of these vibrations can be seen. Indicated by the yellow arrows are the possible torque vibration transferred into either the primary or secondary pulley. Note that these torque vibrations at either side of the variator can also be directly caused by a fluctuating friction force in the element-pulley contact. These torque vibrations are subsequently transferred to the pushpart as described in Section 2.3.2 resulting in longitudinal load fluctuations in the pushpart. Both the pull- and pushforce are effected by the vibrations since they are coupled. The longitudinal load vibrations result in the pushpart vibrating in transversal direction due to the axial bending freedom in the pushbelt. The pushbelt vibrations are thus defined as the transversal vibrations of the pushpart indicated by the red arrow in Figure 3.1.

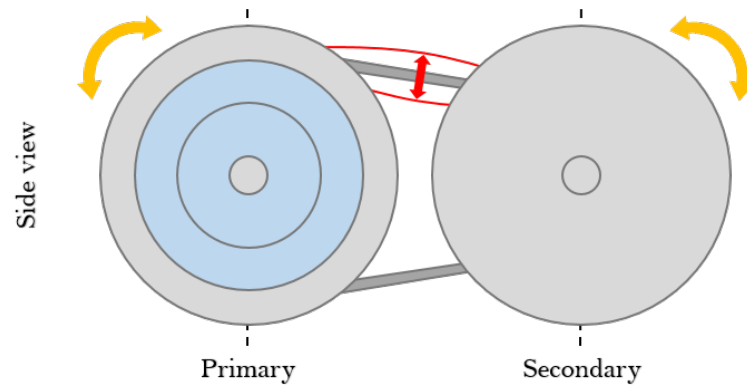


Figure 3.1: Belt vibration

As mentioned in Sections 2.4.1 and 2.4.2 the pushbelt contains both geometrical and material nonlinear properties. This means that the vibration occurring inside the CVT will also contain a form of nonlinearity since the system is nonlinear. However due to the complexity of the working mechanism behind the pushbelt motion and the very limited available knowledge on pushbelt CVT vibration in this study only the linear contribution to the vibration will be taken into account

Chapter 4

Ordinary belt vibration

4.1 Introduction

Within the extent of this literature study an analytic expression for the natural frequency of the pushpart of a pushbelt CVT has not been found. Because of the fact that this type of transmission is highly specialized and such expression does not exist at Bosch it is questionable that publicly available research outside the scope of this literature study indeed provides this expression. In order to get some insides in what basic parameters influence the natural frequency of the pushbelt it is therefore necessary to go back to the basics. Regular belt drives as the Variomatic contain a simple belt which is only loaded by a tensile force. Basic understanding on what parameters influence the vibration frequency of such a belt drive are sought for in this chapter.

4.2 Free vibration

To get some initial understanding on the influence of belt characteristics and external factors for the occurring belt vibration, the free vibration of a stationary ordinary belt represented by either a string, beam and tensioned beam are analyzed.

4.2.1 String vibration

The most simplistic approach assumes that the belt is a string. This means that the belt does not have any bending stiffness. It is assumed that this string only moves in transverse direction $y(x, t)$, has a uniform continuous mass per unit length m and constant length L . The string is simply supported (pinned-pinned) and tensioned by a constant force T as can be seen in Figure 4.1. Note that the tension is not a time-varying disturbance so the string is indeed analyzed for free vibration.

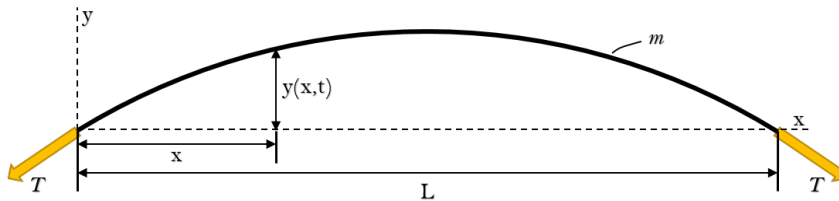


Figure 4.1: String in free bending vibration

Meirovitch [20] described how to analyze the linear natural frequency of a tensioned string by rewriting its equation of motion (EOM) into the corresponding partial differential equation (PDE) as

$$T \frac{\partial^2 y(x, t)}{\partial x^2} = m \frac{\partial^2 y(x, t)}{\partial t^2}, \quad 0 < x < L \quad (4.2.1)$$

The pinned-pinned boundary conditions are formulated as

$$y(0, t) = 0 \quad y(L, t) = 0 \quad (4.2.2)$$

Equations (4.2.1) and (4.2.2) constitute the boundary-value problem for the string. The circumstance is explored under which the motion of the string is synchronous. This means that it is assumed that the string exerts a motion with a unique profile or shape. When this is assumed the boundary-value problem can be separated in spatial variable x and time t in the form

$$y(x, t) = Y(x)F(t) \quad (4.2.3)$$

where $Y(x)$ represents the string profile and $F(t)$ describes how the amplitude of the profile changes over time. Equations (4.2.1) and (4.2.2) are reformulated using (4.2.3) resulting in the boundary-value problem being transformed into the differential eigenvalue problem as

$$-T \frac{d^2 Y(x)}{dx^2} = \omega^2 m Y(x), \quad 0 < x < L \quad (4.2.4)$$

where ω is the radian vibration frequency, with boundary conditions

$$Y(0) = 0 \quad Y(L) = 0 \quad (4.2.5)$$

Since the differential eigenvalue problem for the string is harmonic and of second order its solution can be represented by

$$Y(x) = A \sin \beta x + B \cos \beta x \quad (4.2.6)$$

where A and B are constants of integration and $\beta^2 = \omega^2 m/T$.

By inserting (4.2.6) into (4.2.5) the natural frequencies of the string can be found, which are

$$f_n = \frac{n}{2L} \sqrt{\frac{T}{m}}, \quad n = 1, 2, 3, \dots \quad (4.2.7)$$

where n indicates the n th mode frequency. For $n = 1$ the fundamental frequency is found.

Concluding from (4.2.7) the natural frequency of a freely vibrating string depends on its length, mass and tension.

4.2.2 Beam vibration

Different from previous section most belt drives contain a belt with a bending stiffness that cannot be neglected. The belt can in that case be seen as a beam. It is again assumed that this belt consists of a uniform continuous material with constant mass per unit length m , constant length L and is simply supported (pinned-pinned). The flexural rigidity EI in which E is the modulus of elasticity and I the cross-sectional area moment of inertia is also constant over its length. A schematic representation of the beam can be seen in Figure 4.2 where $y(x, t)$ denotes the transverse displacement.

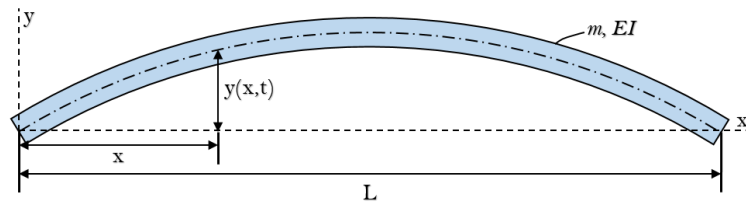


Figure 4.2: Beam in free bending vibration

Similarly to the free vibration of a tensioned string, the free vibration of a beam is described by Meirovitch [20] as well. The method used is identical to the method for the string. The EOM is rewritten into

its corresponding PDE, formulating the boundary-value problem. This problem is transformed into a differential eigenvalue problem by separation in spatial variable x and time t as Equation (4.2.3).

The difference between the string and beam case is the added flexural rigidity of the beam. To include the beam stiffness into the EOM, the Euler-Bernoulli beam theory is used. With this theory rotational inertia and shear deformation are ignored. Ignoring rotational inertia is valid if small deflections are considered. Ignoring shear deformation effects results in underpredicting deflections and overpredicting natural frequencies. As rule of thumb the ratio between length and thickness of the beam needs to be relatively large, more than 10. Otherwise these prediction errors become too large.

Using the method of Meirovitch the PDE for free bending vibrations of a beam becomes

$$-EI \frac{\partial^4 y(x, t)}{\partial x^4} = m \frac{\partial^2 y(x, t)}{\partial t^2}, \quad 0 < x < L \quad (4.2.8)$$

which is a fourth order PDE. To complete the derivation of the boundary-value problem also four boundary conditions must be specified, two at each end of the pushpart. The additional boundary conditions to that of the string state that no torque is experienced at either ends of the beam. For the left and right pinned end the boundary conditions are respectively

$$\begin{aligned} y(0, t) = 0, \quad M(0, t) = EI \frac{\partial^2 y(0, t)}{\partial x^2} = 0 \\ y(L, t) = 0, \quad M(L, t) = EI \frac{\partial^2 y(L, t)}{\partial x^2} = 0 \end{aligned} \quad (4.2.9)$$

The eigenvalue problem is defined as

$$EI \frac{d^4 Y(x)}{dx^4} = \omega^2 m Y(x), \quad 0 < x < L \quad (4.2.10)$$

where ω is the radian vibration frequency, with boundary conditions

$$Y(0) = Y(L) = 0, \quad \frac{d^2 Y(0)}{dx^2} = \frac{d^2 Y(L)}{dx^2} = 0 \quad (4.2.11)$$

Since there are four boundary conditions, two terms are added to Equation (4.2.6) giving the general solution

$$Y(x) = A \sin \beta x + B \cos \beta x + C \sinh \beta x + D \cosh \beta x \quad (4.2.12)$$

where A, B, C and D are constants of integration and $\beta^4 = \omega^2 m / EI$. By inserting (4.2.12) into (4.2.11) the natural frequencies of the beam can be found, which are

$$f_n = \frac{n^2 \pi}{2L^2} \sqrt{\frac{EI}{m}}, \quad n = 1, 2, 3, \dots \quad (4.2.13)$$

From (4.2.13) it can be concluded that the natural frequency of a freely vibrating beam is dependent on its flexural rigidity (bending stiffness), mass and length.

4.2.3 Tensioned beam vibration

The frequency analysis of the beam from the previous section can be extended by loading the beam with a longitudinal force, as is also the case for ordinary belt drives. A constant tension T will be applied to both ends of the beam from figure 4.2 as illustrated in Figure 4.3.

Bokaian [5] described an analytical method to estimate the natural frequencies of beams under tensile loads by using the Euler-Bernoulli beam theory and expanding the EOM from (4.2.8) by adding the axial load term as

$$-EI \frac{\partial^4 y(x, t)}{\partial x^4} + T \frac{\partial^2 y(x, t)}{\partial x^2} = m \frac{\partial^2 y(x, t)}{\partial t^2}, \quad 0 < x < L \quad (4.2.14)$$

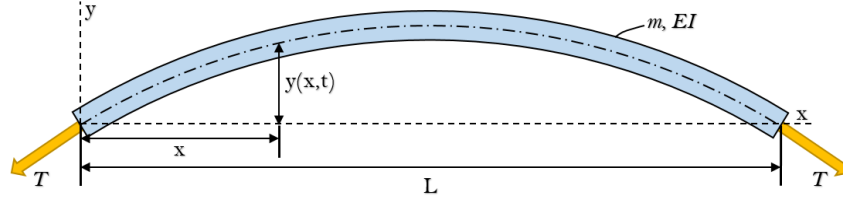


Figure 4.3: Tensioned beam in free bending vibration

and corresponding differential equation

$$EI \frac{d^4 Y(x)}{dx^4} - T \frac{d^2 Y(x)}{dx^2} = \omega^2 m Y(x), \quad 0 < x < L \quad (4.2.15)$$

The boundary conditions remain similar to (4.2.11) as well as the method of solving this differential eigenvalue problem. Different from the differential eigenvalue problem in Section 4.2.2 is the coupling between the natural frequency and the tension for the pinned-pinned beam as

$$\bar{\omega} = \sqrt{1 + \bar{T}} \quad (4.2.16)$$

where $\bar{\omega}$ is the normalized radian vibration frequency and \bar{T} is the normalized tension. Introducing the dimensionless spatial coordinate $\zeta = x/L$ where $0 \leq \zeta \leq 1$, a general solution to (4.2.15) and (4.2.16) is

$$Y(x) = A \sin \Phi \zeta + B \cos \Phi \zeta + C \sinh \Psi \zeta + D \cosh \Psi \zeta \quad (4.2.17)$$

where A, B, C and D are constants of integration, and Φ and Ψ are defined as

$$\Phi = \sqrt{-\hat{T} + \sqrt{\hat{T}^2 + \Omega^2}}, \quad \Psi = \sqrt{\hat{T} + \sqrt{\hat{T}^2 + \Omega^2}} \quad (4.2.18)$$

where $\hat{T} = TL^2/2EI$ is the dimensionless tension parameter and $\Omega = \omega L^2/\sqrt{EI/m}$ is the dimensionless radian vibration frequency parameter.

Solving (4.2.17) finally gives the natural frequency f_n with n being the n th mode as

$$f_n = \frac{n}{2L^2} \sqrt{\frac{n^2 \pi^2 EI + TL^2}{m}} \quad (4.2.19)$$

Equation (4.2.19) shows similarities with both (4.2.7) and (4.2.13). The characteristics of both the free vibration of the string and beam are combined into one equation. The conclusion drawn in Section 4.2.2 can be extended to: The natural frequency of an axially tensioned beam can be changed by altering its flexural rigidity, mass and length of, and load on the beam.

The belt of the CVT is loaded with both a pull- and pushforce. The analysis made above only takes into account a tensile force but not a compressive force. If the beam from Figure 4.3 would have been loaded with a compressive force C the only change in Equation (4.2.19) is a sign change [4] giving

$$f_n = \frac{n}{2L^2} \sqrt{\frac{n^2 \pi^2 EI - CL^2}{m}} \quad (4.2.20)$$

4.3 Belt speed

The natural frequency analyses of the string and beam made in previous sections do not take into account the fact that the belt is rotating. The effect of belt speed can be incorporated into the analysis of the natural frequency by using a type of numerical approximation methods known as weighted residuals. Examples of these methods are the Rayleigh-Ritz method, the Galerkin method and Collocation method. These methods can be used for finding an approximate solution of differential eigenvalue problems. For

finding a solution of the differential eigenvalue problems of Section 4.2 with incorporation of belt speed the Galerkin method is frequently used. For example by Ghayesh [11] and Pakdemirli [19].

Another frequently used method for solving similar differential eigenvalue problems is the method of multiple scales (MMS) belonging to the family of perturbation methods. These methods work by applying small nonlinear perturbations to linearized solutions. They can be applied to weakly nonlinear systems with relatively low amplitudes of motion. The elegance of the MMS is that an approximate analytical solution is sought instead of an approximate numerical solution in the case of the Galerkin method. For this reason the MMS is applied to solve the differential eigenvalue problems described below.

4.3.1 Method of multiple scales

Unlike linear systems, for nonlinear systems like the pushbelt CVT the frequency and amplitude of oscillation are dependent variables. By using the MMS these variables are separated by permitting the solution to be a function of multiple independent time-variables or -scales as described by Thomsen [30]. Fast time-scales are used to find frequencies comparable to the linear natural frequencies of the system and slow time-scales for finding changes in amplitude and phase. Note that the MMS is in this case only used to find the linear natural frequencies. However with this method it is also possible to find the nonlinear natural frequencies.

By using the MMS, the solution $y(x, t)$ is written as a uniformly valid expansion:

$$y(x, t; \epsilon) = y_0(x, T_0, T_1, T_2, \dots) + \epsilon y_1(x, T_0, T_1, T_2, \dots) + \epsilon^2 y_2(x, T_0, T_1, T_2, \dots) + \dots \quad (4.3.1)$$

where y_j , $j = 0, 1, 2, \dots$ are to be determined functions and T_j , $j = 0, 1, 2, \dots$ are independent time-scales as

$$T_j = \epsilon^j t, \quad j = 0, 1, 2, \dots, \quad \epsilon \ll 1 \quad (4.3.2)$$

The first and second order time derivatives of (4.3.1) are

$$\begin{aligned} \frac{d}{dt} &= \frac{dT_0}{dt} \frac{\partial}{\partial T_0} + \frac{dT_1}{dt} \frac{\partial}{\partial T_1} = \frac{\partial}{\partial T_0} + \epsilon \frac{\partial}{\partial T_1} = D_0 + \epsilon D_1 \\ \frac{d^2}{dt^2} &= \frac{\partial(D_0 + \epsilon D_1)}{\partial T_0} + \epsilon \frac{\partial(D_0 + \epsilon D_1)}{\partial T_1} = D_0^2 + 2\epsilon D_0 D_1 + O(\epsilon^2) \end{aligned} \quad (4.3.3)$$

where $D_i^j \equiv \partial^j / \partial T_i^j$.

The expansion (4.3.1) and its time derivatives (4.3.3) are substituted into the system's EOM and coefficients containing powers of ϵ are zeroed. Now a set of perturbation equations are formulated which can be solved by assuming a solution in the form of complex exponentials.

4.3.2 Approximate analysis

To find the influence of the belt speed on the natural frequency of a beam, the MMS will be applied to the beam's EOM from Equation (4.2.14). The belt is axially moving with a constant speed v .

Wickert [42] used the Euler-Bernoulli model together with Hamilton's Principle to formulate the linear, time-dependent, dimensionless EOM of the axially moving beam illustrated in Figure 4.4.

$$\frac{\partial^2 y(x, t)}{\partial t^2} + 2v \frac{\partial^2 y(x, t)}{\partial x \partial t} + \frac{\partial v}{\partial t} \frac{\partial y(x, t)}{\partial x} + v_f^2 \frac{\partial^4 y(x, t)}{\partial x^4} + (v^2 - 1) \frac{\partial^2 y(x, t)}{\partial x^2} = 0 \quad (4.3.4)$$

where $v_f = \sqrt{EI/TL^2}$ is the dimensionless flexural rigidity. Note that terms $\partial^2 y(x, t)/\partial t^2$, $2v \partial^2 y(x, t)/\partial x \partial t$ and $v^2 \partial^2 y(x, t)/\partial x^2$ correspond to respectively the local, Coriolis and centripetal accelerations. Also note that for $v_f^2 = 0$ EOM (4.3.4) is reduced to the EOM of an axially moving string. The boundary conditions for the simply supported beam are formulated as

$$y(0, t) = y(1, t) = 0, \quad \frac{\partial^2 y(0, t)}{\partial t^2} = \frac{\partial^2 y(1, t)}{\partial t^2} = 0 \quad (4.3.5)$$

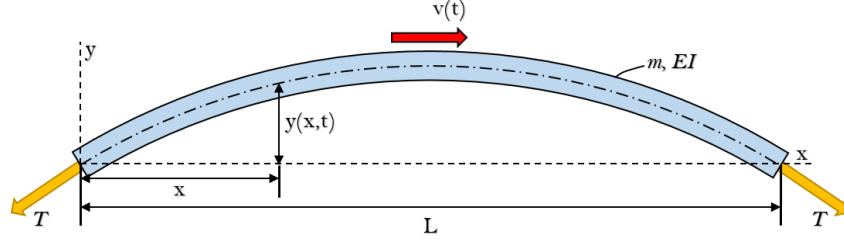


Figure 4.4: Axially moving tensioned beam in forced bending vibration

Öz and Pakdemirli [43] analyzed the dynamic response of an axially moving tensioned beam by applying a harmonically varying velocity to it and using the MMS to do a natural frequency analysis. A varying velocity is applied to find not only the linear natural frequency but also the nonlinear natural frequency by doing a forced vibration analysis. As stated earlier with this method the nonlinear frequency can be found as well but this is not described since this is out of the scope of the study. The velocity can be formulated as

$$v(t) = v_0 + \epsilon v_1 \sin \Omega t \quad (4.3.6)$$

where v_0 is the mean velocity, ϵ is a small parameter and ϵv_1 represents the amplitude of fluctuation. In this case, since the linear natural frequency is analyzed, only the mean velocity v_0 is relevant as becomes clear below.

Substituting equation (4.3.6) into (4.3.4) and keeping terms of only first order of approximation gives

$$\begin{aligned} \frac{\partial^2 y(x,t)}{\partial t^2} + 2v_0 \frac{\partial^2 y(x,t)}{\partial x \partial t} + (v_0^2 - 1) \frac{\partial^2 y(x,t)}{\partial x^2} + v_f^2 \frac{\partial^4 y(x,t)}{\partial x^4} \\ + \epsilon \left(v_1 \Omega \cos \Omega t \frac{\partial y(x,t)}{\partial x} + 2v_1 \sin \Omega t \frac{\partial^2 y(x,t)}{\partial x \partial t} + 2v_0 v_1 \sin \Omega t \frac{\partial^2 y(x,t)}{\partial x^2} \right) = 0 \end{aligned} \quad (4.3.7)$$

Now the MMS can be directly applied to (4.3.7) by substituting (4.3.1) and (4.3.3). For each time-scale the terms are separated as

$$O(1) : D_0^2 y_0 + 2v_0 D_0 \frac{\partial y_0}{\partial x} + (v_0^2 - 1) \frac{\partial^2 y_0}{\partial x^2} + v_f^2 \frac{\partial^4 y_0}{\partial x^4} = 0 \quad (4.3.8)$$

$$\begin{aligned} O(\epsilon) : D_0^2 y_1 + 2v_0 D_0 \frac{\partial y_1}{\partial x} + (v_0^2 - 1) \frac{\partial^2 y_1}{\partial x^2} + v_f^2 \frac{\partial^4 y_1}{\partial x^4} = \\ - 2D_0 D_1 y_0 - 2v_0 D_1 \frac{\partial y_0}{\partial x} - 2v_1 \sin \Omega T_0 D_0 \frac{\partial y_0}{\partial x} \\ - 2v_0 v_1 \sin \Omega T_0 \frac{\partial^2 y_0}{\partial x^2} - \Omega v_1 \cos \Omega T_0 \frac{\partial y_0}{\partial x} \end{aligned} \quad (4.3.9)$$

As explained in section 4.3.1 to find the linear natural frequencies of the system only the fast time-scale equation, (4.3.8), is relevant. Note that this equation only contains the mean velocity v_0 of (4.3.6) as expected.

The solution to (4.3.8) has the form $y_0(x, T_0, T_1) = a(T_1) \cos(T_0 + \phi(T_1))$ [30], but for using the MMS it is more convenient to use complex exponentials. The solution at fast time-scale ϵ^0 is

$$y_0(x, T_0, T_1) = A_n(T_1) e^{i\omega_n T_0} Y_n(x) + \bar{A}_n(T_1) e^{-i\omega_n T_0} \bar{Y}_n(x) \quad (4.3.10)$$

where A_n is an unknown slow time-scale function, $Y_n(x)$ are the spatial functions describing the shape of the beam and ω_n are the radian natural frequencies. The terms with overbar denote the complex conjugates of these terms. Substituting (4.3.10) into (4.3.8) gives the equation

$$v_f^2 \frac{d^4 Y_n(x)}{dx^4} + (v_0^2 - 1) \frac{d^2 Y_n(x)}{dx^2} + 2iv_0 \omega_n \frac{dY_n(x)}{dx} - \omega_n^2 Y_n(x) = 0 \quad (4.3.11)$$

with the boundary conditions from (4.3.5) becoming

$$Y_n(0) = Y_n(1) = 0, \quad \frac{d^2 Y_n(0)}{dx^2} = \frac{d^2 Y_n(1)}{dx^2} = 0 \quad (4.3.12)$$

Solution of equation (4.3.11) is

$$Y_n(x) = c_{1n} (e^{i\beta_{1n}x} + C_{2n} e^{i\beta_{2n}x} + C_{3n} e^{i\beta_{3n}x} + C_{4n} e^{i\beta_{4n}x}) \quad (4.3.13)$$

Coefficients β_{in} satisfy the dispersive relation

$$v_f^2 \beta_{in}^4 + (1 - v_0^2) \beta_{in}^2 - 2\omega_n v_0 \beta_{in} - \omega_n^2 = 0, \quad i = 1, 2, 3, 4, \quad n = 1, 2, \dots \quad (4.3.14)$$

Applying the boundary conditions to the general solution (4.3.13) four equations are obtained, one for each conditions, which can be denoted in the following matrix equation

$$\begin{bmatrix} 1 & 1 & 1 & 1 \\ \beta_{1n}^2 & \beta_{2n}^2 & \beta_{3n}^2 & \beta_{4n}^2 \\ e^{i\beta_{1n}} & e^{i\beta_{2n}} & e^{i\beta_{3n}} & e^{i\beta_{4n}} \\ \beta_{1n}^2 e^{i\beta_{1n}} & \beta_{2n}^2 e^{i\beta_{2n}} & \beta_{3n}^2 e^{i\beta_{3n}} & \beta_{4n}^2 e^{i\beta_{4n}} \end{bmatrix} \begin{bmatrix} 1 \\ C_{2n} \\ C_{3n} \\ C_{4n} \end{bmatrix} c_{1n} = \begin{bmatrix} 0 \\ 0 \\ 0 \\ 0 \end{bmatrix} \quad (4.3.15)$$

where the $[4 \times 4]$ matrix is called the coefficient matrix.

To have non-trivial solutions for C_{2n} , C_{3n} and C_{4n} , the determinant of the coefficient matrix must be equal to zero, which gives the following supporting condition

$$\begin{aligned} & [e^{i(\beta_{1n} + \beta_{2n})} + e^{i(\beta_{3n} + \beta_{4n})}] (\beta_{1n}^2 - \beta_{2n}^2) (\beta_{3n}^2 - \beta_{4n}^2) \\ & + [e^{i(\beta_{1n} + \beta_{3n})} + e^{i(\beta_{2n} + \beta_{4n})}] (\beta_{2n}^2 - \beta_{4n}^2) (\beta_{3n}^2 - \beta_{1n}^2) \\ & + [e^{i(\beta_{2n} + \beta_{3n})} + e^{i(\beta_{1n} + \beta_{4n})}] (\beta_{1n}^2 - \beta_{4n}^2) (\beta_{2n}^2 - \beta_{3n}^2) = 0 \end{aligned} \quad (4.3.16)$$

Using both Equations (4.3.14) and (4.3.16) numerical values of β_{in} and ω_n can be calculated resulting in finding the linear natural frequency of the axially moving beam.

4.4 Extended beam models

In previous sections a method has been described to find the linear natural frequency of an axially moving beam. As described in Section 4.2.2 the Euler-Bernoulli beam model used in this method has some limitations because of assumptions made in the model. It is only applicable for small beam deflections and thin beams. However because of the very limited available knowledge on this topic it is yet unsure if the Euler-Bernoulli beam model can be used for frequency calculations of the pushpart. It is also possible to extend the beam model to the Rayleigh beam model or Timoshenko beam model to include respectively only rotational inertia or both rotational inertia and shear deformation. The MMS described in the previous section fortunately allows for this extension relatively easily. For both extended beam models the application in the MMS is briefly pointed out.

4.4.1 Rayleigh beam model

Using the Rayleigh beam model the dimensionless EOM of the axially moving beam used in Equation (4.3.4) is extended with a rotational inertia term as described by Ghayesh [12] like

$$\begin{aligned} & \frac{\partial^2 y(x, t)}{\partial t^2} + 2v \frac{\partial^2 y(x, t)}{\partial x \partial t} + \frac{\partial v}{\partial t} \frac{\partial y(x, t)}{\partial x} + v_f^2 \frac{\partial^4 y(x, t)}{\partial x^4} + (v^2 - 1) \frac{\partial^2 y(x, t)}{\partial x^2} \\ & - \gamma^2 \left(\frac{\partial^4 y(x, t)}{\partial x^2 \partial t^2} + 2v \frac{\partial^4 y(x, t)}{\partial x^3 \partial t} + \frac{\partial v}{\partial t} \frac{\partial^3 y(x, t)}{\partial x^3} + v^2 \frac{\partial^4 y(x, t)}{\partial x^4} \right) = 0 \end{aligned} \quad (4.4.1)$$

where ϵ is a small parameter and γ includes the rotational inertia like

$$\gamma = \frac{k}{L}, \quad k = \sqrt{\frac{I}{m}} \quad (4.4.2)$$

where k is the radius of gyration, L is the length, I is the inertia, v_f is the dimensionless flexural rigidity, v is the axially speed and m the mass per unit length of the beam.

Substituting (4.3.6) into (4.4.1) and using the MMS the fast time-scale equation becomes

$$O(1) : D_0^2 y_0 + 2v_0 D_0 \frac{\partial y_0}{\partial x} + (v_0^2 - 1) \frac{\partial^2 y_0}{\partial x^2} + v_f^2 \frac{\partial^4 y_0}{\partial x^4} - \gamma^2 \left(D_0^2 \frac{\partial^2 y_0}{\partial x^2} + 2v_0 D_0 \frac{\partial^3 y_0}{\partial x^3} + v_0^2 \frac{\partial^4 y_0}{\partial x^4} \right) = 0 \quad (4.4.3)$$

General solution (4.3.10) is substituted in (4.4.3) as

$$\begin{aligned} (v_f^2 - \gamma^2 v_0^2) \frac{d^4 Y_n(x)}{dx^4} + (-2i\gamma^2 v_0 \omega_n) \frac{d^3 Y_n(x)}{dx^3} \\ + [(v_0^2 - 1) + \gamma^2 \omega_n^2] \frac{d^2 Y_n(x)}{dx^2} + 2iv_0 \omega_n \frac{dY_n(x)}{dx} - \omega_n^2 Y_n(x) = 0 \end{aligned} \quad (4.4.4)$$

Considering (4.3.13) and (4.4.4) the dispersive relation becomes

$$\begin{aligned} (v_f^2 - \gamma^2 v_0^2) \beta_{in}^4 - 2\gamma^2 v_0 \omega_n \beta_{in}^3 + \\ [(1 - v_0^2) - \gamma^2 \omega_n^2] \beta_{in}^2 - 2\omega_n v_0 \beta_{in} - \omega_n^2 = 0, \quad i = 1, 2, 3, 4, \quad n = 1, 2, \dots \end{aligned} \quad (4.4.5)$$

By numerically solving for β_{in} and ω_n using Equations (4.3.16) and (4.4.5) the linear natural frequencies of the axially moving Rayleigh beam can be found.

4.4.2 Timoshenko beam model

By using the Timoshenko beam model next to rotational inertia also shear deformation is taken into account. Ghayesh [13] also described the application of this beam model and used the MMS to find the linear natural frequency of the axially moving beam. For this beam model the angle of rotation due to bending $\phi(x, t)$ is introduced, which is coupled to the transverse displacement $y(x, t)$. The dimensionless set of EOM's becomes

$$\begin{aligned} \frac{\partial^2 y(x, t)}{\partial t^2} + \frac{\partial v}{\partial t} \frac{\partial y(x, t)}{\partial x} + 2v \frac{\partial^2 y(x, t)}{\partial x \partial t} + (v^2 - 1) \frac{\partial^2 y(x, t)}{\partial x^2} - \alpha^2 \left(\frac{\partial^2 y(x, t)}{\partial x^2} - \frac{\partial \phi(x, t)}{\partial x} \right) = 0 \\ \frac{\partial^2 \phi(x, t)}{\partial t^2} + \frac{\partial v}{\partial t} \frac{\partial \phi(x, t)}{\partial x} + 2v \frac{\partial^2 \phi(x, t)}{\partial x \partial t} + (v^2 - \mu) \frac{\partial^2 \phi(x, t)}{\partial x^2} - \beta^2 \left(\frac{\partial y(x, t)}{\partial x} - \phi(x, t) \right) = 0 \end{aligned} \quad (4.4.6)$$

where v , μ and α are respectively the dimensionless axial speed, axial stiffness and shear rigidity with

$$\mu = \sqrt{\frac{EA}{T}}, \quad \alpha = \sqrt{\frac{k_s GA}{T}}, \quad \beta = AL \sqrt{\frac{k_s G}{TI}} \quad (4.4.7)$$

where E is the modulus of elasticity, I the cross-sectional area moment of inertia, T the tension, G the modulus of rigidity, k_s the Timoshenko shear coefficient, A the cross-sectional area and L the length of the beam.

Substituting (4.3.6) into (4.4.6) and using the MMS the fast time-scale set of equations becomes

$$\begin{aligned} O(1) : D_0^2 y_0 + 2v_0 D_0 \frac{\partial y_0}{\partial x} + (v_0^2 - 1) \frac{\partial^2 y_0}{\partial x^2} + v_f^2 \frac{\partial^4 y_0}{\partial x^4} - \alpha^2 \left(\frac{\partial^2 y_0}{\partial x^2} - \frac{\partial \phi_0}{\partial x} \right) = 0 \\ O(1) : D_0^2 \phi_0 + 2v_0 D_0 \frac{\partial \phi_0}{\partial x} + (v_0^2 - \mu) \frac{\partial^2 \phi_0}{\partial x^2} + v_f^2 \frac{\partial^4 \phi_0}{\partial x^4} - \beta^2 \left(\frac{\partial y_0}{\partial x} - \phi_0 \right) = 0 \end{aligned} \quad (4.4.8)$$

Substituting general solution (4.3.13) into (4.4.8) and decoupling $Y_n(x)$ and $\Phi_n(x)$ where $\phi(x, t) = \Phi(x)F(t)$ gives the set of equations

$$\begin{aligned} b_1 \frac{d^4 Y_n(x)}{dx^4} + b_2 \frac{d^3 Y_n(x)}{dx^3} + b_3 \frac{d^2 Y_n(x)}{dx^2} + b_4 \frac{dY_n(x)}{dx} + b_5 Y_n(x) = 0 \\ b_1 \frac{d^4 \Phi_n(x)}{dx^4} + b_2 \frac{d^3 \Phi_n(x)}{dx^3} + b_3 \frac{d^2 \Phi_n(x)}{dx^2} + b_4 \frac{d\Phi_n(x)}{dx} + b_5 \Phi_n(x) = 0 \end{aligned} \quad (4.4.9)$$

where

$$\begin{aligned} b_1 &= (\mu^2 - v_0^2)(v_0^2 - 1 - \alpha^2), & b_2 &= -2iv_0\omega_n(2v_0^2 - 1 - \alpha^2 - \mu^2), \\ b_3 &= \omega_n^2(6v_0^2 - 1 - \alpha^2 - \mu^2) - \beta^2(v_0^2 - 1), & b_4 &= 4iv_0\omega_n^3 - 2i\beta^2v_0\omega_n, \\ b_5 &= \omega_n^2(\beta^2 - \omega_n^2) \end{aligned} \tag{4.4.10}$$

Considering (4.3.13) and (4.4.9) the dispersive relation becomes

$$b_1\beta_{jn}^4 - ib_2\beta_{jn}^3 - b_3\beta_{jn}^2 + ib_4\beta_{jn} + b_5 = 0, \quad j = 1, 2, 3, 4, \quad n = 1, 2, \dots \tag{4.4.11}$$

Finally using Equations (4.3.16) and (4.4.11) the linear natural frequency of the axially moving Timoshenko beam can be found.

Chapter 5

Bosch models

5.1 Introduction

[Redacted text block]

5.2 [Redacted]

[Redacted text block]

5.3 [Redacted]

[Redacted text block]

5.4 [Redacted]

[Redacted text block]

[REDACTED]

5.5 [REDACTED]

[REDACTED]

5.6 [REDACTED]

[REDACTED]

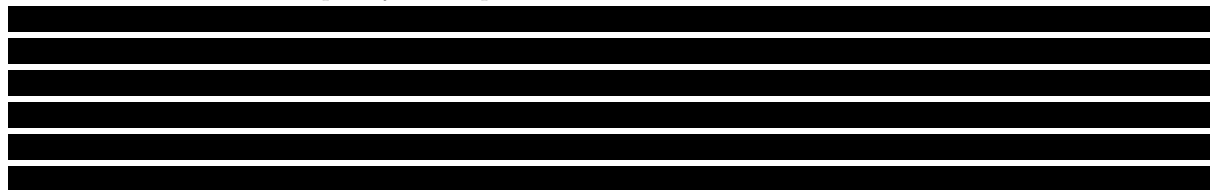
Chapter 6

Conclusion: literature study

Noise originating from the driveline of the vehicle is increasingly subjected to stricter requirements. This includes the noise coming from the CVT pushbelt vibrations that is caused by torque vibration in either the CVT itself or other driveline components. In theory the pushbelt could be designed so resonance resulting in noise is significantly reduced. Knowing the relation between different belt parameters and effects occurring in the belt and their effect on the natural frequency of the pushbelt is crucial.

The pushbelt CVT is a highly complex piece of engineering as turned out in Chapter 2. The CVT shares some basic mechanisms with a regular belt drive or regular CVT. However the pushbelt, being an assembly of the loopsets and elements, gives this transmission a whole new dimension. Due to the combination of the loopsets and the elements the belt is loaded with both a tensile and compressive force called pull- and pushforce. The compression of the elements under pushforce is nonlinear causing a nonlinear relation in the 'growth' of catsback in the pushpart as well as a nonlinear relation between pull- and pushforce. Next to that the element-element contact is divided into both a contact in the rocking edge and the head. Depending on the point of application of the pushforce between the elements the pushforce is distributed over either the rocking edge or head or a combination of both.

From Chapter 4 it can be concluded that the natural frequency of an ordinary belt drive, represented by an axially moving simply supported beam, depends on the mass, flexural rigidity, length and velocity of the belt as well as the axial load applied to the belt. This means that it is expected that the natural frequency of a CVT pushbelt should at least also depend on these parameters. However the flexural rigidity of, and axial load on a pushbelt have not been investigated sufficiently to be able to design a relation for the natural frequency of the pushbelt.



Overall it can be stated that more research on several topics is necessary to achieve the ultimate goal described in the introduction. These topics are:

- The resemblance of the natural frequency of the pushbelt compared to that of an ordinary belt.
- The influence of belt parameters and external factors on the pushbelt's flexural rigidity.
- The influence of the pushforce distribution on the natural frequency of the pushbelt.

Besides from investigating these topics possibly even more valuable knowledge can be gained by actually performing frequency measurements to find the natural frequency of the pushpart. Until now these kind of measurements have not been performed by Bosch and could not be found within the scope of this literature study. These measurements could give insights in the change in natural frequency for increasing loads or other belt parameters.

Part II

Master Thesis

Chapter 7

Research scope

7.1 Introduction

Although several models designed by Bosch are able to calculate the vibration frequency of the pushpart or simulate its vibration motion, natural frequency measurements of the pushpart have not been performed until now. These kind of measurements could however be used as a powerful resource to get more insights in the mechanism behind the belt vibrations.

During CVT operation the pushpart is subjected to longitudinal load fluctuations causing forced vibration in the belt. To measure the natural frequency of the pushpart the free vibration of the belt should be examined. This means that the frequency measurements should be performed on a stationary pushpart. This however raises a lot of questions. During belt operation the pushpart can move with respect to both pulleys for changing ratio thereby changing in length. Depending on the longitudinal load on the pushpart a catsback shape arises also effecting the load on and length of the pushpart, see Section 2.4.2. It is therefore necessary to define a framework in which the natural frequency of the pushpart is investigated.

7.2 Parameter selection

As described in Chapter 6 from the literature study it was concluded that the natural frequency of the pushpart is most likely depending on at least the mass, flexural rigidity, length and velocity of the belt as well as the axial load applied to the belt. By examining a stationary pushpart by definition the speed dependency of the pushpart is not included in the scope of this research. Desirably the other four parameters are incorporated in the investigation. Selecting a tool for measuring the natural frequency of the pushpart however resulted in ruling out two of the four parameters, namely the mass and length, which will remain constant. The limitations of the tool will be explained in Chapter 8.

7.3 Boundary conditions

Since the pushpart is examined as separate system excluded from the entire pushbelt it is important to define the boundary conditions for the pushpart. As stated earlier in Chapter 2 the pushpart can move in longitudinal and transversal direction with respect to the pulleys and is also free to axially rotate at its ends due to the rotational freedom between the elements. The translational movements of the pushpart are neglected for this study since the pushpart vibrations occur at specific operating conditions meaning that no significant change in ratio or catsback shape is expected. The rotational freedom of the pushpart at both ends is however important for the way the pushpart vibrates. Translating these conditions to boundary conditions of the pushpart it is concluded that the pushpart is simply supported at both ends.

7.4 System schematic

With the definition of the system and its boundary conditions a schematic representation of the pushpart that is analyzed in this study is presented in Figure 7.1.

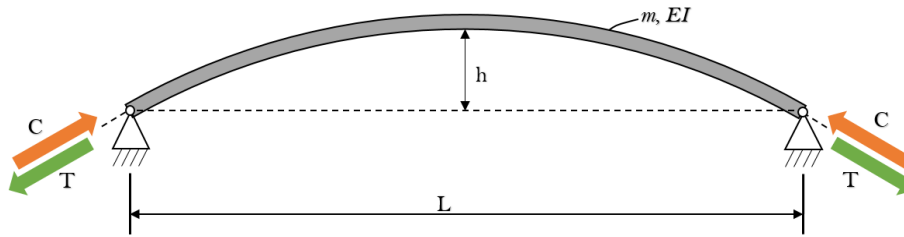


Figure 7.1: Pushpart schematic

Here the pushpart assembly is represented by the gray curved bar. m , h , L and EI indicate respectively the mass, catsback height, length and flexural rigidity of the pushpart. T and C are respectively the tension and compression forces applied on the pushpart. Note that the system neatly corresponds to the cases described in Chapter 4. Outcomes of frequency measurements can therefore be compared to the models for ordinary belt drives directly.

7.5 Assumptions

By stating that the pushpart is represented by the schematic from Figure 7.1 several assumptions have been made. These assumptions are listed below:

- The length of the pushpart is constant.
- The mass of the pushpart is constant.
- The pushpart is stationary, e.q. no longitudinal speed.
- The pushpart is simply supported at both ends.
- The effect of gravity on the pushpart is negligible.
- The pull- and pushforce are assumed to apply to the pushpart ends in its longitudinal direction.

The assumption that the effect of gravity can be neglected is supported by the fact that the mass of the pushpart is around 350 grams corresponding to a gravitational force of $0.35 \cdot 9.81 = 3.4$ N. Compared to the several hundreds and thousands of newtons pull- and pushforce that are applied to the pushpart the gravitational force is negligible.

Chapter 8

Measurement setup

8.1 Introduction

At Bosch a specific tool for measuring the natural frequency of a pushbelt does not exist. Therefore a tool normally serving another purpose is used for the natural frequency measurements of the pushpart. This tool, called the compression tool, is used to measure the compressibility of the pushpart by isolating the pushpart of the belt. With some modifications this tool is used for natural frequency measurements. In this chapter it is explained how this tool is modified. The scope of the measurements is presented, together with a sensors and instruments list, a measurement procedure and tool validation.

8.2 Compression tool

The tool that is used for the frequency measurements is the pushpart compression tool as designed by Bosch. This tool is used to measure the longitudinal compression of the pushpart for specific loadpaths. The pushpart assembly is span in the tool as shown in Figure 8.1. The loopsets are clamped between clamping blocks at both ends. In the tool these clamping blocks are pulled apart so the loopsets are tensioned.

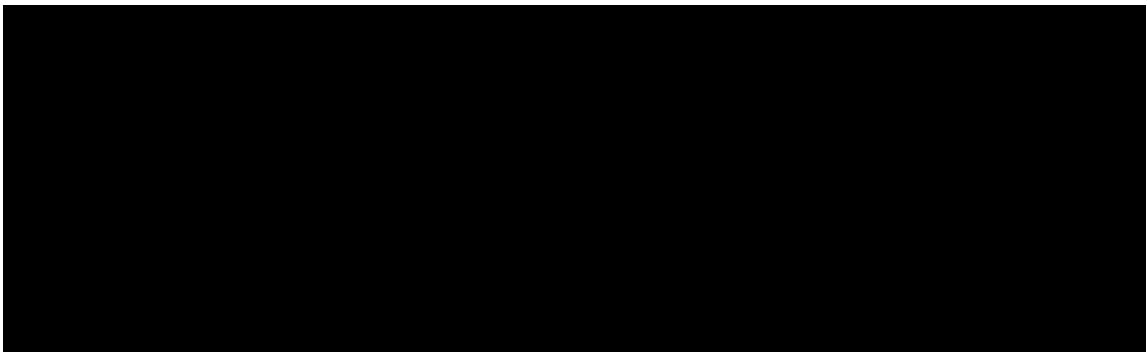


Figure 8.1: Pushpart assembly

On one side the clamping block is fitted with a ball bearing to remove any unwanted longitudinal torsional load in the pushpart. The elements are fitted in between the loopsets similarly to a normal pushbelt assembly. At both ends of the element string a push block is fitted. The pink rods at both the top and bottom are part of the push block. In the tool these push blocks are pushed towards each other to load the element string with a pushforce.

In Figure 8.2 the pushpart assembly is placed in the tool. One side of the pushpart is displayed. At both ends the clamping block is attached to the tool using a locking pin. The push block is fitted within

the support block by clamping the pink rods of each push block. The pink rods allow the push block to rotate along the transversal axis.

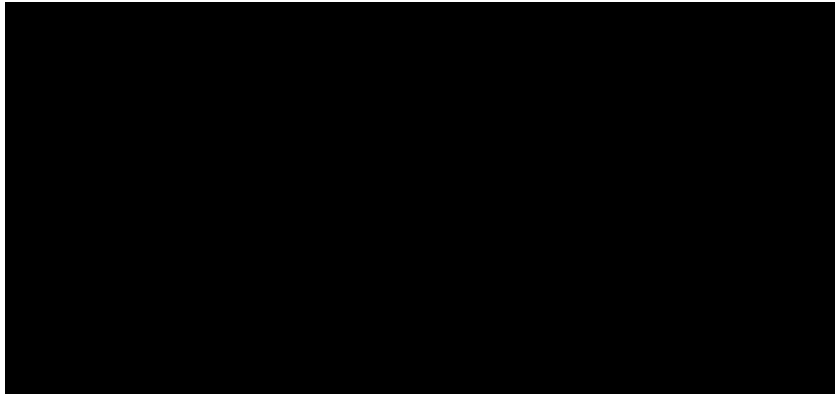


Figure 8.2: Pushpart assembly in compression tool

The entire compression tool can be seen in Figure 8.3. In the middle of the tool the pushpart assembly is span and at each side the support blocks are clearly visible. The support blocks act as levers. These levers can rotate as indicated by the red arrows. At the other side of the levers two counterweights are fitted. The reason the tool allows this rotational freedom is because of the changing shape of the pushpart while loaded with a pull- and pushforce. When the pushpart arcs into a catsback the support blocks rotate upwards so the pushforce acting on the push blocks is still applied in longitudinal direction of the pushpart. The counterweights balance the weight of the support blocks and levers so they do not influence the loadcase applied to the pushpart assembly. By tightening both the push- and pullforce nut the pushpart assembly can be loaded to a specific loadcase.

When the compression tool is used, the loopsets are tensioned to a specific pullforce. Then the pushforce is gradually increased until the loadcase boundary, as indicated in Figure 2.7, is reached. Both push- and pullforces are measured by load cells. Simultaneously the distance between both push blocks is measured to track the compression of the pushpart. The compression is measured by two displacement sensors placed directly against the push blocks.

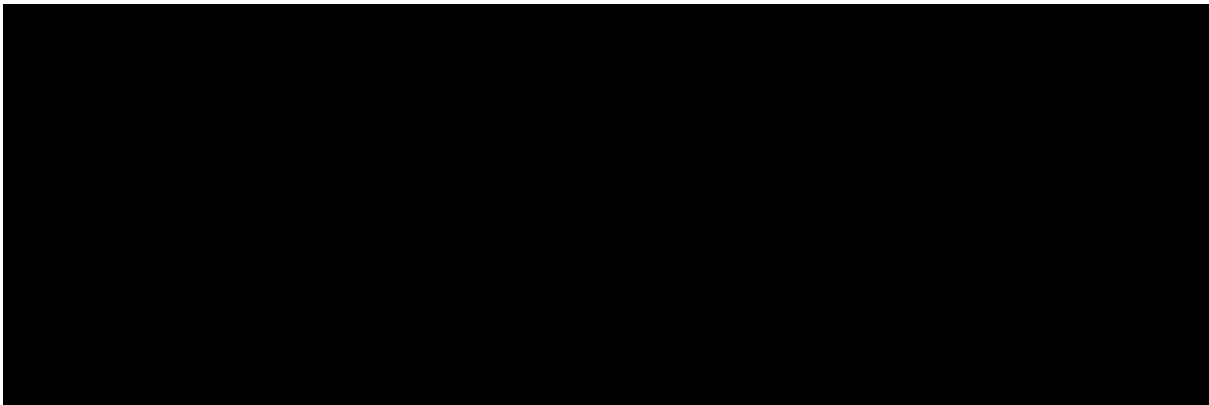


Figure 8.3: Compression tool

8.3 Tool modifications

As explained in Chapter 4.2 the mass of a vibrating belt directly influences its natural frequency. In the case of the compression tool the levers move along with the belt's motion adding a significant amount of weight to the system and thus influencing the frequency measurement. It is possible to compensate for

this added mass afterwards, but this is not desired. It is however not possible to remove the levers since the pushpart is span in between them. The only way to exclude the influence of the mass of the levers is by preventing the levers from moving. The rotational freedom of the levers is therefore constrained. This tool modification comes with a couple of important consequences. As a result of the fixation of the levers, the pushpart is unable to move in longitudinal and transverse direction at both ends. Because of the push blocks pressing against the pushpart the end-elements of the element string are not able to rotate around the axial axis. Meaning the pushpart is clamped at both ends, negatively influencing the catsback shape. To give the pushpart the ability to rotate freely at both ends the head of the end-elements is grinded off. One of the grinded off elements can be seen in Figures 8.4 and 8.5.

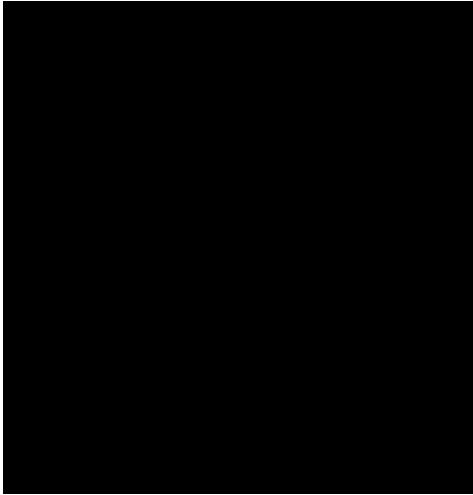


Figure 8.4: End-element side view

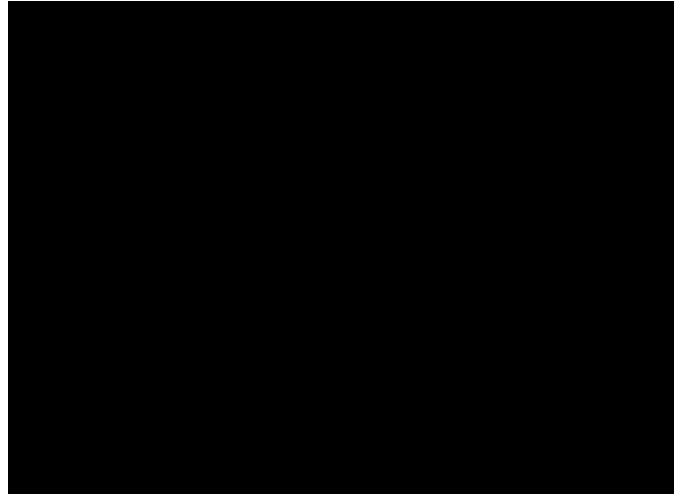


Figure 8.5: End-element 3D view

This can be done under the assumption that the pushforce at both ends of the pushpart is passed on through the rocking edge. This assumption is commonly made at Bosch and also applied in the Catsback model. A drawback of this modification is that the measured pull- and pushforce does not directly correspond to the actual pull- and pushforce in the pushpart for increasing catsback because the centerlines of the sensors lose their alignment with the longitudinal axis of the pushpart. The misalignment between actual forces applied to the pushpart and the measured forces is visualized in Figure 8.6, respectively indicated by the red and black arrows. In the end the fixation of the levers and application of the adjusted end-elements results in the pushpart being simply supported corresponding to the research scope from previous chapter.

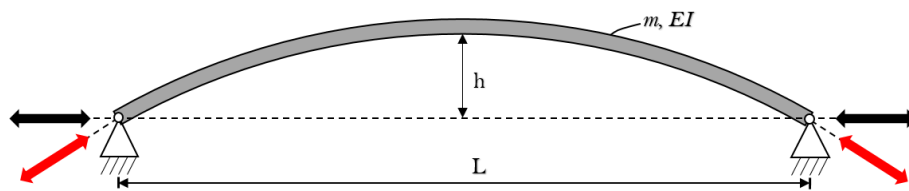


Figure 8.6: Misalignment forces in pushpart and measured forces

Other modifications are made to the tool to be able to measure the parameters necessary to find the vibration frequency. The tool is fitted with an additional displacement sensor. A hall sensor will measure the transversal displacement of the pushpart at its center. From the displacement signal the vibration frequency can be derived. Normally an accelerometer is used to measure the vibration. However the uneven surface of the pushpart does not allow the accelerometer to be fitted robustly. Since the displacement sensors located in the push blocks are not used during the frequency measurements, they are removed from the tool.

The natural frequency of the pushpart is measured doing a hammer impact test. The pushpart is subjected

to an impulse load in transversal direction at the center of the pushpart to initiate the free vibration of the pushpart. The hammer is fitted with a load cell in the tip. The input signal from the hammer is used as trigger to start each frequency measurement.

Pictures of the modified measurement tool and pushpart assembly can be found in Appendix A.

8.4 Assumptions

By modifying the compression tool in order to perform frequency measurements some assumptions have been made. These assumptions are listed as:

- The vibration frequency of the pushpart is not affected by the mass of the compression tool levers because the levers are fixed.
- The pushforce at both ends of the pushpart is applied fully at the rocking edge of the elements.
- Fitting the pushpart with modified end-elements gives the pushpart sufficient rotational freedom to retain a catsback shape according its loadcase.
- The misalignment of the pull- and pushforce sensor centerlines with the longitudinal axis of the pushpart for increasing catsback resulting in an offset in actual and measured pushforce in the pushpart is negligible.

The last assumption regarding the negligible difference between measured and actual pull- and pushforce can be supported by the fact that the end-elements in the pushpart pitch at most several degrees for a high catsback shape. This means the measured force is at most a factor $\cos(5^\circ) = 0.996$ of the actual force. This difference is indeed negligible.

8.5 Scope

As mentioned in Section 7.2 the influence of both the mass and length of the pushpart are not incorporated in the research scope. Due to limitations of the tool the length of pushpart can only be changed by the thickness of one element. Furthermore the narrow spread in element mass and size produced at Bosch limits the change in mass of the pushpart. It is therefore expected that differences in results for varying length and mass of the pushpart are too small to draw conclusions. Regarding the flexural rigidity at Bosch a belt parameter that is frequently linked to have an effect on this property is EI , [15]. Because of this hypothesis and its possible effect on the natural frequency four belts have been chosen for the frequency measurements. These four belts share the same material and geometric properties except for one, the EI . The four belts are listed in Table 8.1 and have been given a unique belt ID which is used to keep them apart for the remainder of the report. Note that these four belts have loopsets with ten loop layers each.

Table 8.1: Belts selected for frequency measurements

EI	EI	EI	Belt ID
EI	EI	EI	Belt A
EI	EI	EI	Belt B
EI	EI	EI	Belt C
EI	EI	EI	Belt D

For all four belts frequency measurements are performed at varying loadcases. To be able to compare the four belts as much as possible five different loadpaths, starting from five different initial pullforces, are selected. The natural frequency is measured along these loadpaths for all four belts similarly. In this way the dependency of EI , possibly resembling some flexural rigidity effect, and varying loadcases on the natural frequency of the pushpart can be analyzed.

8.6 Sensors and data acquisition

In Tables 8.2 and 8.3 respectively all sensors and hard- and software used for the frequency measurements are listed. The pull- and pushforce and hammer and hall sensor signals are retrieved using separate data acquisition systems (DAQ). In Figure 8.7 a schematic representation of the measurement setup is displayed. The numbers and letters in the figure correspond to the ID tags from the tables.

Table 8.2: Sensorlist frequency measurements

Sensor	Brand	Model	Max range	ID
Cylindrical loadcell (pullforce)	TesT	K304M.5 kN	$\pm 5\text{kN}$	I
Dual cylindrical loadcell (pushforce)	Althen	FLF256-Z4082	$\pm 10\text{kN}/\pm 200\text{N}$	II
Impulse hammer force sensor	PCB	086C03	$\pm 2225\text{N}$	III
Hall sensor (transverse vibration)	-	MPU 1101-1	-	IV

Table 8.3: DAQ hard- and software list

DAQ hard- & software	Manufacturer	Model	Version	ID
LMS Scadas	Siemens	XS	5.06	A
LMS Test.Lab	Siemens	-	16a	B
Catman Easy	HBM	-	4.2.1	C
MGCplus	HBM	AB22A	-	D
2 Channel DMS amplifier	Althen	SG-2K-IP	-	E

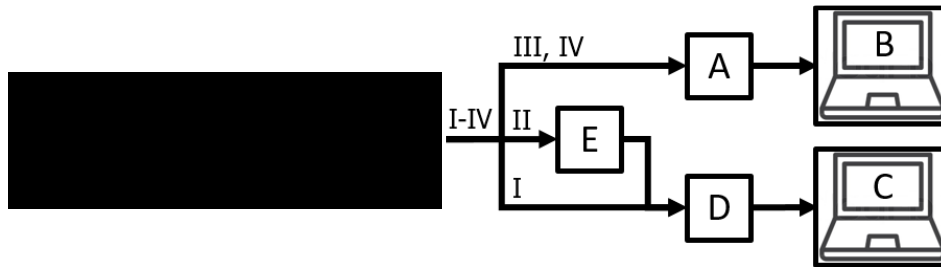


Figure 8.7: Measurement setup

8.7 Procedure

The frequency measurements on the pushpart have been performed by following a specific measurement procedure. Effects in the measurement results like hysteresis or drift can be reduced to a minimum when this procedure is followed. The procedure consists of two parts; the first for setting up the tool and the second for performing the frequency measurements. If both checklists are executed correctly after each measurement data for both the pull- and pushforce, the impact hammer force and hall sensor are retrieved.

8.7.1 Tool setup

The modified compression tool is set up by going through the following checklist:

1. Assemble the pushpart by fitting ■ elements (including both end-elements) and the push blocks between the loopsets and clamp the loopsets in between the clamping blocks. It is important to slightly tension the loopsets before tightening the bolts of the clamping blocks to avoid misalignment of the pushpart.

2. Insert the pushpart assembly in the tool and place the locking pins so the pushpart assembly is span in the tool.
3. Tighten the pushforce nut until the pink pins of the push blocks from Figure 8.1 are fixed within the support blocks.
4. Align both levers horizontally using a level and support both support blocks and counterweights using four in height adjustable rigid supports.
5. Place the hall sensor above the center of the pushpart. Note that during pushpart vibration the sensor may not come in contact with the elements, adjust the height of the sensor accordingly.
6. Connect all sensors to the DAQ systems as indicated in Figure 8.7.

8.7.2 Measurement setup

The frequency measurement are performed according following checklist:

1. Power up all DAQ systems. It is recommended to use two separate computers to be able to monitor the loadcase of the pushpart and to perform the frequency measurements simultaneously.
2. Setup the Catman Easy software such that both pull- and pushforce are displayed and updated continuously.
3. Setup the LMS Test.Lab software by using the built-in impact hammer test template. Within this template the impact hammer can be tuned to act as a trigger for starting the impact measurement.
4. Make sure the pushpart is not loaded by any pull- or pushforce and zero both cylindrical load cells.
5. Tighten the pullforce nut to load the pushpart with the desired pullforce. Note that the tension may never exceed the sensor limit of ████████.
6. To get rid of hysteresis increase the pushforce in the pushpart till ████████ by tightening the pushforce nut. Subsequently unload the pushpart from all pushforce. Most likely the pullforce has decreased. If so again increase the pullforce to the desired amount. Repeat this complete step until the pullforce does not significantly decrease anymore. Most of the hysteresis is now out of the system.
7. Bring the pushpart into the desired loadcase by tightening the pushforce nut to the desired pushforce.
8. The pushpart is in its desired loadcase and the frequency measurement can be performed. Make sure to perform several measurements for each loadcase to average out any unwanted fluctuations in the measurement. In this case an average of five measurements was selected.

8.8 Tool validation: loopset measurement

A test measurement has been performed prior to the pushpart measurements to validate if it is possible to perform accurate natural frequency measurements with the modified compression tool. A single loopset of four stacked loops has been span in the tool and loaded with a specific tension. In Appendix A pictures of the tool validation can be found. A similar test has been performed as described in the Bosch report by Van Engelen [41]. Since the loopset can be substituted by a beam of similar material and dimensions, the natural frequency can easily be calculated using Equation 4.2.19. The four layer loopset has width $w = \text{████████}$ m, height $h = \text{████████}$ m, length $l = \text{████████}$ m, density $\rho = \text{████████}$ kg·m⁻³ and Young's modulus $E = \text{████████}$ GPa. The cross-sectional moment of inertia is defined as $wh^3/12$ m⁴. The calculated and measured results are plotted in Figure 8.8 and the percentual measurement error is plotted in Figure 8.9.

From the figure it can be concluded that the natural frequency of the four layer loopset can be measured accurately using the modified tool. The absolute percentual error of the measurement compared to

the calculation does not exceed two percent which is assumed sufficiently accurate. Regarding the tool modifications it can be concluded that the applied fixation of the levers does indeed eliminate their mass having an effect on the natural frequency of the pushpart.

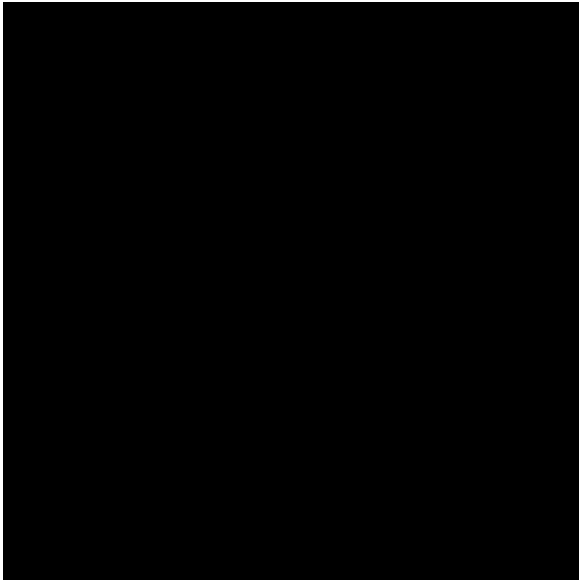


Figure 8.8: Four layer loopset test measurement

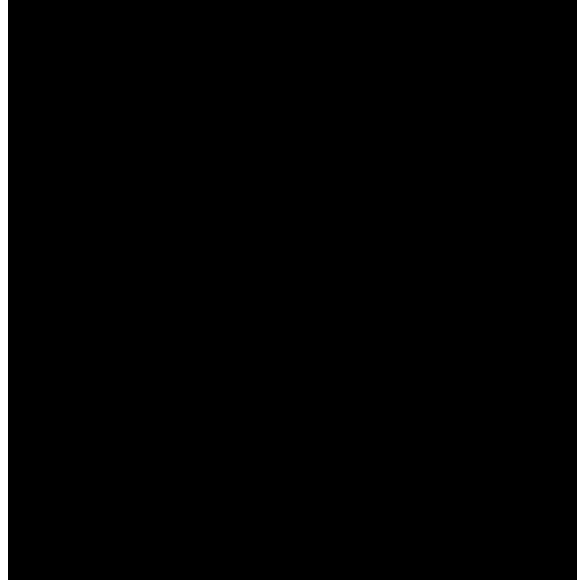


Figure 8.9: Four layer loopset test error

Chapter 9

Frequency measurement results

9.1 Introduction

The frequency measurements performed according the procedure described in previous chapter on the four belts from Table 8.1 are presented in this chapter. Since the measurements produced a substantial amount of data, the data from one of the belts is presented first followed by a comparison of the four belts. For all measurement results please refer to Appendix B.

9.2 Single belt

The measurement results of belt B are presented separately in this section. During measurements this belt turned out to be easiest to set up for the different loadcases. As a result this belt also shows the most consistent data, meaning without a lot of outliers or irregularities in trends.

9.2.1 Loadpaths

To get a clear picture of the outcomes of the measurements it is important to know for what loadcases and loadpaths measurements have been performed. In Figure 9.1 all measured loadcases are plotted. A distinction between the five loadpaths is clearly seen. These loadpaths are located within the triangle indicated by the black bold line. This triangle was defined by both the range of the pullforce sensor and the boundary introduced in Section 2.4.1.

The different loadpaths start at initial pullforces of approximately [REDACTED] and [REDACTED]. These values are equal for all four belts and were chosen by trial and error to spread out the loadpaths evenly across the triangle of Figure 9.1. Furthermore note that the loadpaths indeed show a nonlinear relation between pull- and pushforce as stated in Section 2.4.1.

9.2.2 Frequencies

At each loadcase an impact hammer test was performed resulting in a frequency response function (FRF). An example FRF of belt B is shown in Figure 9.2. The peak at [REDACTED] indicates the natural frequency of the pushpart. Damping is proportional to the width of the peak, which in this case indicates that there seems to be limited damping.

When the FRF of all measured loadcases of the belt are placed next to each other a color map can be created to show the frequency spectrum for varying pull- and pushforce. In Figure 9.3 a color map of the frequency response of belt B for the yellow loadpath of Figure 9.1 is shown. For very low pushforces the natural frequency of the pushpart is between [REDACTED] but increases significantly for increasing pushforce. At [REDACTED] pushforce a change in trend is seen because for increasing pushforce the natural frequency does not increase as significant as for low pushforces. In fact the natural frequency seems to stagnate to a maximum of around [REDACTED] at the end of the loadpath.

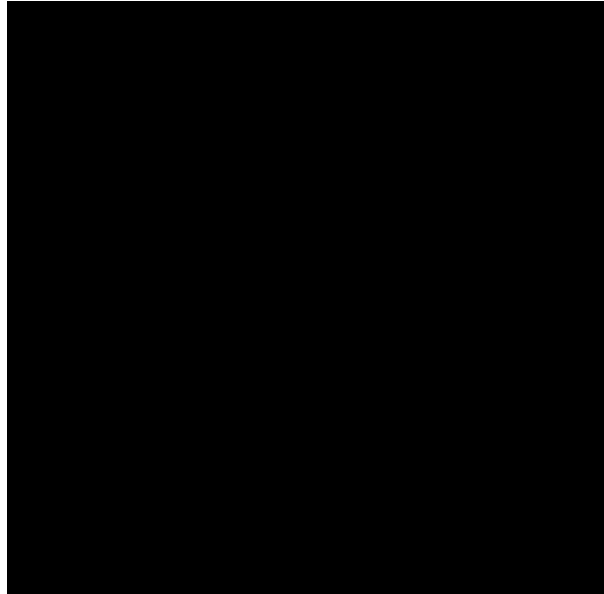


Figure 9.1: Measured loadpaths belt B

For all five loadpaths a color map as Figure 9.3 can be made. However comparing them is not that easy. To overcome this problem for every loadcase that is measured the peaks of its corresponding FRF are analyzed. It turned out that not all FRF's are like Figure 9.2 but sometimes show multiple peaks, at different frequencies. An example FRF showing this phenomenon can be seen in Figure 9.4. For this particular loadcase three peaks are present in the FRF although this cannot be seen directly from the color map. Note that this FRF corresponds to a loadcase also located in the yellow loadpath from before.

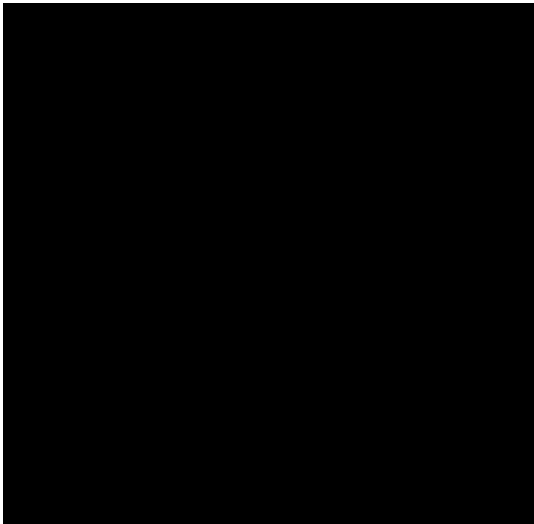


Figure 9.2: Belt B: FRF at single loadcase

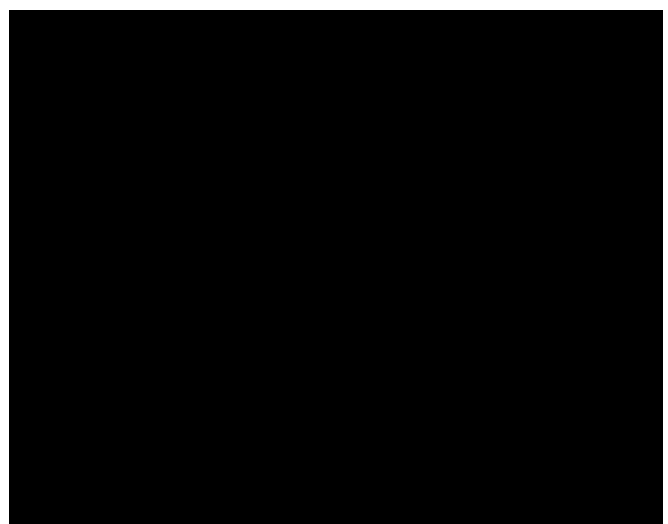


Figure 9.3: Belt B: FRF contour at single loadcase

To get a more detailed picture of the frequency variation along the loadpath for all loadcases all peaks in their corresponding FRF's have been plotted in Figure 9.5. The size and transparency of each dot in the graph depends on the height of the peak at that frequency, where the highest peak gives a large and black dot. For the frequency a similar trend can be seen as found in Figure 9.3. At relatively small pushforces the natural frequency of the pushpart is increasing fast for increasing pushforce. But for large pushforces the frequency seems to stagnate at around [REDACTED]. The gap in the color map around [REDACTED]

is also shown. In fact if the change in frequency along the loadpath is followed, a jump or shift occurs twice. At frequencies of [REDACTED] indicated by the yellow and purple lines respectively the peaks fade out eventually while a peak frequency above [REDACTED] fades in and remains present till the end of the loadpath.

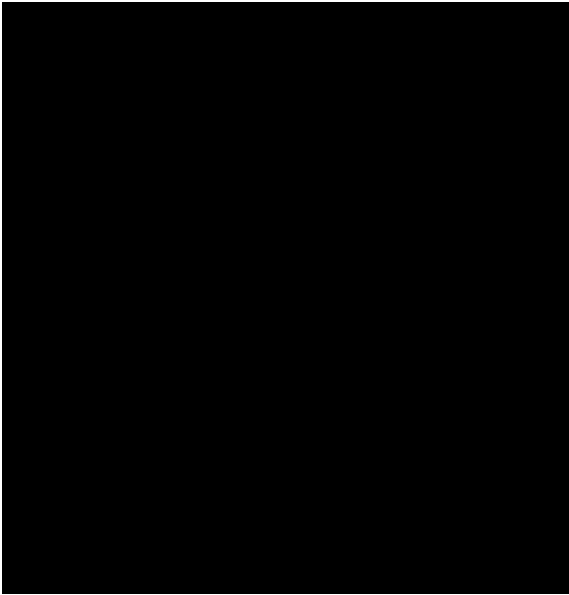


Figure 9.4: Belt B: FRF at single loadcase

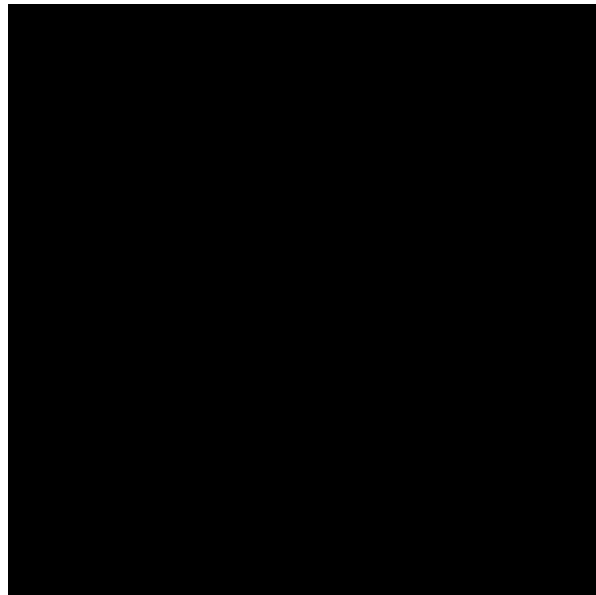


Figure 9.5: Belt B: peak frequencies loadpath

To illustrate more clearly how Figure 9.5 was created the peak frequencies from Figure 9.4 indicated at the red, blue and green dotted lines are highlighted similarly in Figure 9.5. Note that the pushforce indicated by the gray dotted line corresponds to the pushforce of the loadcase of the plotted FRF. For Figure 9.5 a final remark has to be made regarding the respectively small and transparent dots in the low pushforce region, at frequencies around and above [REDACTED]. These peaks are the result of the way the peak frequencies have been found in the post-processing algorithm and can be derived from minute fluctuations in the FRF graph, as can for example be seen in Figure 9.4 at frequencies above [REDACTED].

All frequency measurements for the five loadpaths of Belt B can now be compared. In Figures 9.6 and 9.7 the measured peak frequencies for all five loadpaths are plotted against respectively the push- and pullforce. Only the three peak frequencies with the highest amplitude are plotted for each loadcase since the figure would otherwise be hard to read because of the amount of data points. Ignoring all other data points is admissible since the vibration amplitude at these frequencies is relatively low, e.g. <30%, compared to the peak frequency with the highest vibration amplitude. Next to that the trend in the frequency variation along the loadpaths remains visible.

In Figure 9.6 it can be seen that for a loadpath with a higher initial pullforce the frequency reaches a higher frequency at the end of the loadpath. This matches the general relation that increasing tension in a system increases its natural frequency as seen in Equation 4.2.19 and Figure 8.8. For increasing pushforce the natural frequency also increases. As seen earlier this happens very fast in the low pushforce range and stagnates at the end of each loadpath. The fact that the vibration frequency increases for increasing pushforce is contradicting the relation between compressional load and natural frequency in Equation 4.2.20 where exactly the opposite occurs. This observation will be discussed more thoroughly in Chapter 11.

Visible in both figures is a gap in the frequency variation along the loadpath as seen earlier in Figure 9.5. This phenomenon is however not a gap but more a transition area where for increasing load on the pushpart the lower frequency in the region between [REDACTED] fades out and the higher frequency in the region [REDACTED] fades in. Concealed in Figure 9.6 but clearly visible in Figure 9.7 is a second smaller

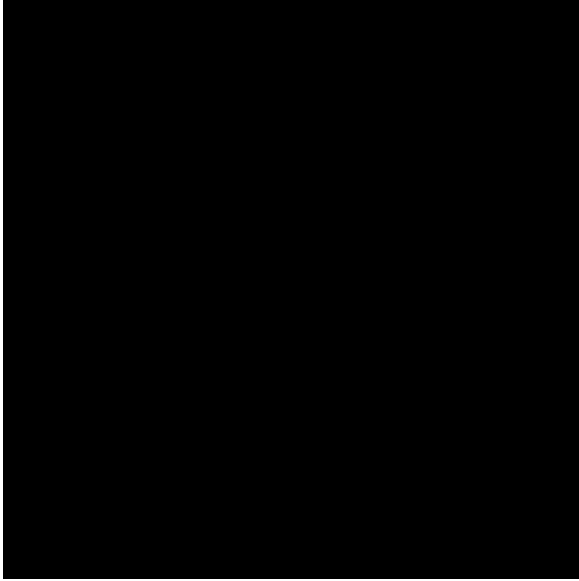


Figure 9.6: Belt B: peak frequencies for all loadpaths vs. pushforce

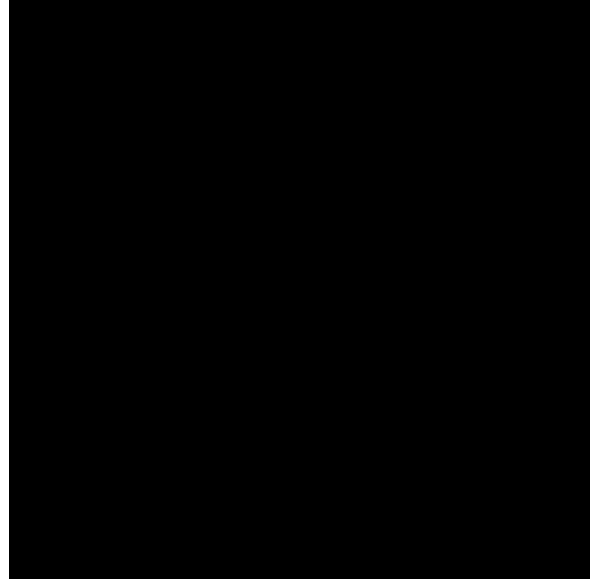


Figure 9.7: Belt B: peak frequencies for all loadpaths vs. pullforce

transition area apparent for all loadpaths except the blue one. Next to that the loadpaths intersect each other in the higher frequency region. This means that the vibration frequency of the pushpart can be equal for different loadcases, dependent on the initial pullforce and pushforce.

9.3 Belt comparison

The measurement data obtained for belt B is also obtained for the other three belts. A comparison between all four belts is made in this section. Before the results are presented it should be noted that during the frequency measurements it was experienced that for the lower ██████ belts it was more difficult to perform the measurements than for the higher ██████ belts. This can be mainly accounted for the fact that the higher ██████ belts tend to settle at lower pushforces than the lower ██████ belts, meaning that individual movement in between elements occurred less over the loadpath for these belts. As one could imagine this individual movement could seriously influence the measurement since the pushpart is hit by an impact hammer.

9.3.1 Loadpaths

In Figure 9.8 the measured loadpaths for all four belts are plotted. Although the loadpaths for the different belts start at similar initial pullforces it can be seen that depending on the ██████ a different relation between pull- and pushforce exists. Belt D deviates the most from the other three belts and for higher pullforces the deviations between all belts loadpaths increases overall. The fact that the loadpaths of the different belts do not always overlap each other exactly means that the results of the belts cannot be compared directly since loadcases between the belts do not always match.

9.3.2 Frequencies

To overcome the problem of misaligning loadpaths and to be able to compare the measurements of all four belts the frequency data is linearly interpolated between the loadpaths. For the loadcases were multiple peak frequencies exist in the FRF, the highest peak is selected. In this way the frequency variation in the area between the lowest and highest loadpath can be mapped. In Figures 9.9 to 9.12 the interpolated data is plotted in color maps.

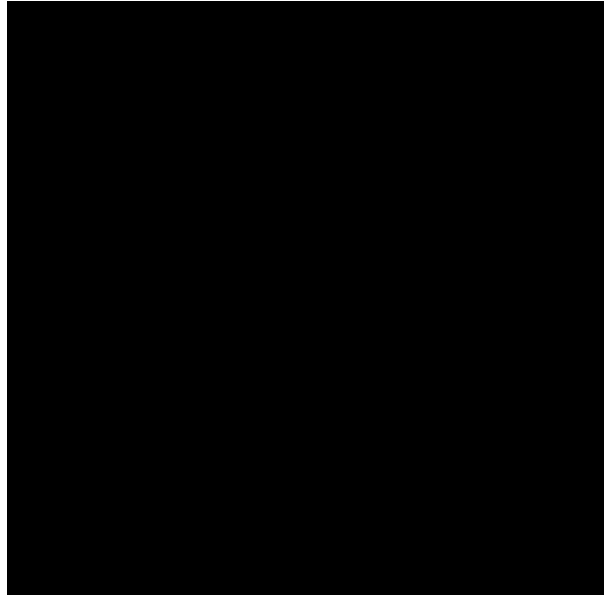


Figure 9.8: Measured loadpaths all belts

Overall it can be stated that for higher [REDACTED] belts the frequencies are higher than for lower [REDACTED] belts, both in the low and high force regions. At high pull- and pushforce the frequency for belt A and D reaches respectively [REDACTED] and well over [REDACTED]. Furthermore it can be seen that at low pushforces the frequency changes much faster for the higher [REDACTED] belts than for the lower [REDACTED] belts. Next to that the contour lines at low pushforces are almost vertical indicating that the change in pushforce changes the frequency much more significant than the pullforce. For higher forces the contour lines seem to more and more align with the loadpaths of the belts meaning that the change in frequency somehow corresponds to the relation between pull- and pushforce. For higher [REDACTED] this alignment even occurs at medium pushforces of [REDACTED] and above.

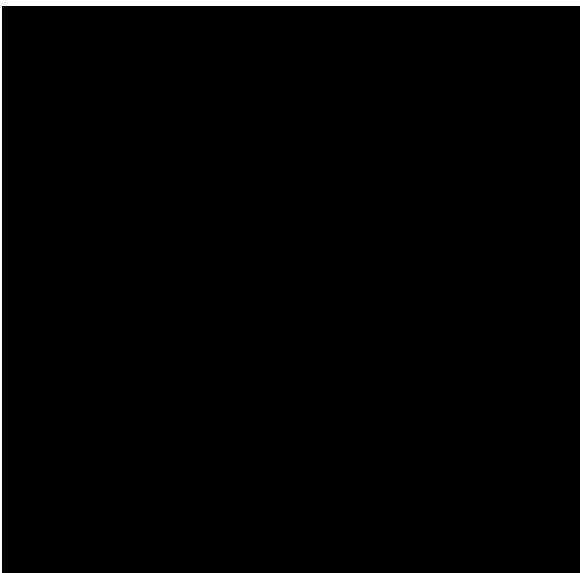


Figure 9.9: Belt A: frequency contour plot

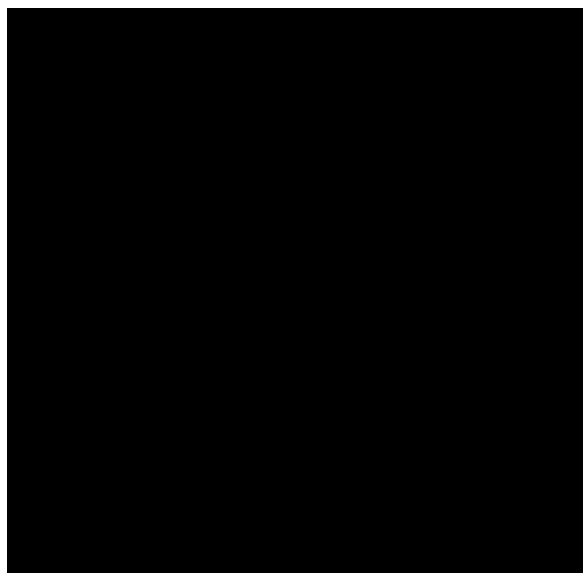


Figure 9.10: Belt B: frequency contour plot

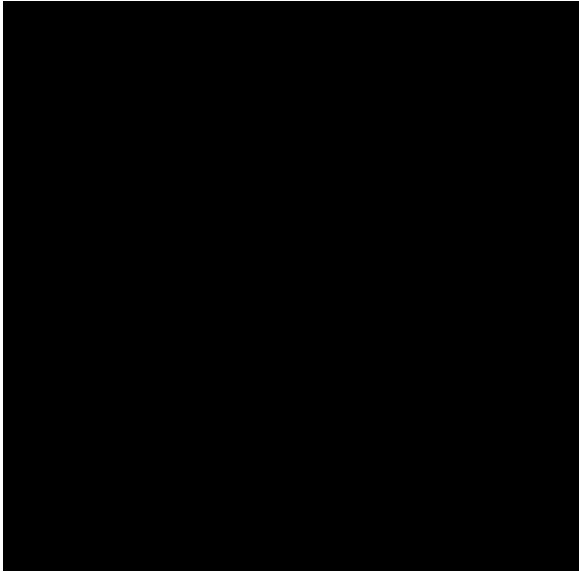


Figure 9.11: Belt C: frequency contour plot

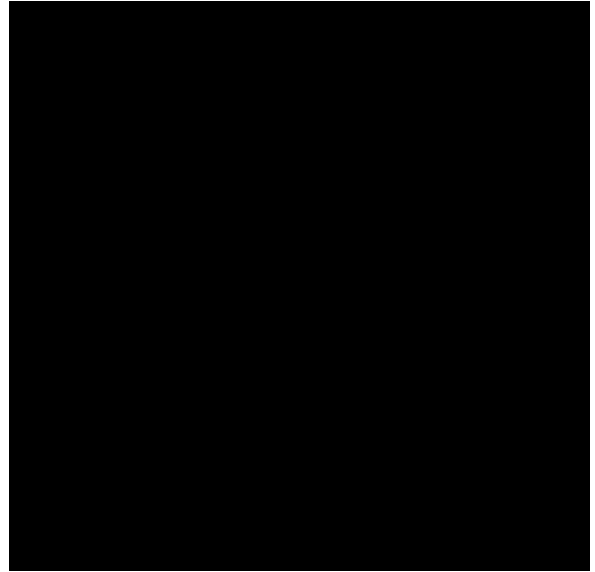


Figure 9.12: Belt D: frequency contour plot

9.3.3 Transition area

A drawback of interpolating the frequency data is that the transition areas that were identified in previous section are not visible anymore. The smaller transition area is not visible for all belts and all loadpaths but the large one is. This larger transition area is an interesting phenomena that is going to be looked at more closely.

To be able to compare the transition area between the different loadpaths and belts three transition area characteristics are defined. The first characteristic is defined as the frequency jump between the fading out and fading in frequency. The second characteristic is defined as the pushforce difference between the fading out and fading in frequency. The last characteristic is defined as the pullforce difference between the fading out and fading in frequency. For all belts and all loadpaths the first characteristic is plotted in Figure 9.13 and the second and third are plotted together in Figure 9.14.

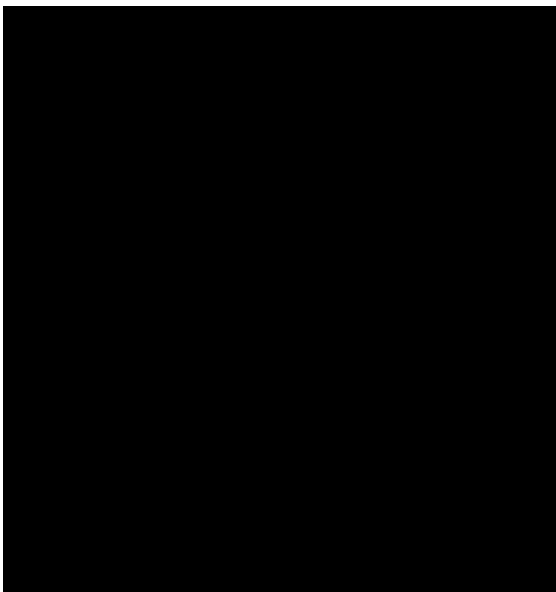


Figure 9.13: Transition area: frequency jump

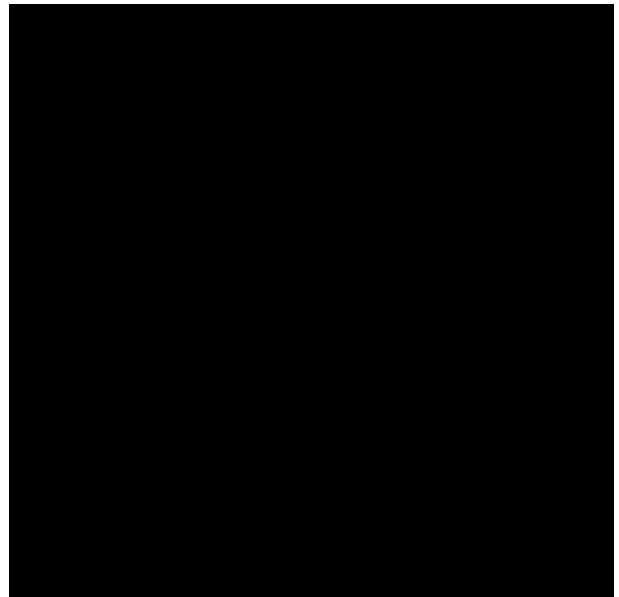


Figure 9.14: Transition area: force differences

In Figure 9.13 it can be seen that the frequency jump for belts A to C is between ██████████, where belt A is most consistent over the different loadpaths. The frequency jump for belt D shows a reasonably constant increase over the different loadpaths.

In Figure 9.14 the transition areas are indicated by rectangles where the face color of each rectangle denotes the belt and the edge color denotes the loadpath. The rectangles are placed in a pull- pushforce coordinate system at the location where the frequency transition for that particular belt and loadpath takes place. The width of the rectangle resembles the second characteristic and the height the third. By visualizing the frequency transition in this way some interesting observations can be made. Firstly, considering the location of the rectangles, it can be seen that for increasing ██████ the transition takes place at lower pull- and pushforces, in particular for the loadpaths with lowest initial pullforce. For the highest two loadpaths not only the location but also the size of the rectangles for belt B to D is much alike. Furthermore for the loadpaths with lower initial pullforce the rectangles of belt D are significantly smaller, especially the width. This means that the frequency transition for the highest ██████ belt takes place over a smaller pushforce range than the other belts.

9.4 Conclusion

From the frequency measurement results a lot of conclusions can be drawn providing new insights in the frequency response of the pushpart. From the results of belt B it can be concluded that the loadpaths over which is measured are nonlinear. The frequency change for increasing load can be divided in two parts. At low pushforce the frequency increases fast and for high pushforces the frequency increases slowly and eventually stagnates. The area in between these two parts is named the transition area. In this area the frequency makes a jump in trend. The lower trend fades out and the higher trend fades in. Furthermore at a loadpath with high initial pullforce the frequency is higher than for a loadpath with low initial pullforce, matching the theory that increasing tension in similar systems increases the frequency. However the fact that increasing pushforce also increases the frequency contradicts this theory.

Comparing all four belts in first it can be concluded that the loadpaths between belts do not match although starting at similar initial pullforces. By interpolating the frequency data the measurements for all four belts could be compared, showing that the vibration frequency overall is higher for higher ██████ belts. Next to that the increase in frequency at low pushforces is more violent for increasing ██████. From trends in corresponding color maps it can also be seen that at low pushforces the changing in frequency is mostly depending on the pushforce and for high pushforces the frequency seems dependent on a relation similar to that between pull- and pushforce.

Finally by analyzing the transition area it is shown that the frequency jump is mostly constant for belts A to C and shows an increase over the loadpaths for the highest ██████ belt. Moreover regarding the forces and force range where the transition takes place it can be seen that for increasing ██████ the transition takes place at lower pushforces and at smaller pushforce ranges. For increasing initial pullforce of the loadpath this difference becomes smaller.

Chapter 10

Pushpart modal analysis

10.1 Introduction

Next to the frequency measurements the pushpart span in the modified tool can also be subjected to a modal analysis. Using this analysis the mode shape of the pushpart can be found. Especially interesting for this analysis is the transition area. In this area two dominant frequencies appear for which a different mode shape could possibly explain what phenomena is causing this transition in frequency.

10.2 Setup

For the modal analysis a similar setup is used as for the frequency measurements. Because of the significant resemblance seen in frequency trend between belts only two belts are analyzed. Belt B is selected because belts with similar [REDACTED] are commonly produced at Bosch and belt D is chosen since this has the highest [REDACTED] and therefore the largest catsback shape, possibly influencing the mode shape. The modal analysis is performed for three loadcases; below, in and above the transition area. A possible change in mode shape as a result of the frequency transition will in this way become visible.

The modal analysis is performed using a roving hammer test. This test makes use of a fixed accelerometer or in this case the hall sensor used for the frequency measurements and a roving hammer as excitation. Using this setup the analysis is done with a MISO (multi-input, single-output) approach. This approach is mathematically similar to the SIMO (single-input, multiple-output) approach due to the principle of reciprocity which is assumed to be valid in this case. This assumption seems quiet strong for this system because of nonlinear effects occurring in the pushpart. However during the frequency measurements no out of the ordinary vibration of the pushpart was visible, compared to a vibrating string or beam. Furthermore due to limitations in the tool and test setup a roving accelerator test could not be performed ending up with this test setup.

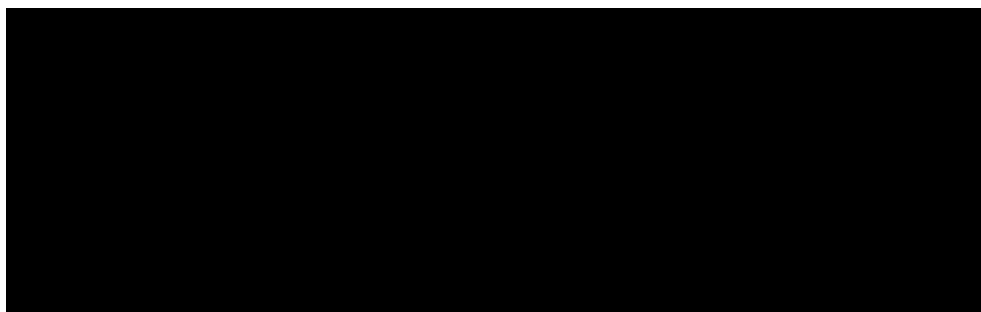


Figure 10.1: Impact hammer hit locations indicated on the pushpart

In Figure 10.1 the locations hit by the impact hammer during the analysis are indicated by black stripes.

The red stripe in the middle is also included in the locations hit with the hammer. The results of the measurement are analyzed using LMS Test.Lab. This software package contains a module to perform a modal analysis by applying the PolyMAX frequency-domain method.

10.3 Results

For each belt the loadcases for which the modal analysis is performed are chosen by trial and error to get a clear distinction between the three locations; below, in and above the transition area. The exact loadcases at which the roving hammer tests are performed can be found in Table 10.1. The frequencies measured at these loadcases are also displayed and match the trends seen in the results of the frequency measurements.

Table 10.1: Loadcases of modal analysis

Loadcase	Fpull0 [N]	Fpush [N]	Fpull [N]	Mode 1 [Hz]	Mode 2 [Hz]	ID

The different frequencies and corresponding mode shapes have all been given an unique ID to easily keep them apart. To make it even more clearer at what loadcases and frequencies the mode shapes have been analyzed a graphical overview can be seen in Figure 10.2. The dashed lines represent the global trend in frequency response but do not indicate the actual frequency measurements.

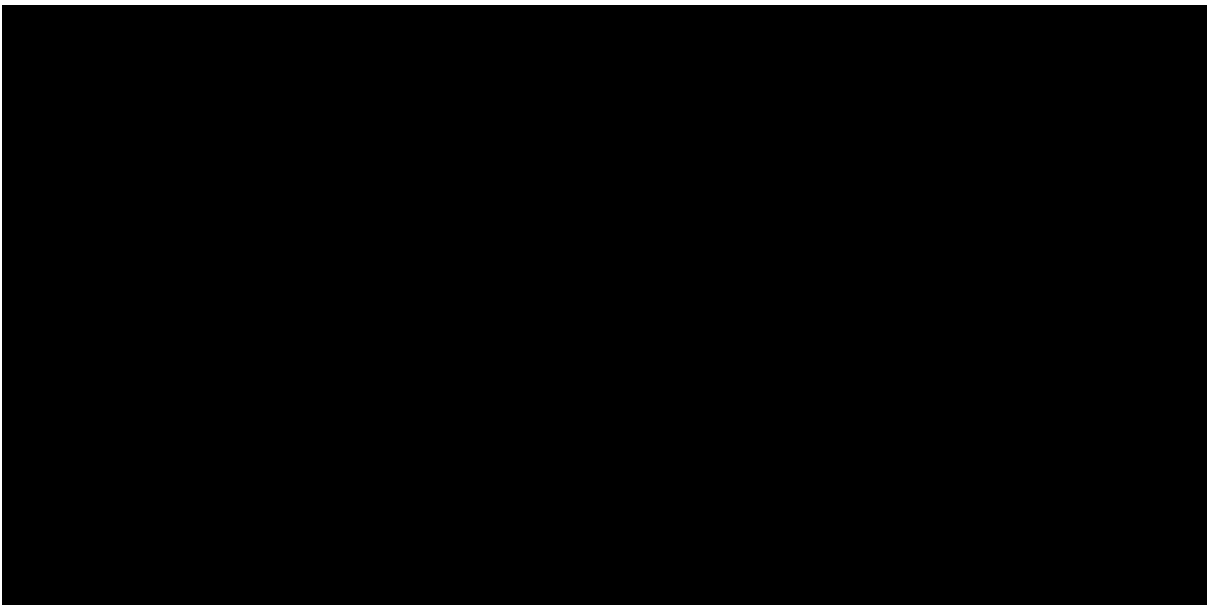


Figure 10.2: Overview of origin of the mode shapes

In Figures 10.3 and 10.4 the catsback shapes for the different loadcases are plotted. Since the pushpart is not hit with the hammer yet these shapes show the undeformed catsback shape of the pushpart. Comparing the three loadcases for each belt it can be seen that for increasing load the catsback height increases. For belt D, having a larger [REDACTED] this effect is larger.



Figure 10.3: Undeformed catsback shapes belt B

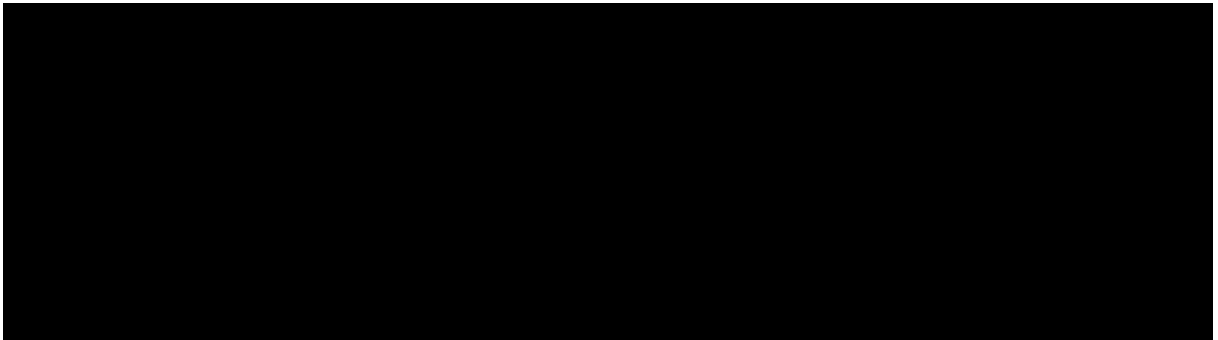


Figure 10.4: Undeformed catsback shapes belt D

It should be noted that the ends of the pushpart seem to be plotted at fixed locations. However due the effect of catsback and a fixed pushpart length these ends move towards each other for increasing catsback. Since the scale of the x- and y-axis is not equal this effect is not visible.

The mode shapes for belt B and D can be seen in Figures 10.5 and 10.6. These mode shapes are directly extracted from the LMS program. For all mode shapes it can be seen that nodes are located at the end and an antinode around the center of the pushpart meaning that the measured frequencies from previous chapter are the first mode or fundamental frequencies of the pushpart.

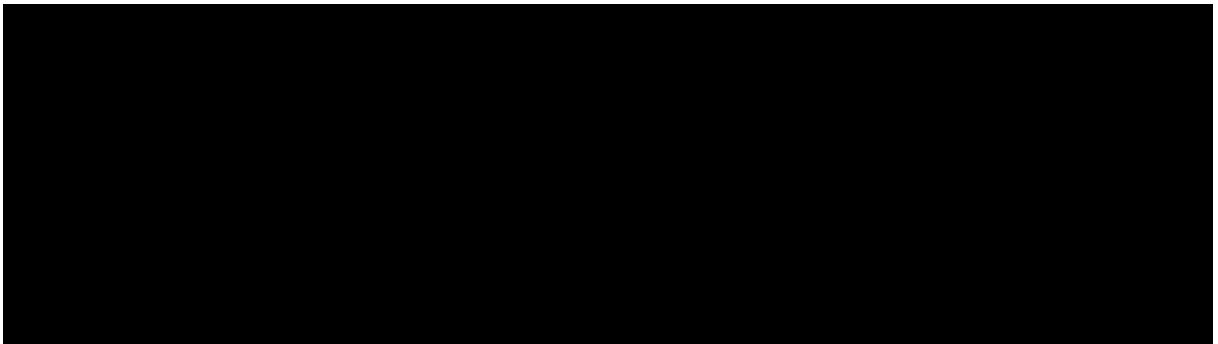


Figure 10.5: Belt B mode shapes

Regarding belt B, the mode shapes B1 and B2.1 look almost identical and have an arch-like shape. Mode shapes B2.2 and B3 also have a arch-like shape but with a flattened middle part. The mode shapes of belt D are very similar to the mode shapes of belt B. Again the mode shapes corresponding to the fading out frequency trend, D1 and D2.1 have an arch-like shape. Mode shape D3, corresponding to the highest frequency, again shows a flattened middle part. Only mode shape D2.2 is different from the similarly located mode shape B2.2.



Figure 10.6: Belt D mode shapes

Although it can be concluded that all mode shapes from both belts and for the different loadcases are much alike the subtle difference between the mode shapes can be visualized by doing a Model Assurance Criterion (MAC) analysis [27]. During this analysis the normalized dot product of the complex mode vector at each common node between two modes is calculated. If the mode are similar a value of 1 or 100% is returned. Are the mode shapes completely different a value of 0 or 0% is returned. In this way insight is given on the similarity of the different mode shapes. Typically these MAC values are presented in a MAC matrix. The MAC matrices of belt B and D are presented in Figure 10.7 and 10.8.

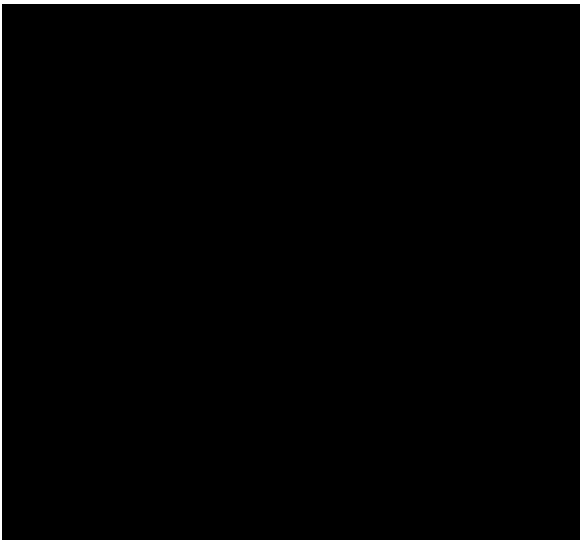


Figure 10.7: Belt B MAC matrix

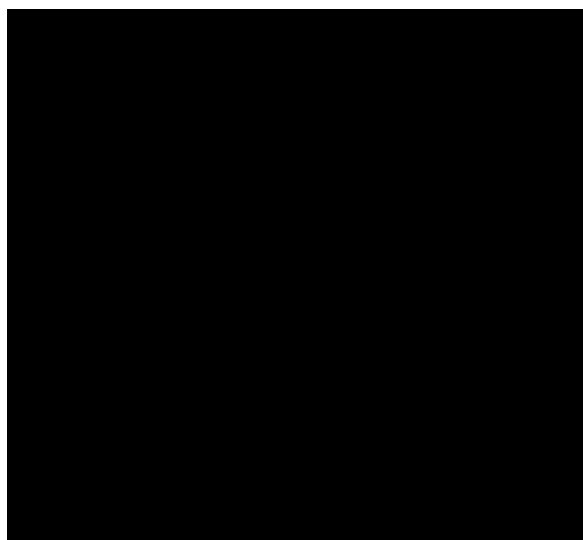


Figure 10.8: Belt D MAC matrix

From the MAC matrices for both belts it can be seen that the MAC values for all mode shape comparisons are high. Although it can be seen that for the mode shapes in the transition area the MAC value is lower. To be able to compare the MAC values even more clearly they have been plotted in a regular 2D matrix in Figures 10.9 and 10.10. In these matrices the values are formatted so the lowest value is yellow and the largest value is red. Note that the diagonal values in both matrices are red and thus 100% since each mode is compared to itself.

Although the differences are relatively small, by assigning a color to the individual values an interesting similarity between the matrices of both belts becomes visible. Comparing the mode shapes B1, B2.1 and D1, D2.1 to respectively B2.2 and D2.2, a relatively large difference in mode shape is indicated by the MAC value. This indicates that the pushpart vibration shape for the frequency trend that fades in during the frequency transition is (slightly) different from the pushpart vibration shape for the low frequency trend.



Figure 10.9: Belt B MAC matrix values



Figure 10.10: Belt D MAC matrix values

Surprisingly enough the mode shapes B3 and D3 are again very much similar to the respectively B1, B2.1 and D1, D2.1. This is also seen in the MAC values for the comparison B2.2 to B3 and D2.2 to D3, which are also relatively low.

10.4 Conclusion

The mode shape analysis of the pushpart is performed using a roving hammer test. The results from this test show that for all measured frequencies, below, in and above the transition area, the first mode or fundamental frequency is found.

Comparing the individual mode shapes of each of the belts to each other by doing a MAC analysis it can be concluded that overall the mode shapes indeed are very much alike. However if the MAC values are compared relatively to each other it can be concluded that for both belts the mode shape of the higher frequency in the transition area, located in the fading in frequency trend, is slightly different from the mode shapes corresponding to the other three measured frequencies. Not only the mode shapes of the frequencies in the lower fading out frequency trend, but also the mode shape corresponding to the highest measured frequency in the higher fading in trend. An explanation for this difference in mode shape cannot be given although it does not seem coincidental that for both belts a similar conclusion can be drawn.

Chapter 11

Pushpart modeling

11.1 Introduction

The measurement results presented in previous chapters give new insights on the frequency response of the pushpart. In this chapter an attempt is made to replicate the results by examining similarities and differences between the results from Chapters 9 and 10 and the theory behind ordinary belts. In this way it becomes clear on what level the complex mechanism behind the belt vibrations can be modeled and on what level more research is necessary.

11.2 Loopsets model

The natural frequency of the loopsets incorporated in the pushpart assembly can be calculated relatively easily, as seen previously in Chapter 4 and Section 8.8. A comparison between the measured frequencies of the pushpart and that of the loopsets can therefore also be made with low effort. This comparison will in first be made by looking at the start of the loadpaths and subsequently looking at the rest of the loadpaths.

11.2.1 Loadpath start

In the case that the pushpart is solely loaded with a pullforce in the loopsets, without a pushforce applied in between the elements, no contribution of the elements to the flexural rigidity of the beam is present. The elements are after all free to move with respect to each other and any element-element interaction forces are negligible small compared to the pullforce. By choosing these pull- and pushforces essentially the loadcase at the start of each loadpath is replicated when only an initial pullforce is applied. Ruling out the influence of the elements on the flexural rigidity the pushpart can be replicated by a tensioned beam, representing the loopsets. Note that ruling out the flexural rigidity does not mean that the elements have been removed from the pushpart. The mass of the element string must be taken into account since this also influences the natural frequency of the pushpart. The frequency can for this special case be calculated using Equation (4.2.19), using the following parameters; density $\rho = \blacksquare \text{ kg}\cdot\text{m}^{-3}$, Young's modulus $E = \blacksquare \text{ GPa}$, width $w = \blacksquare \text{ m}$, height $h = \blacksquare \text{ m}$ and mode number $n = \blacksquare$. Note that the factor 10 in the height of the loopset is introduced because of the 10 loop layers in the loopset. The length, inertia and mass per unit length of the pushpart are in this case defined as:

$$L = \#el \cdot th \tag{11.2.1}$$

$$I = 2 \cdot \frac{wh^3}{12} \tag{11.2.2}$$

$$m = 2\rho(wh) + \frac{m_{el}}{th} \tag{11.2.3}$$

where $\#el = \blacksquare$ is the number of elements, $th = \blacksquare$ m is the thickness and $m_{el} = \blacksquare$ kg the mass of each element. Note that both loopsets are substituted by a single beam resembling the loopsets packed side by side. This assumption can be made since the loopsets have similar dimensions and share the same centroidal axis. Since the ratio between length and height meets the criteria of an Euler beam this equation is in this case valid.

In Figure 11.1 the pushpart frequencies at the start of the loadpaths are plotted. The natural frequencies of the four belts at the start of the loadpaths have not been measured because this was not possible. At zero pushforce the individual elements can move slightly with respect to each other making it impossible to hit the pushpart properly during the impact hammer tests. The frequencies presented in Figure 11.1 are linearly extrapolated from the frequency measurement results.

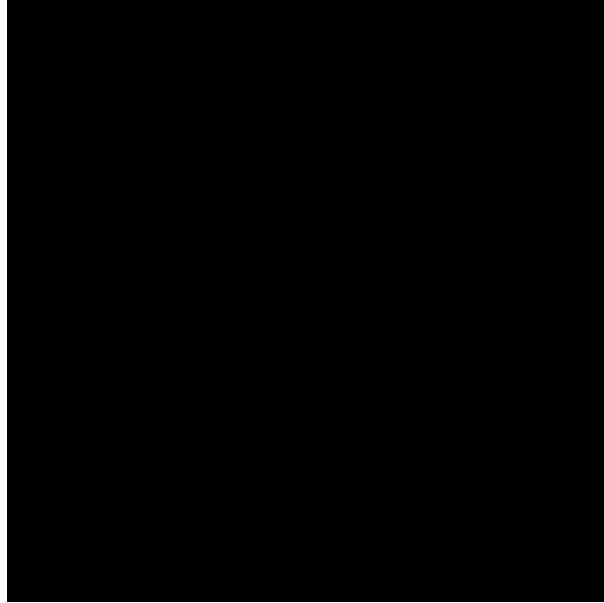


Figure 11.1: Measured and calculated natural frequencies at the start of the loadpaths

Figure 11.1 shows that the natural frequencies of the four belts are not the same although it is expected that they are. The only difference between the belts is \blacksquare and this parameter should not influence the natural frequency of the pushpart since no pushforce is applied. Because the presented frequency is derived from the other frequency measurements most likely measurement accuracy differences between the belts are the cause of the frequency differences shown as explained in Section 9.3. The calculated natural frequency of the pushpart without element string flexural rigidity overall comes closest to that of belts C and D but varies over the different loadpaths. This confirms the experience gained during testing that the measurement accuracy is not always optimal but improves for increasing \blacksquare .

11.2.2 Loadpath start to end

A similar comparison as in previous section cannot be made for the full loadpaths since the pushforce causes the elements to be pressed against each other effecting the flexural rigidity of the belt. Up to now the exact influence of the elements on the flexural rigidity is not know. However by doing a thought experiment this influence can be visualized.

Again it is assumed that the pushpart can be modeled solely by looking at the loopsets. The influence of the elements on the flexural rigidity is neglected but the increase in pullforce as a result of the relation between pull- and pushforce is not. Clearly this is a thought experiment since the situation that is sketched could not occur in reality. Making these assumptions the pushpart's natural frequency can be calculated by tensioning a beam with pullforces that match the pullforces experienced by the loopsets along the loadpaths.

In Figures 11.2 and 11.3 the measured frequencies of belt D are plotted as well as the model of the pushpart described here, from now on called the loopsets model. As can be seen in Figure 11.2 the model shows a relation expected for a tensioned beam. The loadpaths in this case overlap each other. Compared to the measurements the model does not show a similar increase in frequency for the different loadpaths. This can also be seen in Figure 11.3. The natural frequency calculated for the loopsets model only increases because of an increase in pullforce as a result of the interaction between pull- and pushforce. Clearly this effect cannot fully explain the change in frequency over the loadpaths. An additional effect between pushforce, element string and the natural frequency of the pushpart should be included in the model.

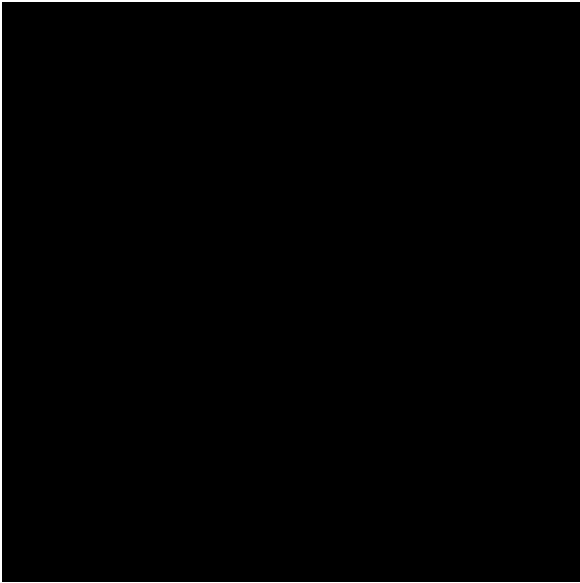


Figure 11.2: Belt D: measured natural frequency vs. loopsets model against pullforce

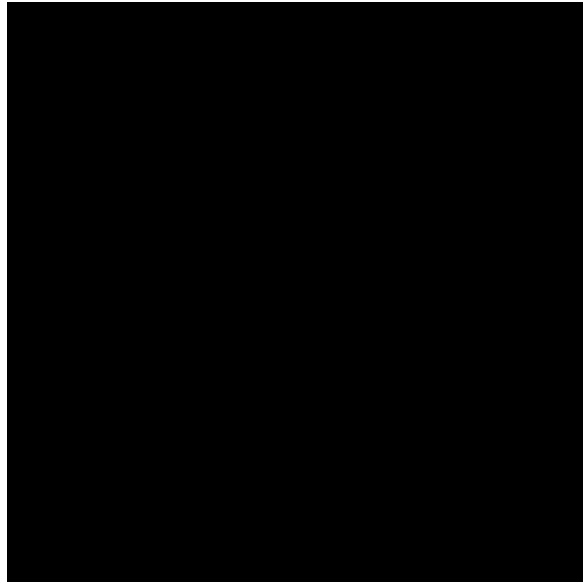


Figure 11.3: Belt D: measured natural frequency vs. loopsets model against pushforce

To visualize the difference between the measured frequencies and loopsets model the percentual difference between the two is plotted for all four belts in Figure 11.4. The percentual difference is calculated for all measured loadcases using Equation (11.2.4). Defining the difference in this way directly shows where the loopsets model falls short in describing a relation between pushpart load and frequency. In the figure each dot represents a loadcase, without making a distinction between the different loadpaths.

$$\text{Percentual difference} = \frac{\text{Measured frequency} - \text{Loopsets model frequency}}{\text{Loopsets model frequency}} \times 100\% \quad (11.2.4)$$

In Figure 11.4 it can be seen that for pushforces close to zero and for belts B to D the difference is smallest, as was expected since the model was initially designed for zero pushforce. The percentual difference is largest around a [REDACTED] pushforce and decreases to approximately 40% at very high pushforces. Overall it can be concluded that the frequencies calculated by the model are much too low compared to the measurements. This means that the flexural rigidity in the model is too low which can be explained by the fact that the flexural rigidity of the element string was ignored.

Belt A shows a significantly different trend compared to the other belts. The absolute initial difference is much larger and the trend follows a different path than the trends for the other three belts. Apparently the negative [REDACTED] has a significant influence on the frequency response of the pushpart. In fact a similar trend between the belts can be found when examining the compression stiffness of the belts. Since the loopsets model used in this section clearly is not sufficient to replicate the frequency response of the belts the compression stiffness is investigated in the next section to analyze its influence on the frequency of the pushpart.

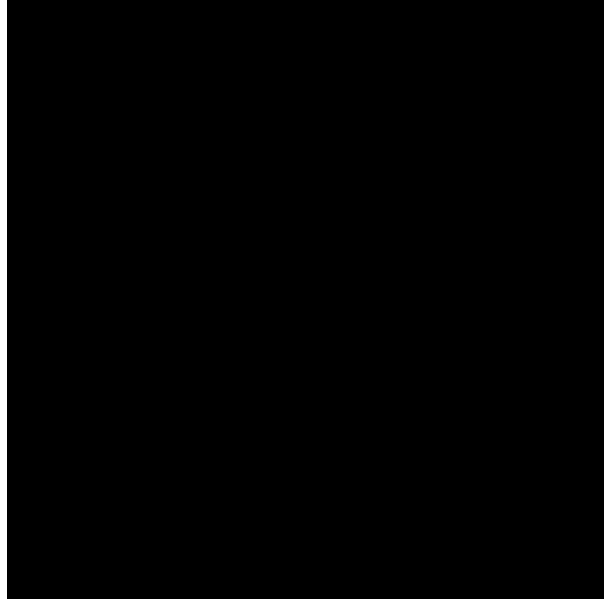


Figure 11.4: Percentual difference between measurements and loopsets model

11.3 Compression stiffness

The compression stiffness of the pushpart of the four belts can be calculated from compression curves obtained by using the compression tool, from Section 8.2, as it is intended for. In compression curves the longitudinal compression of the pushpart is displayed as function of the pushforce. It should be noted that the measured compression not only includes the compression of the elements as a result of the pushforce but also the extension of the loopsets as a result of the increasing pullforce while pushforce is increased. This means that the compression stiffness of the total pushpart assembly is found and not only the compression stiffness of the element string. The process of performing compression measurements is explained by [REDACTED].

For the frequency measurements the compression tool was modified and one of these modifications also is applied while measuring the compression curves. Both ends of the pushpart have been fixed as described in Section 8.3 because the compression and frequency measurements cannot be compared evenly if the boundary conditions of the pushpart are different.

11.3.1 Catsback compensation

Normally the compression tool is not fixed at both ends while doing compression measurements. Since it is necessary to fixate the tool for proper comparison with the frequency data the measured compression is not directly corresponding to the true compression of the pushpart. Especially for high [REDACTED] where a high catsback is present this is the case. The compression is measured by the longitudinal shift of the push blocks. Because the length of the pushpart in the tool is fixed and the push blocks cannot move up or down they shift inwards for increasing the catsback height. This additional shift is incorporated in the measured compression resulting in a measured compression that is higher than the actual compression as visualized in Figure 11.5.

While the pushpart is longitudinally compressed, the measured compression is defined as u . But because of the catsback shape that appears at the same time, the actual compression of the pushpart is v . By monitoring the catsback height h , at the center of the pushpart, during the compression measurements the measured compression can be adjusted for the growth in catsback. This is under the assumption that the catsback shape is a perfect arch with constant radius. Using a geometric relation for a circular segment explained by Weisstein [9] the actual compression v is defined as:

$$v = L - \arcsin \left(\frac{L - u}{h + \frac{(L-u)^2}{4h}} \right) \left(h + \frac{(L - u)^2}{4h} \right) \tag{11.3.1}$$

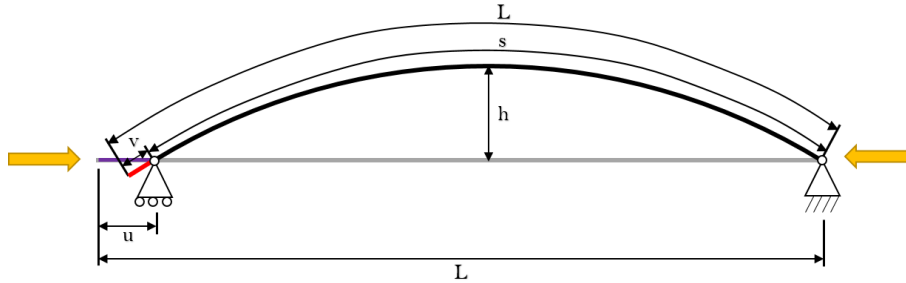


Figure 11.5: Compression measurement error

11.3.2 Compression curves

All presented compression measurement results have been compensated for catsback height according Equation (11.3.1). The outcome of the compression measurement of one of the belts is shown in Figure 11.6. The data for belt D is presented since for this belt the cleanest data could be obtained. Again this corresponds to the experiences from the frequency measurements regarding accuracy between the four belts. The data for the other belts can be found in Appendix C.1.



Figure 11.6: Belt D: compression curves

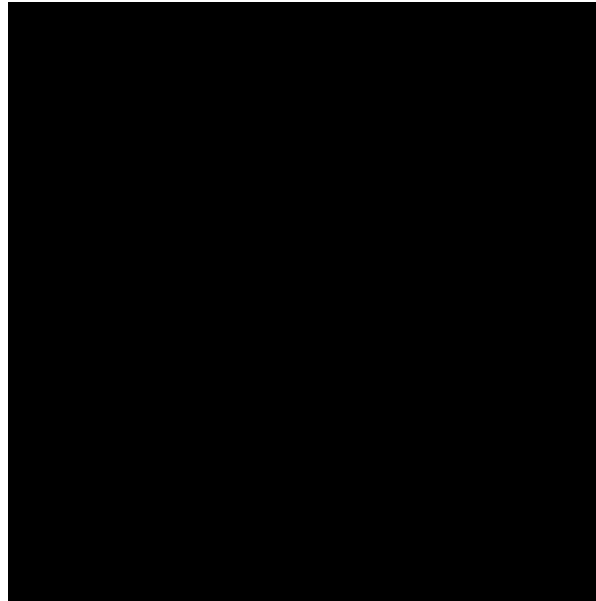


Figure 11.7: Belt D: stiffness curves

In Figure 11.6 the compression curves are shown for all loadpaths of belt D. It can be seen that for increasing pushforce the pushpart initially is compressed nonlinear but eventually a more linear relation between pushforce and compression exists. Regarding this figure it should be noted that the compression curves have been smoothed by a moving average with a window of approximately 15% of the total amount of data points for each loadpath. This is essential for smoothing the compression stiffness curves as much as possible as can be seen in the next section.

11.3.3 Stiffness curves

The compression stiffness of the pushpart is calculated from the compression data according general equation:

$$S = \frac{dF}{du} \quad (11.3.2)$$

where S is the compression stiffness in $\text{N}\cdot\text{m}^{-1}$, F is the compression force and u the compression.

The stiffness curves for belt D are presented in Figure 11.7. It can be seen clearly that numerous fluctuations in the trends have appeared. This is caused by minute fluctuations in the compression curves even after smoothening. It should be noted that filtering of the compression data reduces the amount of fluctuations in the compression stiffness curves but also the amplitude of the stiffness curves is altered, which is undesirable. For increasing pushforce initially the increase in compression stiffness is large and eventually flattens out. Note that the compression stiffness starts at zero for zero pushforce since the elements are not compressed when no pushforce is applied.

When all stiffness curves from all four belts are plotted together an interesting and familiar trend for low pushforces appears, as can be seen in Figure 11.8. The stiffness curves are presented in a scatter plot so the trend between stiffness and pushforce can be seen more clearly. For low pushforces up to a [REDACTED] the stiffness curves of all loadpaths of belts B to D follow a similar trend while belt A does not. In fact a similar difference between belt A and the other belts is seen in Figure 11.4. The fact that a similar trend is seen suggests that the relation between pushforce and compression stiffness is to some extent also visible in the frequency response of the pushpart.

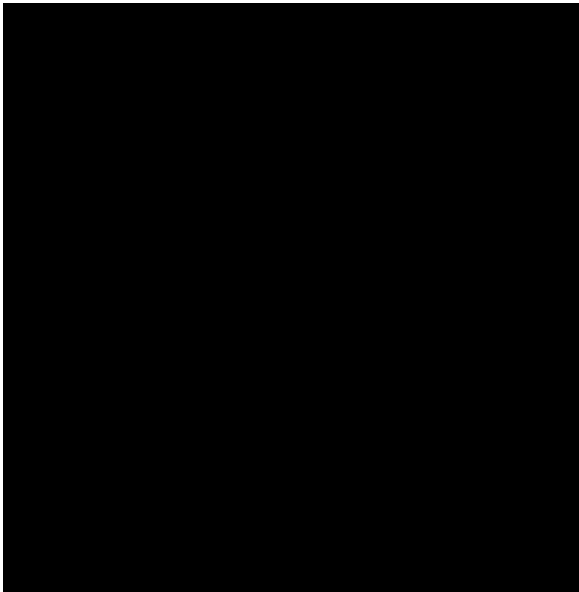


Figure 11.8: All belts: compression stiffness curves scattered

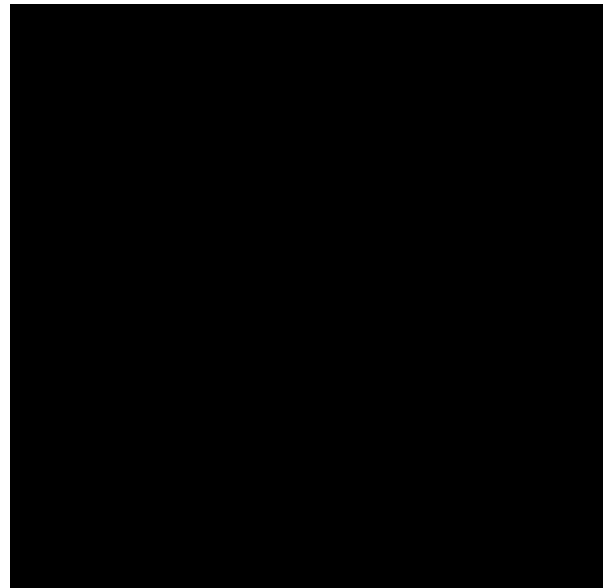
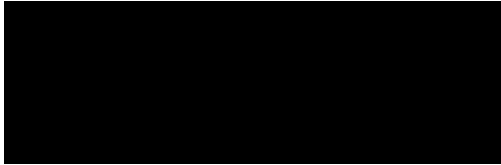


Figure 11.9: Percentual difference between measurements and pushpart model without element string flexural rigidity

11.3.4 Compression curve fitting

To overcome the minor irregularities visible in Figure 11.6, the compression curves can be fitted to known curves. These curves are used as approximation of the measured curves. [REDACTED] described a relation, Equation (11.3.3), that can be used for describing the compression curves. This relation

describes the curve in two parts, a nonlinear part and a linear part.


(11.3.3)

where . As can be seen from the conditions parameter F_0 indicates the boundary between nonlinear and linear relation.

In theory fitting the compression curves using equation (11.3.3) sounds straight forward although at Bosch multiple attempts have shown that fitting of the curves is quiet a challenge because in the measurement data a clear boundary between the nonlinear and linear part is not always visible, as is also the case for the curves from Figure 11.6. Therefore, for this investigation the smoothed data presented in Figures 11.6 and 11.7 is used and presented in scatter plots to visualize trends more clearly.

11.4 Element string implementation

The frequency measurement results have been compared to a simplified loopsets model which was created by neglecting any flexural rigidity contribution from the element string. From the compression stiffness results it can however be seen that this pushpart property also seems to play a role. The loopsets model is therefore extended to analyze the relation between the compression stiffness and frequency response of the pushpart.

11.4.1 Pushpart as beam

Assume that the pushpart can be substituted by a single beam. This beam is subjected to both a longitudinal tension and compression. Furthermore the beam's total flexural rigidity is defined as a combination of two local flexural rigidities. The general equation for the natural frequency of this beam then becomes:

$$f_n = \frac{n}{2L^2} \sqrt{\frac{n^2 \pi^2 (EI)_{tot} + (T - C)L^2}{m}} \quad (11.4.1)$$

derived from equations (4.2.19) and (4.2.20) where $(EI)_{tot}$ is the total flexural rigidity, T the tension and C the compression force. The local flexural rigidities for this beam are logically that of the loopsets and the element string. This model will be called the pushpart model. The flexural rigidity of the loopsets is constant and always apparent. The flexural rigidity of the element string is not constant and depends on at least the pushforce as was concluded from Figure 11.4. By using equation (11.4.1) the influence of the flexural rigidity of the element string can be visualized similarly to Figure 11.4.

In Figure 11.9 the percentual difference between the measured frequencies and this pushpart model are plotted for all four belts. Again the flexural rigidity of the element string is assumed zero. For low pushforce up to  the trends shown are similar to the trends from Figure 11.4. However for higher pushforces the difference compared to the measurements is even larger than for the loopset model. Although this may seem as a performance decrease actually an interesting observation can be made when comparing Figure 11.9 to 11.8. A high correlation between trends for all four belts can be seen between the two figures. This strengthens the suspicion that the compression stiffness is related to the frequency response of the pushpart.

11.4.2 Flexural rigidity

To validate if this suspicion can be justified a relation between flexural rigidity and compression stiffness needs to be found. Therefore the components of flexural rigidity; Young's modulus and cross-sectional area moment of inertia are analyzed for the pushpart.

In first the Young’s modulus is, by implementation of Hooke’s law thereby assuming linear-elastic material, defined as:

$$E = \frac{kL_0}{A} \tag{11.4.2}$$

where E is the Young’s modulus, k is the longitudinal stiffness, L_0 is the undeformed length of the object and A is the actual cross-sectional area to which force is applied. Secondly the cross-sectional area moment of inertia is defined as:

$$I = \iint_R x^2 dA \tag{11.4.3}$$

where I is the cross-sectional area moment of inertia, x is the distance to the reference axis. The double integral is taken over the cross-sectional area of the geometric shape of the material to which force is applied.

Applying both Equations (11.4.2) and (11.4.3) for the case of the pushpart the flexural rigidity of the pushpart can be described as:

$$(EI)_{tot} = \frac{SL_0}{A_{tot}} I_{tot} \tag{11.4.4}$$

where S is the compression stiffness of the entire pushpart, L_0 is the initial length of the pushpart. A_{tot} and I_{tot} are respectively the cross-sectional area of the pushpart to which force is applied and its corresponding cross-sectional area moment of inertia.

An important difference between this approach and the loopsets model is the implementation of the loopsets. For the loopsets model the loopsets Young’s modulus was defined as a constant value corresponding to the material. In case of the pushpart model the Young’s modulus of the pushpart assembly is derived from the compression data meaning that no distinction is made between loopsets and element string but the assembly is seen as a single piece of material. This in fact is also the case for the cross-sectional area moment of inertia as is explained below.

Regarding Equation (11.4.4) the compression stiffness is measured and the undeformed length of the pushpart is known. Determining the other two parameters is more difficult. As explained in Section 2.4.3 the element-element contact area is not constant. Available knowledge about the relation between pushforce, element-element contact location and area as well as shift in bending line is not sufficient to determine this contact area and thereby the cross-section area moment of inertia. However some hypothetical model cases can be defined which might occur in the pushpart for a specific range of loadcases. These hypothetical cases are visualized in Figures 11.10 to 11.16 where the contact area and bending line are indicated in respectively blue and red. The loopsets are indicated in orange.

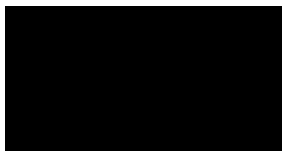


Figure 11.10: Case 1



Figure 11.11: Case 2



Figure 11.12: Case 3



Figure 11.13: Case 4



Figure 11.14: Case 5



Figure 11.15: Case 6



Figure 11.16: Case 7

For model case 1 and 2 it is assumed that all pushforce is transferred through the rocking edge and the bending line is located at respectively the centerline of the rocking edge or loopsets area. For model case

3 and 4 the pushforce is assumed to be applied fully in the head with respectively the bending line at the head or loopset area. For model cases 5 to 7 the pushforce is assumed to be distributed evenly over both head and rocking edge areas each with a differently located bending line as seen in the other cases. For these specific model cases the cross-sectional area and corresponding moment of inertia can be calculated using dimensions of respectively the loopsets, rocking edge and head: $w_l =$ [redacted] m, $h_l =$ [redacted] m, $w_r =$ [redacted] m, $h_r =$ [redacted] m, $w_h =$ [redacted] m and $h_h =$ [redacted] m. The distance of either the bending line in the loopsets, rocking edge or head with respect to the bottom of the element are respectively: $y_l =$ [redacted] m, $y_r =$ [redacted] m and $y_h =$ [redacted] m. Note that the loopsets and rocking edge cross-sectional areas are defined as rectangular shapes and the head area as a triangular shape.

Finally the total flexural rigidity of the pushpart for the specific model cases is defined by Equations (11.4.5) to (11.4.11).

$$Case\ 1 : (EI)_{tot} = \frac{SL_0}{A_l + A_r} \left(\frac{w_l h_l^3}{12} + A_l (y_l - y_r)^2 + \frac{w_r h_r^3}{12} \right) \quad (11.4.5)$$

$$Case\ 2 : (EI)_{tot} = \frac{SL_0}{A_l + A_r} \left(\frac{w_l h_l^3}{12} + \frac{w_r h_r^3}{12} + A_r (y_r - y_l)^2 \right) \quad (11.4.6)$$

$$Case\ 3 : (EI)_{tot} = \frac{SL_0}{A_l + A_h} \left(\frac{w_l h_l^3}{12} + A_l (y_l - y_h)^2 + \frac{w_h h_h^3}{36} \right) \quad (11.4.7)$$

$$Case\ 4 : (EI)_{tot} = \frac{SL_0}{A_l + A_h} \left(\frac{w_l h_l^3}{12} + \frac{w_h h_h^3}{36} + A_h (y_h - y_l)^2 \right) \quad (11.4.8)$$

$$Case\ 5 : (EI)_{tot} = \frac{SL_0}{A_{tot}} \left(\frac{w_l h_l^3}{12} + A_l (y_l - y_h)^2 + \frac{w_r h_r^3}{12} + A_r (y_r - y_h)^2 + \frac{w_h h_h^3}{36} \right) \quad (11.4.9)$$

$$Case\ 6 : (EI)_{tot} = \frac{SL_0}{A_{tot}} \left(\frac{w_l h_l^3}{12} + A_l (y_l - y_r)^2 + \frac{w_r h_r^3}{12} + \frac{w_h h_h^3}{36} + A_h (y_h - y_r)^2 \right) \quad (11.4.10)$$

$$Case\ 7 : (EI)_{tot} = \frac{SL_0}{A_{tot}} \left(\frac{w_l h_l^3}{12} + \frac{w_r h_r^3}{12} + A_r (y_r - y_l)^2 + \frac{w_h h_h^3}{36} + A_h (y_h - y_l)^2 \right) \quad (11.4.11)$$

where A_l , A_r and A_h are the cross-sectional areas of respectively the loopsets, rocking edge and head and $A_{tot} = A_l + A_r + A_h$. Note that the cross-section area moment of inertia is defined using the parallel axis theorem.

A final note should be made regarding the initial length of the pushpart. Depending on what case is selected the location of the bending line is different. Because of [redacted] the initial length of the pushpart at these different bending line locations is also different. At the head the [redacted] for all elements should be added to the initial length. In case of belt D with the highest [redacted] this length difference between model cases will be: $\#el \cdot$ [redacted] = [redacted] m, which is $<1\%$ of the total length of the pushpart. This initial length difference between cases is therefore neglected.

11.5 Model case selection

By assuming that the pushpart can be substituted by a beam having properties from both the loopsets and element string a simple model is created for calculating the natural frequency. This model requires the compression stiffness of the pushpart to be known and can be applied for several model cases as described in previous section. It is however unknown which model case is applicable for the pushpart for the different loadpaths. Using the frequency measurement data the model is evaluated for all seven model cases to see what case shows the highest correlation.

By direct application of the loadcases from the frequency measurements and corresponding compression stiffness measurements into Equation (11.4.1) the natural frequency of the pushpart is calculated for the

seven different cases. Again the percentual difference between the measurements and model outcomes are presented. In this case the difference is defined as:

$$\text{Percentual difference} = \frac{\text{Pushpart model frequency} - \text{Measured frequency}}{\text{Measured frequency}} \times 100\% \quad (11.5.1)$$

In this way the measurements are set as baseline and a possible over- or underestimation of the frequency by the pushpart model is visualized. In Figure 11.17 the difference between the model and measured frequency for all measured loadcases of belt D is plotted for all seven model cases. Similar figures for the other three belts can be found in Appendix C. From the figure it can be concluded that the difference between the model and the measurements is lowest assuming model case 6. In fact using this case the model performs significantly better than for the other six cases.

11.5.1 Above transition area

For all four belts a similar conclusion can be drawn for the loadcases located above the transition area. In Figure 11.18 for all four belts the difference between the measurements and the pushpart model with model case 6 is plotted. It can be seen that the total spread over all four belts is between -20% and 10%, where belt A performs best with a spread between -10% and 8%. The fact that model case 6 gives the best performance of the pushpart model can give an explanation for the pushforce distribution and bending line location, namely an evenly distributed pushforce over head and rocking edge and bending line located at the rocking edge for loadcases above the transition area.

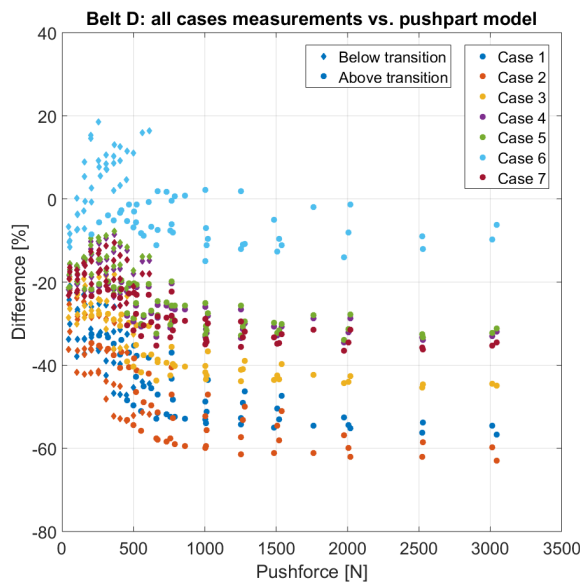


Figure 11.17: Percentual difference between measurements and pushpart model for belt D for all model cases

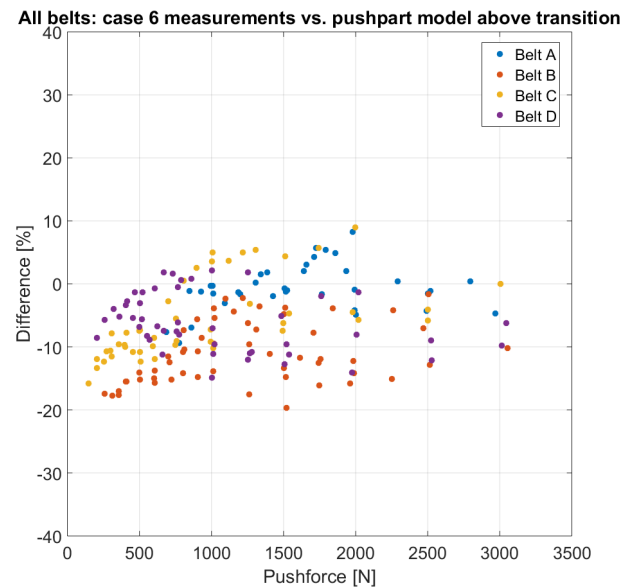


Figure 11.18: Percentual difference between measurements and pushpart model for all belts, model case 6 and loadcases above transition

11.5.2 Below transition area

For the loadcases below the transition area a single best model case cannot be pointed out as easy as for the loadcases above the transition area. In Figure 11.19 the percentual difference between measurements and pushpart model with model case 6 for loadcases below the transition is plotted for all four belts. Now the model performs worst for belt A, completely opposite to what was seen in Figure 11.18. For belt D the model performs best with a spread between -10% and 20%.

Regarding belt A the pushpart model performs much better with three other cases, namely model cases 4, 5 and 7. Note that this can be seen in Figure C.9 of Appendix C.3. Most interesting is that for these

cases belt A again performs best similarly to model case 6 above transition. Model cases 4, 5 and 7 represent cases in which the bending line does not lie at the rocking edge, but higher at the loopsets or head.

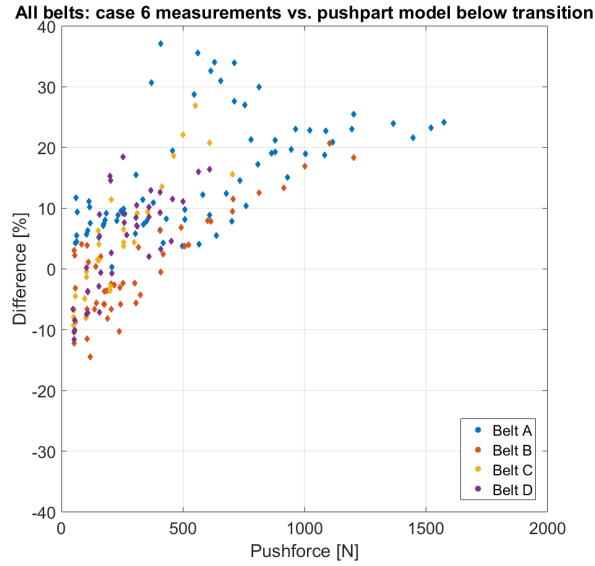


Figure 11.19: Percentual difference between measurements and pushpart model for all belts, model case 6 for loadcases below transition

In Figures 11.20 to 11.23 the percentual difference between measurements and pushpart model for four combinations of model cases is plotted. In all figures model case 6 is selected for loadcases above the transition since this is the best case for this area as seen earlier. The model case for the loadcases below the transition area are varied between case 4 and 7.

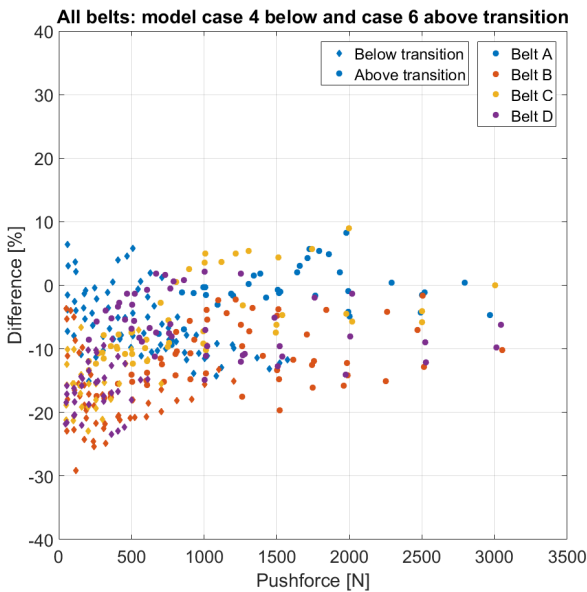


Figure 11.20: Percentual difference between measurements and pushpart model for all belts, model case 4 below transition and model case 6 above transition

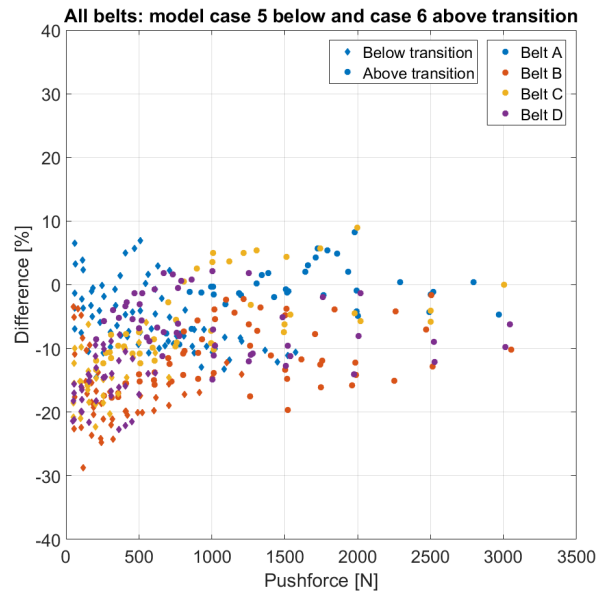


Figure 11.21: Percentual difference between measurements and pushpart model for all belts, model case 5 below transition and model case 6 above transition

In the figures it can be seen that for the low pushforce range the model with model cases 4,5 and 7 are indeed performing relatively similar compared to the model with case 6. The best performing model case is case 5 with a spread between -24% and 9%.

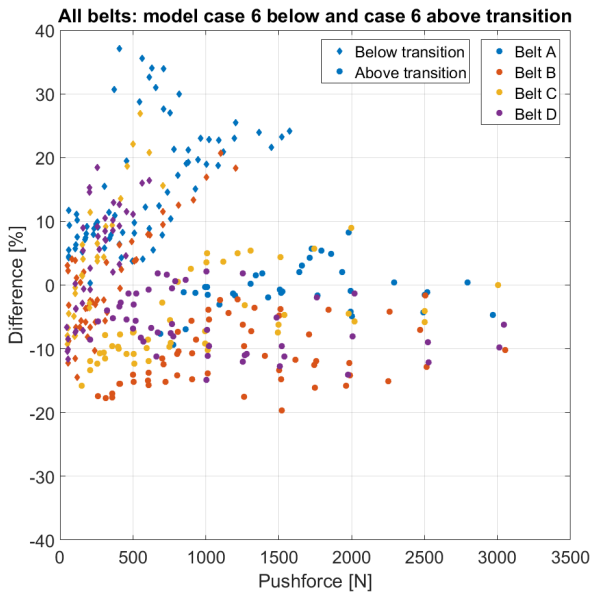


Figure 11.22: Percentual difference between measurements and pushpart model for all belts, model case 6 below transition and model case 6 above transition

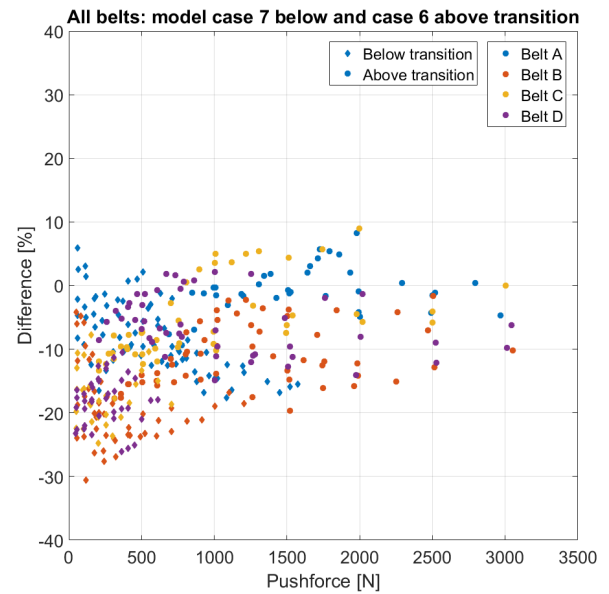


Figure 11.23: Percentual difference between measurements and pushpart model for all belts, model case 7 below transition and model case 6 above transition

By selecting the best model case for the pushpart model for both the loadcases below and above the transition area an important conclusion can be drawn which can give an explanation for the frequency jump visible in the frequency measurements. The best model case for below and above transition are respectively cases 5 and 6. In both cases it is assumed that the pushforce is evenly distributed over the head and rocking edge surfaces but the location of the bending line is shifted from head to rocking edge. This effect is directly resulting in a change in flexural rigidity in the pushpart, resulting in a jump in natural frequency occurring gradually in the transition area.

11.6 Conclusion

In this chapter an attempt is made to put together a model that can calculate the natural frequency of the pushpart. This is done by comparing outcomes of frequency measurements with a model normally used for calculating the natural frequency of tensioned beams. By only incorporating the loopsets flexural rigidity in the model, called the loopsets model, it is found that only at zero pushforce a reasonably accurate prediction of the frequency can be given. Due to the lack of pushforce the element-element contact can be ignored also ruling out any flexural rigidity contribution from this interaction. For increasing pushforce the frequencies calculated by the loopsets model however are much too low. After all the flexural rigidity of the element string is ignored resulting in a highly underestimated flexural rigidity of the pushpart.

A clear coherence in trend is found between the percentual difference between measurements and loopsets model and compression stiffness results of the four belts. Based on the suspicion that the flexural rigidity of the pushpart is influenced by its compression stiffness a direct relation between the two is found. Using this relation a pushpart model is created, based on the theory of a tensioned or compressed beam, in which the flexural rigidity of the pushpart assembly is formulated as a combination of the flexural rigidity of the loopsets and element string.

The pushpart model requires the initial length and compression stiffness of the pushpart to be known. As well as the location and size of the element-element contact area and corresponding pushpart bending line. The last two are however not known due to the lack of research done on the pushpart. Because of that several model cases have been composed each giving a plausible configuration of contact area size, location and bending line location in the pushpart.

Comparing the pushpart model, with all model cases, with the frequency measurement results it is found that at pushforces above the transition area the pushpart model with the model case stating that the pushforce is evenly distributed over the head and rocking edge and the bending line is located at the rocking edge performs best. For this pushforce range the accuracy of this model is between -20% and 10% compared to the frequency measurements.

For pushforces below the transition area the different model cases give a less clear result. Three model cases show virtually similar model performance. The main difference with the model case best suited above the transition area is the location of the bending line. It can be concluded that for pushforces below the transition area the bending line is shifted upwards to either the loopsets or head, depending on the pushforce distribution in between elements. The absolute best performing model case for pushforces below transition, with an accuracy of -24% and 9% compared to the frequency measurements, states that the bending line is located at the head and that the pushforce is evenly distributed over the head and rocking edge areas.

By defining the model cases for the pushpart model an explanation can be given for the jump in frequency in the transition area. Apparently the bending line over which the pushpart bends shifts, most likely in combination with a change in pushforce distribution in the element-element contact area. In the transition area, for increasing pushforce, the bending line shifts downwards.

A final remark should be made regarding the relatively large spread in model accuracy. Inaccuracies in the stiffness results caused a large spread in the pushpart model outcomes. Together with inaccuracies in the frequency measurement results, for the percentual difference between the model and measured frequencies also a large spread is seen. Despite this large spread, trends between the model and measurement outcomes show significant coherence to draw the conclusions listed here.

Chapter 12

Conclusion

The research done and described in this master thesis provides new insights in the frequency response of the pushpart of a metal pushbelt CVT. From the frequency measurements, the modal analysis and the formulated pushpart model conclusions can be drawn that help understand how the vibration of the pushpart is changed for changing operating conditions of the CVT. In first all conclusions found in this research are summarized; from the frequency measurement results, the pushpart modal analysis and the pushpart model. Secondly, since numerous conclusions can be drawn from the research, an overview of the investigation process described in Chapters 7 to 11 is made. In this overview a specific conclusion can easily be traced back to the corresponding part of the research. Finally reference is made to the three topics formulated during the literature study performed in preparation for this thesis.

12.1 Frequency measurements

By doing frequency measurements the frequency response of the pushpart for changing loadcases has been found for four belts with varying ██████. The conclusions drawn from the frequency response of each belt separately are:

1. The loadpaths of a pushpart are nonlinear e.q. the relation between pull- and pushforce is nonlinear.
2. For increasing pushforce the natural frequency of the pushpart increases.
3. For increasing pullforce the natural frequency of the pushpart increases.
4. The frequency response for increasing load can be divided in three parts; at low pushforce, at transition and at high pushforce. With specific conclusions for each part:
 - a. At low and high pushforce the pushpart typically only has one resonance frequency.
 - b. At transition the pushpart typically has more than one resonance frequency.
 - c. At low pushforce, for increasing load, the natural frequency of the pushpart increases fast.
 - d. At transition the natural frequency of the pushpart gradually jumps from a low to a high frequency. The low frequency fades out and the high frequency fades in.
 - e. At high pushforce, for increasing load, the natural frequency of the pushpart increases slowly and eventually stagnates.
5. The transition area, where the frequency jump takes place, can be characterized by three characteristics:
 - a. The frequency jump between the fading out and fading in frequency.
 - b. The pushforce difference between the end of the fading out and start of the fading in frequency trends.

- c. The pullforce difference between the end of the fading out and start of the fading in frequency trends.

The conclusions drawn from comparison of the measurement results of the four different belts are:

6. The loadpaths of the four different belts are not equal e.q. the relation between pull- and pushforce varies depending on [REDACTED].
7. The natural frequency of the pushpart, at similar loadcases, is higher for higher [REDACTED] belts.
8. At low pushforce, the increase in frequency is more violent for increasing [REDACTED].
9. At low pushforce, the frequency response of the pushpart is mostly depending on the pushforce.
10. At high pushforce, the frequency response of the pushpart is mostly depending on a relation similar to that between pull- and pushforce.
11. Based on the three characteristics found for the transition area:
 - a. For [REDACTED] the frequency jump is relatively constant for different loadpaths.
 - b. For [REDACTED] the frequency jump increases for loadpaths with increasing initial pullforce.
 - c. For increasing [REDACTED] the transition takes place at lower pushforces and at smaller pushforce ranges. For increasing initial pullforce of the loadpath this difference becomes smaller.

12.2 Pushpart modal analysis

Next to the frequency measurements the modal analysis of the pushpart of two of the four belts, with [REDACTED], gives the following conclusions:

12. For all measured frequencies, from previous section, the first mode or fundamental frequency is found.
13. It can be concluded that all captured mode shapes for each belt are largely similar.
14. The mode shapes of the measured frequencies in the lower fading out frequency trend are arch-like over the length of the pushpart.
15. The mode shapes of the measured frequencies in the fading in frequency trend are arch-like over the length of the pushpart but generally show a flattened part in the middle.
16. Comparing all mode shapes per belt relatively to each other, it can be concluded that the mode shape corresponding to the high frequency in the transition area differs most from the mode shapes corresponding to the frequencies outside the transition area and the lower frequency in the transition area.

12.3 Pushpart model

The pushpart model is composed by applying the existing theory of a loaded beam, also used for ordinary belt drives. This model is compared to the frequency measurement results to see where the model succeeds or fails to predict the correct natural frequency of the pushpart. By then implementation of characteristic pushbelt properties into this model, the pushpart model is fine tuned to draw the conclusions listed below:

17. At zero pushforce the flexural rigidity contribution of the element string is negligibly small since no significant element-element contact is apparent. The pushpart's flexural rigidity originates from the flexural rigidity of the loopsets solely.

18. For pushforces larger than zero the flexural rigidity of either the loopsets or element string cannot be ignored since both have a significant influence on the frequency response of the pushpart.
19. The pushpart's flexural rigidity is not constant and directly related to its longitudinal compression stiffness, based on Hooke's law, as:

$$(EI)_{tot} = \frac{SL_0}{A_{tot}} I_{tot} \quad (12.3.1)$$

where S is the longitudinal compression stiffness, L_0 is the initial length of the pushpart and A_{tot} and I_{tot} are respectively the cross-sectional area of the pushpart to which force is applied and its corresponding cross-sectional area moment of inertia.

20. The pushpart's natural frequency can be calculated using Equation (12.3.2), which is based on theory for calculating the natural frequency of a tensioned or compressed simply supported beam.

$$f_n = \frac{n}{2L^2} \sqrt{\frac{n^2\pi^2(EI)_{tot} + (T - C)L^2}{m}} \quad (12.3.2)$$

where $n = 1$ for the first mode frequency, L is the length of the pushpart, $(EI)_{tot}$ is the flexural rigidity of the pushpart, T is the tension in the loopsets, C is the compression force in the element string and m is the mass per unit length of the pushpart.

21. The frequency jump at the transition area is a direct result of a changing pushpart bending line and pushforce distribution in between elements, changing A_{tot} and I_{tot} in Equation (12.3.1).

12.4 Research overview

In Figure 12.1 a schematic overview is given of the research done in this master thesis. The different stages of the research are highlighted; the literature study, the frequency measurements, the modal analysis, the loopsets model and pushpart model. The most relevant figures from the thesis are displayed. The equation and figure numbers correspond to the numbers in the report. The specific conclusion to which each figure relates is also indicated. Note that this figure can also be found in Appendix D in a larger scale.

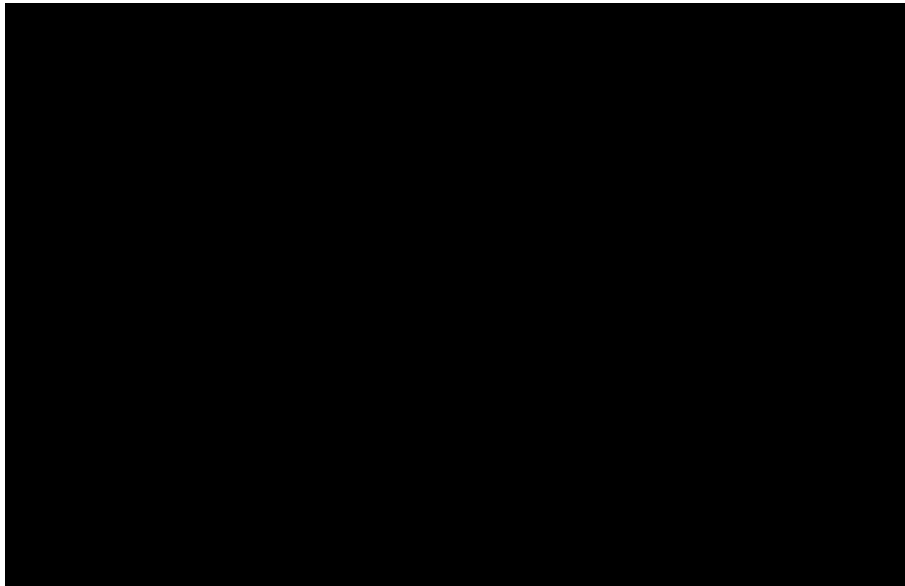


Figure 12.1: Research overview

12.5 Research topics

From the literature study it was concluded that more research on three topics was necessary to achieve the ultimate goal described in the introduction. With the new findings from this research a conclusion for these topics is given. The three topics are:

- The resemblance of the natural frequency of the pushbelt compared to that of an ordinary belt.
- The influence of belt parameters and external factors on the pushbelt's flexural rigidity.
- The influence of the pushforce distribution on the natural frequency of the pushbelt.

Regarding the first topic it can be concluded that the relation for the natural frequency of the pushbelt's pushpart is based on the same theory as that of ordinary belt drives. They share the same equation only a specific component in this equation is defined differently. The relation between length, mass, applied force and the natural frequency is similar. However for an ordinary belt the flexural rigidity is assumed constant and for the pushbelt this is not the case.

Secondly, concluded from this research, the flexural rigidity of the pushbelt depends on the longitudinal compression stiffness, pull- and pushforce in the belt and ██████. Any possible external factors that could influence the flexural rigidity have not been investigated in this research.

The pushforce distribution, from the third topic, directly influences the flexural rigidity of the pushpart and thereby the natural frequency. Although a detailed analysis of this distribution has not been performed it can be concluded from the pushpart model that a change in distribution, thereby changing the pushpart's bending line, is the cause of the frequency jump in the transition area.

Chapter 13

Discussion

At the beginning of this research a specific research scope was defined, based on the literature study outcomes and limited by the measurement tool used for this investigation. Now that the measurements are performed, conclusions are drawn based on their outcomes and a pushpart model is created, the entire research is evaluated.

13.1 Research scope and measurement setup

In first both the research scope and measurement setup are evaluated since the measurement setup partly influenced the scope of this research. From the literature study it was concluded that the natural frequency of the pushpart is highly likely influenced by several pushpart parameters. The influence of some parameters (velocity, length and mass) could not be investigated because of limitations in the measurement tool. For future research a different tool, for which it is possible to also include these parameters, is desirable.

An important choice made in the research scope is the separation of the pushpart from the entire pushbelt and assuming that it can be simply supported. This choice was made based on the research found for ordinary belt drives and the Catsback model used at Bosch that assumes a similar approach to be valid. However during the research feedback on the chosen approach and the intermediate outcomes of the frequency measurements suggested that investigating the pushpart with different boundary conditions could also add significant value to this research topic since these outcomes are not known.

Regarding the tool itself it can be stated that the tool used for the measurements was not the ideal option. But it turned out to be the only option within the available time frame. Nevertheless the tool is not designed for the kind of frequency measurements performed in this investigation. By making some well-founded modifications in the end a tool was created that could do the job although it turned out that the accuracy of the measurements is most likely influenced by the defects in the tool.

13.2 Frequency measurements

Overall the results of the frequency measurements clearly show trends in the frequency response of the pushpart. A lot of time has been invested in doing the frequency measurements since initially the outcomes of the measurements were mistrusted. The phenomena, like the transition area, visible in the data, were not expected and measurements for all belts have been performed multiple times to ensure that the measurements were performed correctly. Nevertheless achieving a sufficient measurement accuracy with the modified tool was a challenge as is also visible in some of the figures presented in Chapter 9.

The conclusions that have been drawn based on the outcomes of the frequency measurements are of high value for understanding the effect of ██████ on the frequency response of the pushpart. Within Bosch it is commonly known that a belt with negative ██████ overall has a poor performance and can be unpredictable. This is directly seen when comparing the transition areas of the four belts. Belt A with the negative ██████ generally has a significantly larger transition area than the other three belts.

Meaning that the highly nonlinear, thereby less predictable, part of the frequency response is stretched out over a larger force range, which is undesirable. Having a relative high ██████ belt, the higher fading out frequency trend appears for a large force range. This trend is much more linear and thereby better predictable than the lower frequency trend. Distinction between the highly nonlinear and more linear part of the frequency response becomes even more obvious from designing the pushpart model.

13.3 Modal Analysis

The modal analysis performed in the research is done using a roving hammer test. This type of test can typically only be performed for linear systems since the principle of reciprocity is applied assuming a symmetrical stiffness matrix. For the pushpart, a nonlinear system, it is therefore debatable if this method can be used to do a mode shape analysis. However the mode shape analysis was performed for specific loadcases. During the analysis only a relatively small force is applied by the hammer. Therefore nonlinear effects that occur for longitudinal load changes are assumed to not occur during the analyses, making it valid to use the roving hammer approach.

The outcomes of the modal analyses of both belts showed that a subtle change in mode shape takes place during the transition area. An explanation for this change in mode shape cannot be given based on the outcomes of this thesis. More research is needed to get a better understanding of the change that is occurring in mode shape while moving through the transition area.

13.4 Pushpart Model

The pushpart model was formulated by comparing the frequency measurement results with the already available knowledge about the vibration of loaded beams. While doing the frequency and mode shape measurements it was experienced that, especially for large loads, the pushpart overall acted similarly to a loaded beam. The pushpart becomes as stiff as a steel bar and clings when hit by an impact hammer. Together with the relation for the natural frequency of the pushpart found in the Catsback model [40], this experience was sufficiently convincing to investigate the resemblance of the theory behind the natural frequency of ordinary belt drives with the outcomes of the frequency measurements of the pushpart.

Although the pushpart model leads to several interesting conclusions the accuracy of the model, while comparing to the frequency measurement results, might not be truly convincing. The main reason for this is the fact that the quality of the stiffness measurements is quite poor. Due to the way the compression of the pushpart is measured multiple fluctuations are visible in the stiffness curves. By representing the calculated frequencies in scatter plots, trends over the entire pushforce range could be distinguished from the individual fluctuations over the loadpaths. If the accuracy of both the frequency measurements and compression measurements is improved it is expected that even more convincing proof is generated that shows that the pushpart model can be used to make a quick and relatively accurate estimation of the frequency of the pushpart.

The conclusion drawn regarding the shift of the bending line and change in pushforce distribution, based on the case evaluation, is valid since it turned out that the model does not work by using a single model case. Next to that signs for this effect are also found in the results of the modal analysis although a solid conclusion could not be drawn. Nevertheless this research does not give a conclusive result on how exactly the pushforce distribution and bending line location are changing in the transition area. It is expected that they gradually change locally in the transition area for changing pushpart load.

Chapter 14

Recommendation

The research presented in this thesis gives multiple new insights in the frequency response of the pushpart of a metal pushbelt CVT. As discussed in previous chapter the pushpart model accuracy is not sufficient to exactly pinpoint what is happening during the transition area. Follow-up research could help in improving the pushpart model for several reasons.

In first the model requires the longitudinal stiffness of the pushpart to be known. Future research could focus on improving the compression measurements to avoid numerous fluctuations in the data negatively influencing the stiffness data. The idea of fitting measured stiffness curves, using a power law, could be looked into more extensively to eventually be able to predict or calculate such curves just by knowing the belt parameters. If it is possible to generate stiffness curves for prototype belts without doing measurements, frequency estimations can be made before a prototype belt is physically made.

Secondly it is recommended to repeat frequency measurements for other types of belts or with different ██████. The more data is available the better trends found for the frequency response or by formulating the pushpart model can be visualized. In this way the accuracy of validating the pushpart model could in theory be improved. This could eventually help in determining the effect behind the pushforce distribution and bending line shift in the pushpart.

In third place it can be beneficial to test the pushpart model for different boundary conditions of the pushpart. Since the pushpart model is based on the straight forward beam theory, replacing the main frequency equation for application of a pushpart with different boundary conditions is relatively easy. Bokaian [5] described how to find the natural frequency of tensioned or compressed beams not only for a simply supported beam but also for amongst others clamped-clamped or pinned-clamped beams. Next to that if it becomes possible to measure the natural frequency of the pushpart under longitudinal velocity, using the theory summarized in the literature study, the pushpart model can also be adapted to include the velocity effect.

The three recommended follow-up research directions that could be looked into all require for new frequency or compression measurements. During this research it was concluded that the tool used for these measurements is far from ideal. Therefore it is highly recommended to invest in designing and building a tool that can be used for proper frequency or compression measurements. Only if such tool is created the accuracy of the frequency measurements can be improved and the fluctuations in the stiffness curves be reduced. Some requirements for this new tool are listed below:

- The pushpart must be span with different boundary conditions; pinned and/or clamped.
- It must be able to apply and measure pull- and pushforce in longitudinal direction.
- The length of the pushpart must be adjustable.
- It must be able to apply pushforce on the end-elements at either the head or rocking edge or a combination of both.
- The tool should at least be equipped with similar sensors as the compression tool.

Appendix A

Frequency measurement tool

A.1 Modified Tool and components

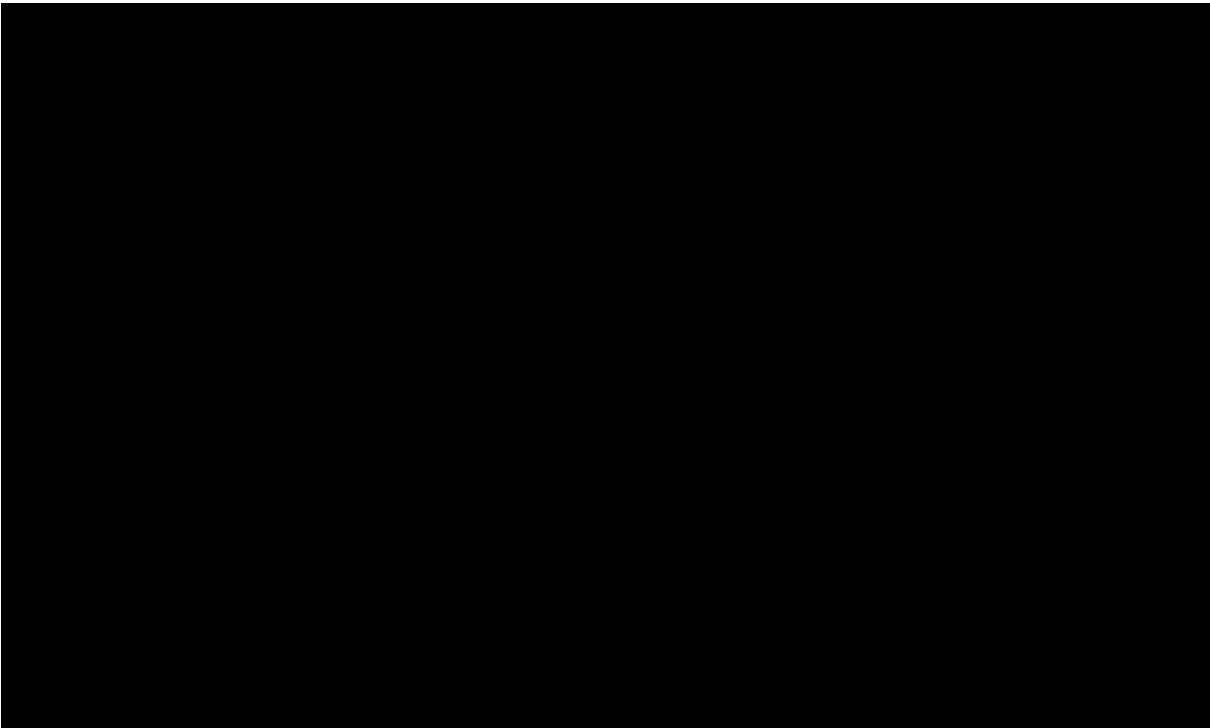


Figure A.1: Pushpart assembly in the tool

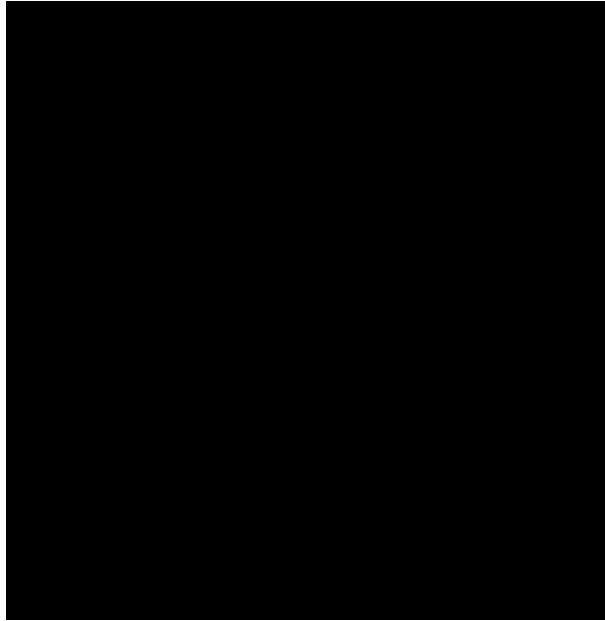


Figure A.2: Fixation of the support block



Figure A.3: Pushpart assembly

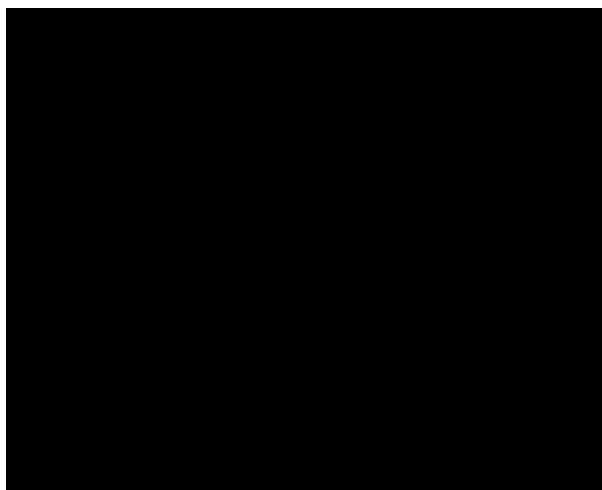


Figure A.4: CVT belt with elements removed for pushpart assembly

A.2 Tool validation

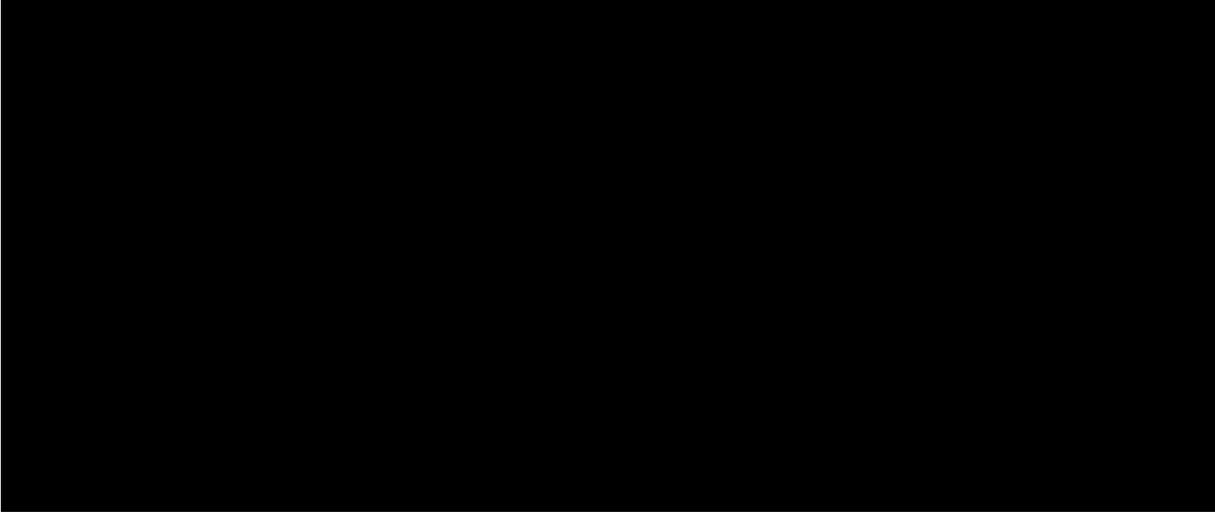


Figure A.5: Loopset validation measurement: tool setup



Figure A.6: Loopset validation measurement: measurement setup

Appendix B

Frequency measurements

B.1 Loadpaths



Figure B.1: Belt A: measured loadpaths



Figure B.2: Belt B: measured loadpaths

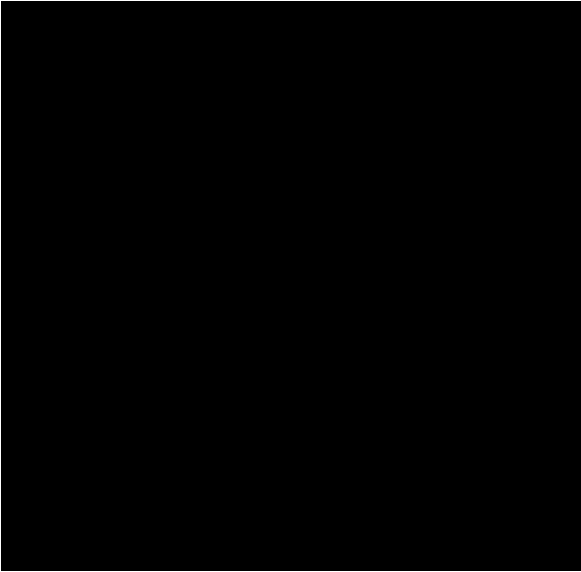


Figure B.3: Belt C: measured loadpaths

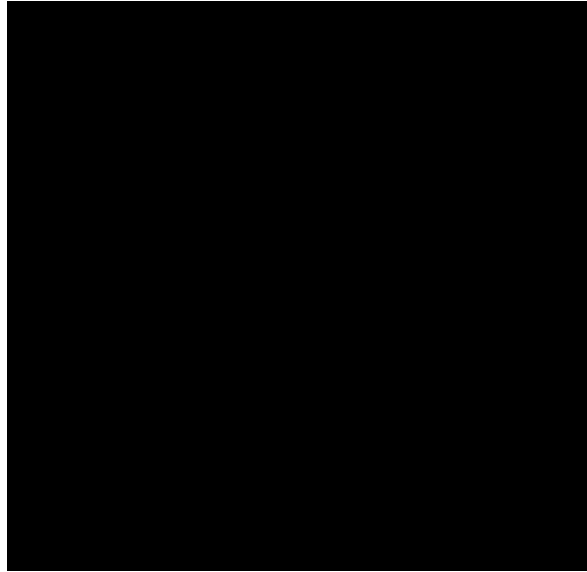


Figure B.4: Belt D: measured loadpaths

B.2 Resonance frequencies

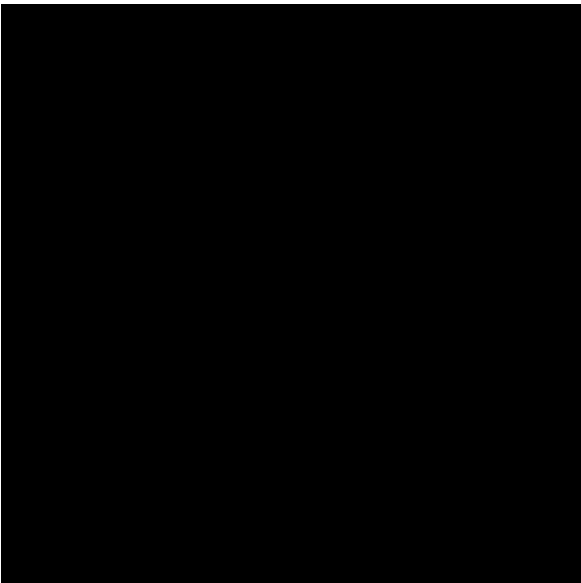


Figure B.5: Belt A: resonance frequencies for all loadpaths vs. pushforce

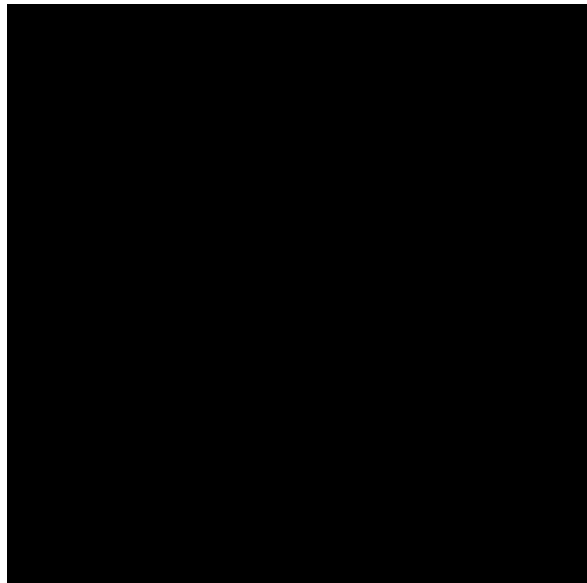


Figure B.6: Belt A: resonance frequencies for all loadpaths vs. pullforce

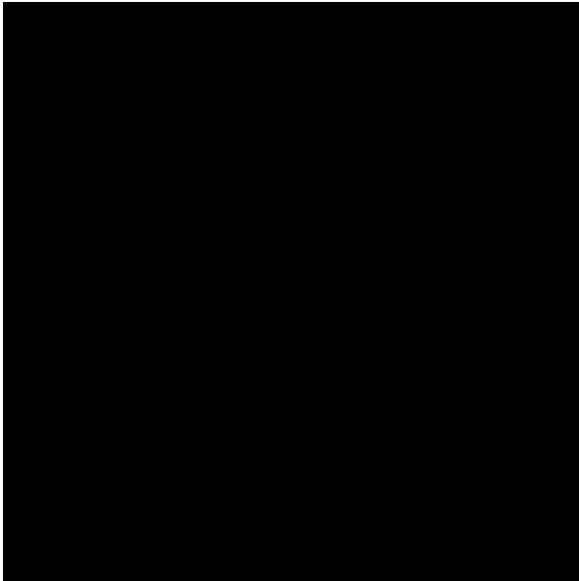


Figure B.7: Belt B: resonance frequencies for all loadpaths vs. pushforce

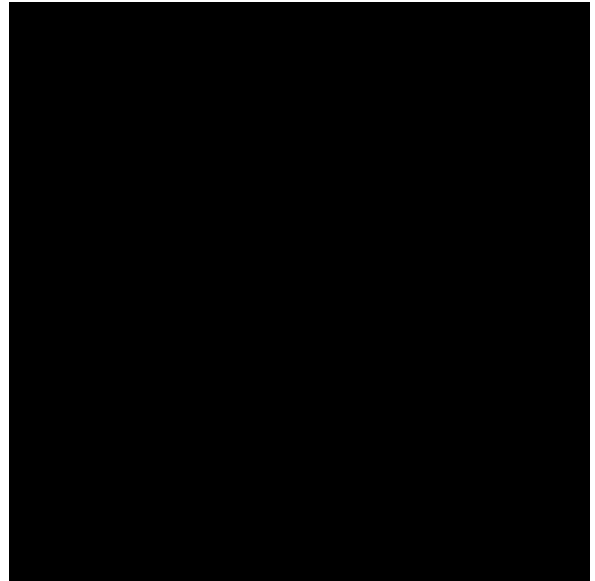


Figure B.8: Belt B: resonance frequencies for all loadpaths vs. pullforce

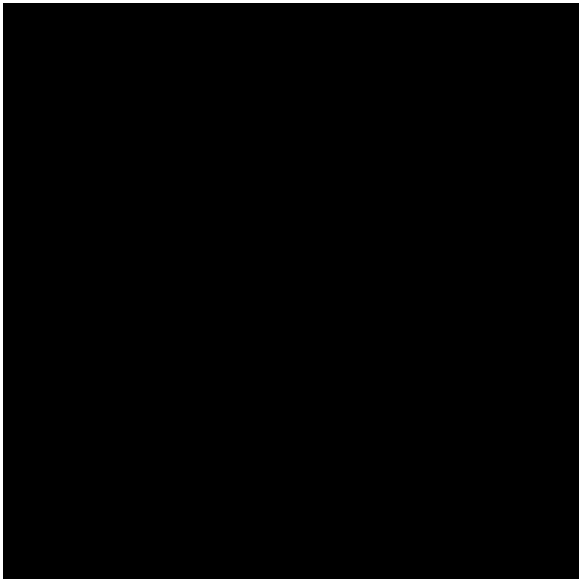


Figure B.9: Belt C: resonance frequencies for all loadpaths vs. pushforce

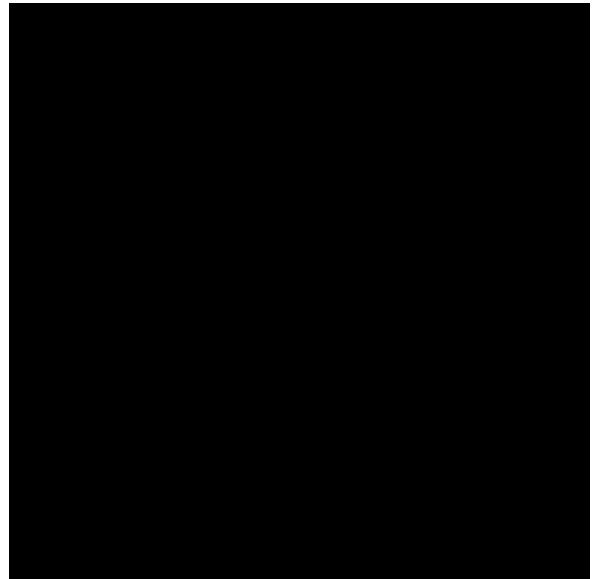


Figure B.10: Belt C: resonance frequencies for all loadpaths vs. pullforce

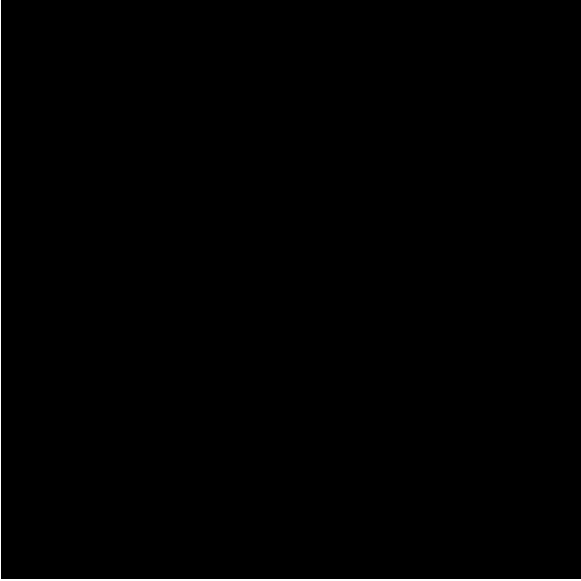


Figure B.11: Belt D: resonance frequencies for all loadpaths vs. pushforce

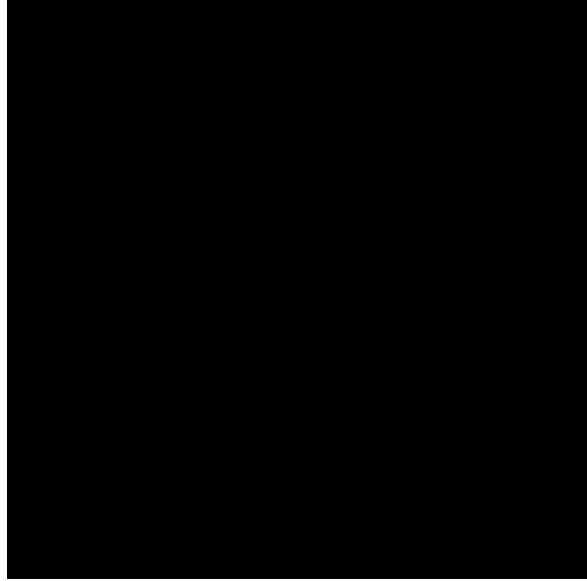


Figure B.12: Belt D: resonance frequencies for all loadpaths vs. pullforce

Appendix C

Pushpart modeling

C.1 Compression curves

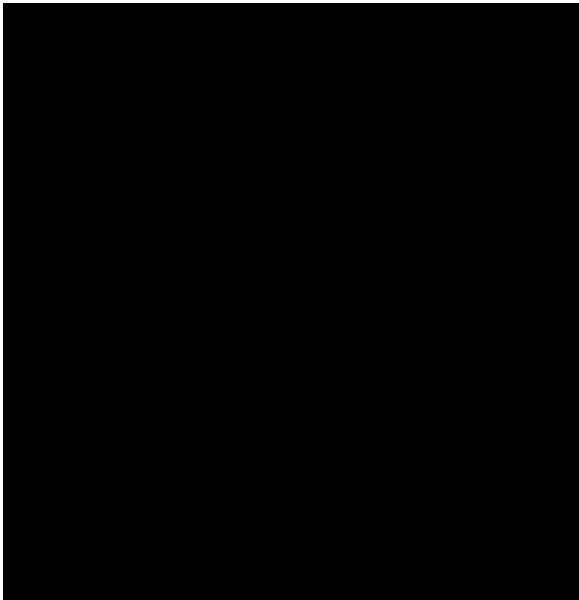


Figure C.1: Belt A: compression curves

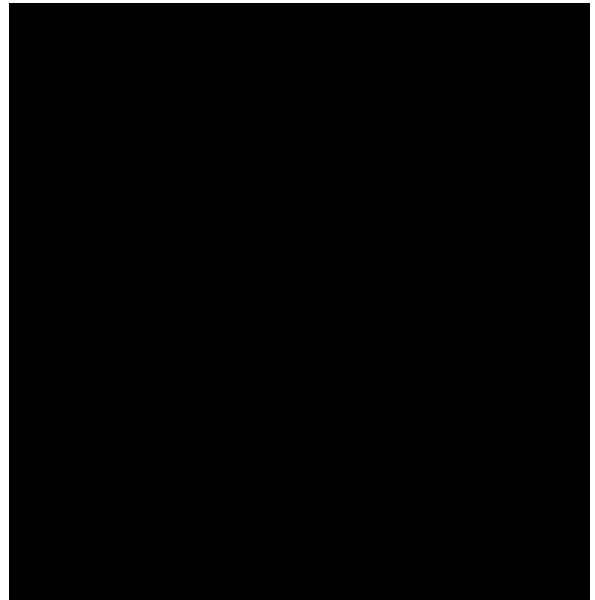


Figure C.2: Belt B: compression curves

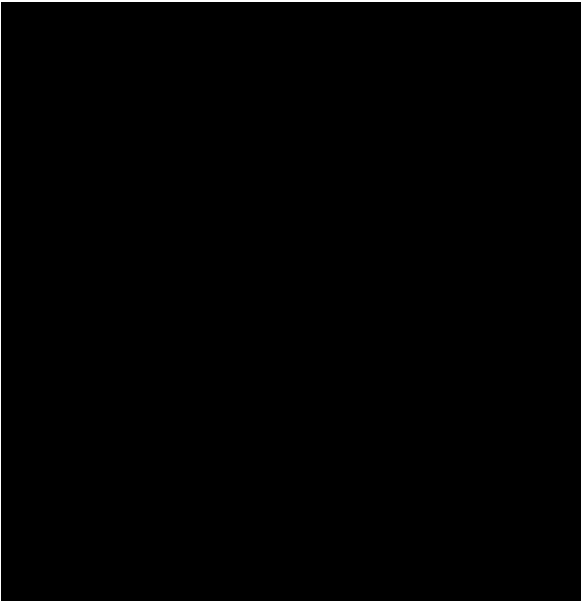


Figure C.3: Belt C: compression curves

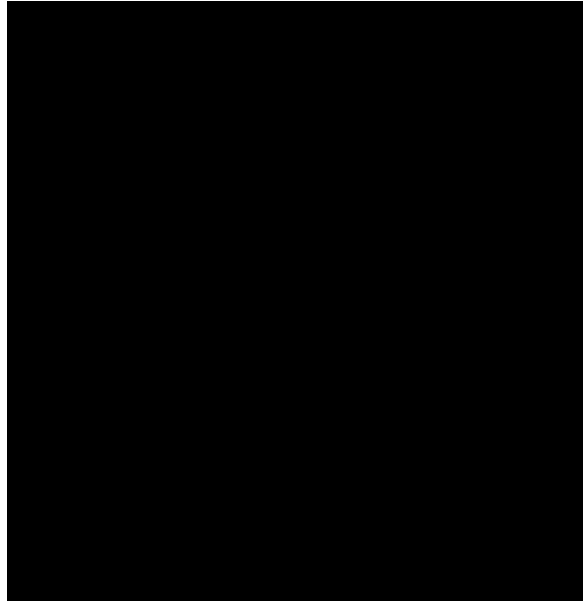


Figure C.4: Belt D: compression curves

C.2 Stiffness curves

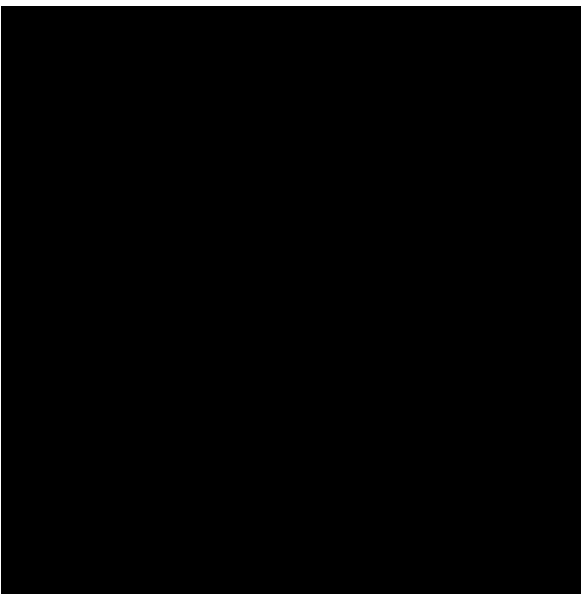


Figure C.5: Belt A: stiffness curves



Figure C.6: Belt B: stiffness curves

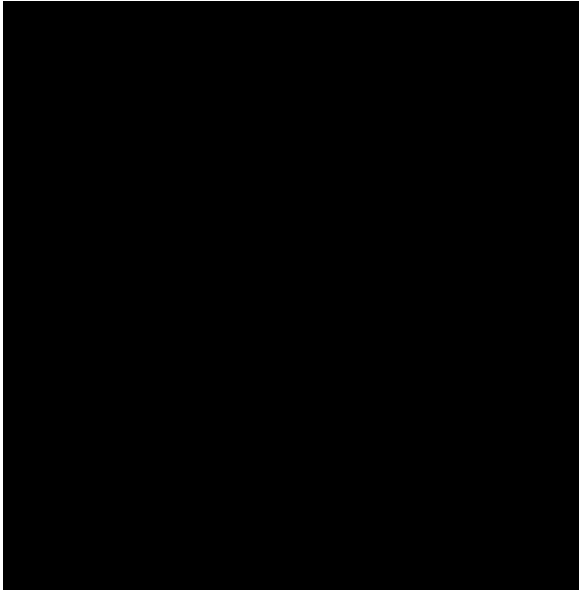


Figure C.7: Belt C: stiffness curves

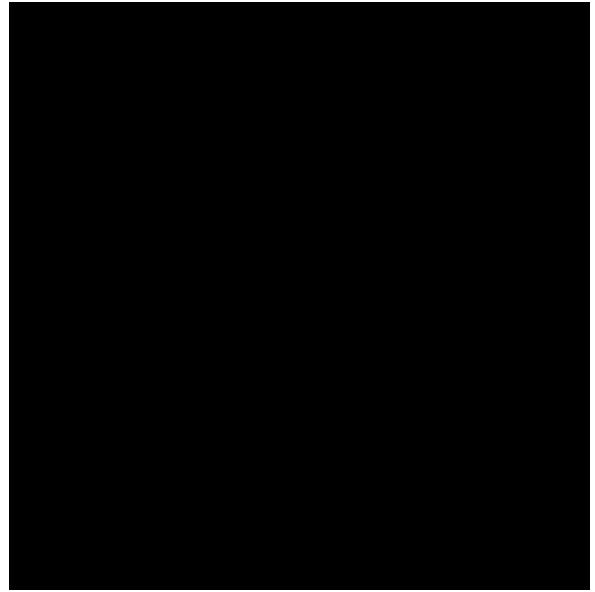


Figure C.8: Belt D: stiffness curves

C.3 Case selection

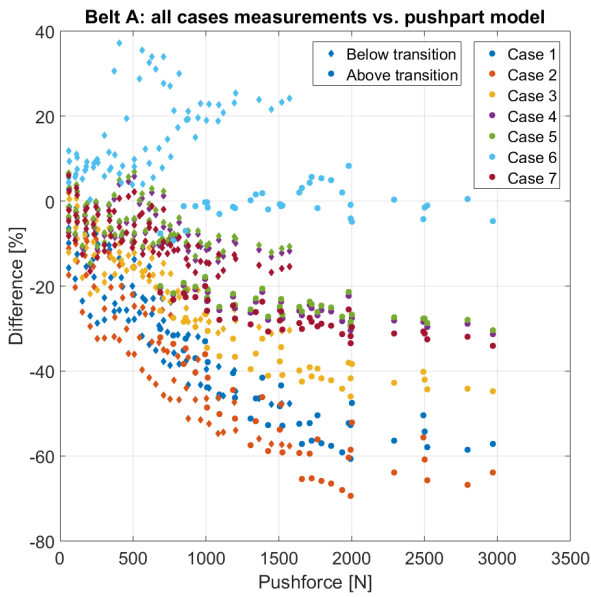


Figure C.9: Percentual difference between pushpart model and measurements for belt A for all cases

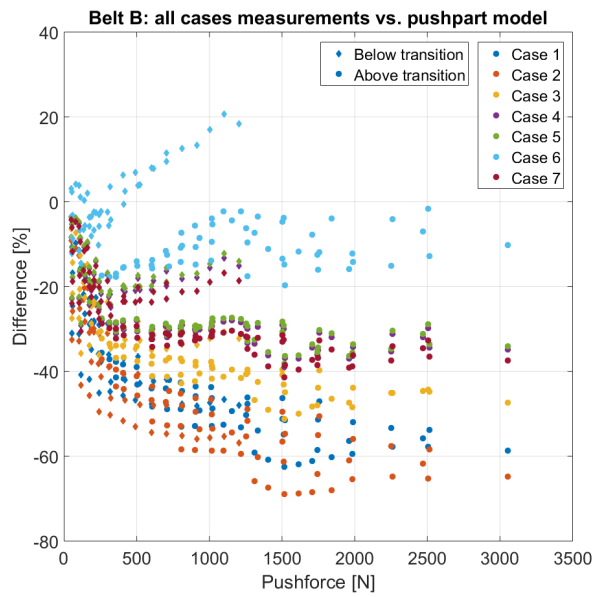


Figure C.10: Percentual difference between pushpart model and measurements for belt B for all cases

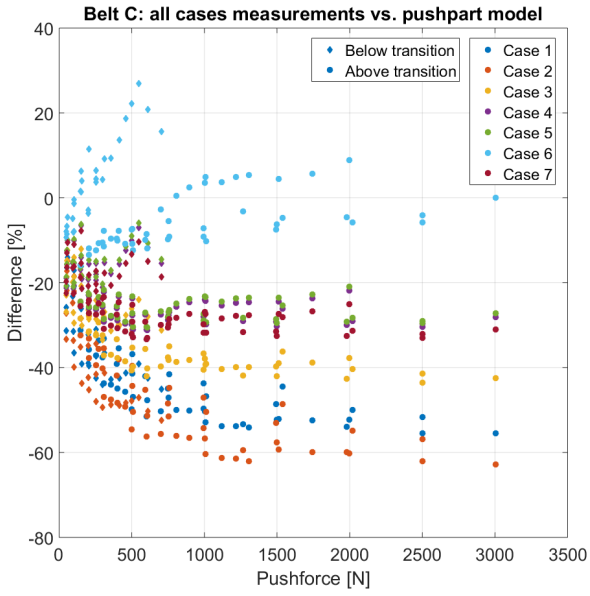


Figure C.11: Percentual difference between pushpart model and measurements for belt C for all cases

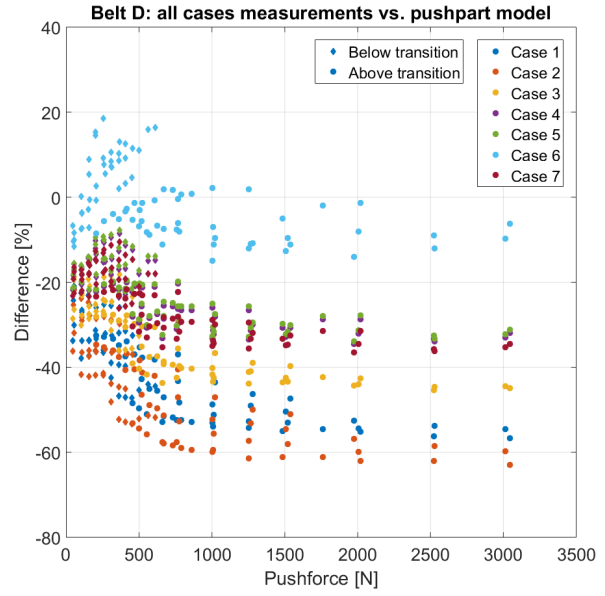


Figure C.12: Percentual difference between pushpart model and measurements for belt D for all cases

Appendix D

Research overview

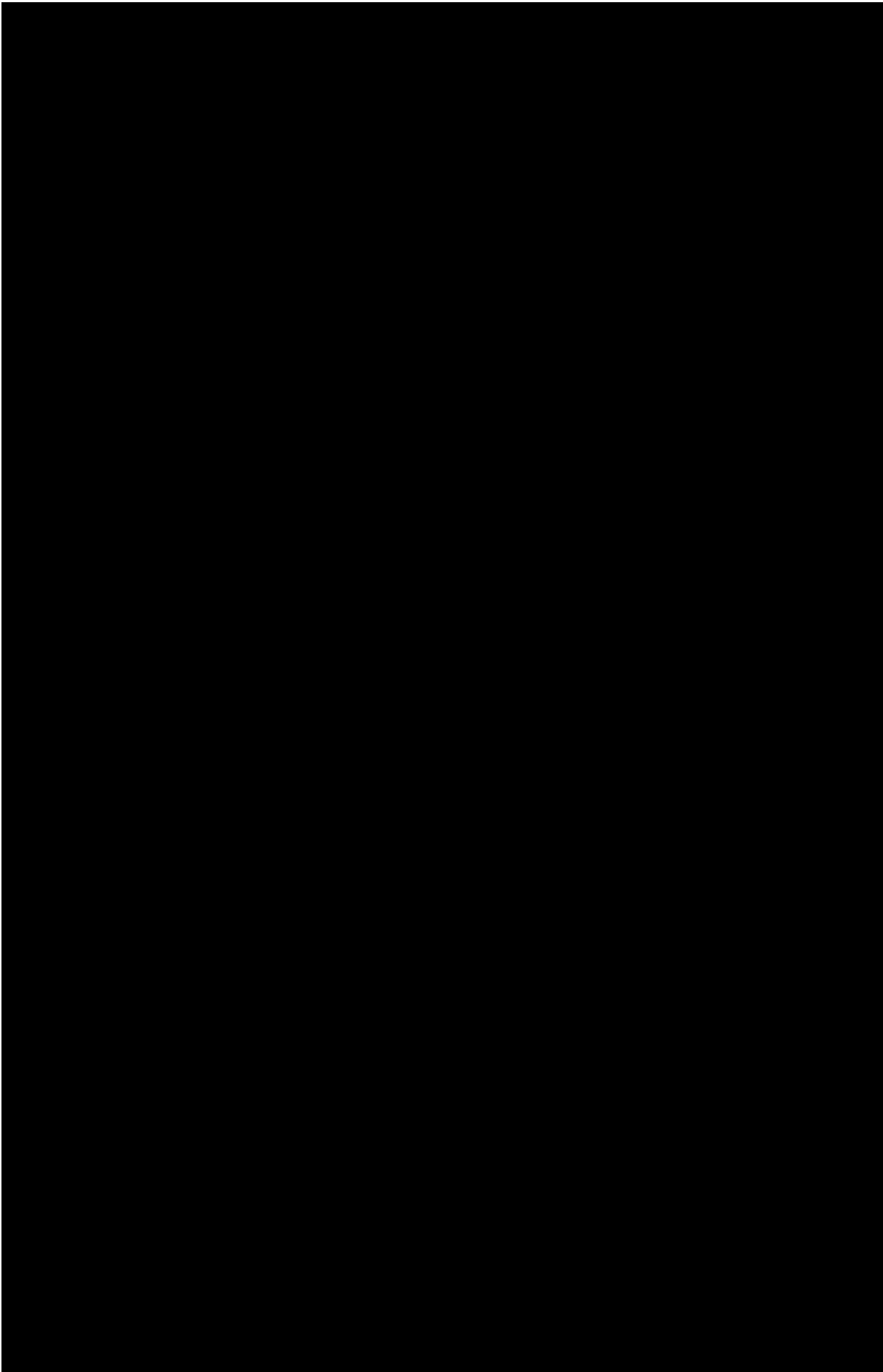


Figure D.1: Research overview

